Deposition and erosion of silt-rich sediment-water mixtures

te Slaa, Steven

DOI
10.4233/uuid:c50eb76c-b2ea-49cf-9873-5c929ff496dc

Publication date
2020

Document Version
Final published version

Citation (APA)
te Slaa, S. (2020). *Deposition and erosion of silt-rich sediment-water mixtures*. [Dissertation (TU Delft), Delft University of Technology]. https://doi.org/10.4233/uuid:c50eb76c-b2ea-49cf-9873-5c929ff496dc

DEPOSITION AND EROSION OF SILT-RICH SEDIMENT-WATER MIXTURES

Steven te Slaa

Deposition and erosion of silt-rich sediment-water mixtures

Steven te Slaa

Deposition and erosion of silt-rich sediment-water mixtures

Dissertation

for the purpose of obtaining the degree of doctor
at Delft University of Technology
by the authority of the Rector Magnificus, Prof.dr.ir. T.H.J.J. van der Hagen,
chair of the Board for Doctorates
to be defended publicly on

Friday 14 February 2020 at 10:00 o'clock

by

Steven TE SLAA

Master of Science in Civil Engineering, Delft University of Technology, the Netherlands
born in Heumen, the Netherlands

This dissertation has been approved by the promotors.

Composition of the doctoral committee:

Rector Magnificus,	chairperson
Prof. dr. ir. J.C. Winterwerp	Delft University of Technology, promotor
Prof. dr. Q. He	East China Normal University, promotor

Independent members:

Prof. dr. ir. Z.B. Wang	Delft University of Technology
Prof. dr. ir. C. van Rhee	Delft University of Technology
Prof. dr. ir. H.J. de Vriend	Delft University of Technology
Dr. D.S. van Maren	Delft University of Technology
Dr. P.J. Vardon	Delft University of Technology

The doctoral research has been carried out in the context of an agreement on joint doctoral supervision between East China Normal University, China and Delft University of Technology, the Netherlands.

This work has been carried as part of the Sino–Dutch collaboration project ‘Effects of human activities on the ecomorphological evolution of rivers and estuaries’ funded by the Dutch Royal Academy of Sciences (KNAW) and is supported by the Natural Science Foundation of China (41130856) within the framework of Scientific Alliances between China and the Netherlands.

Print: Ridderprint

ISBN 978-94-6375-784-3

Table of content

Summary

From a granulometric point of view, sediment can be classified as sand, silt and clay. Silt is thereby defined as sediment with particle sizes equal to, or larger than 2 μm and smaller than 63 μm, with quartz or feldspar as base mineral. Note that quartz and feldspar particles can be smaller than 2 μm. To date, our knowledge on deposition and erosion processes of silt and silt-rich sediment-water mixtures is small compared to their sandy or clayey counterparts, hampering our understanding of large-scale morphological behaviour of silt-dominated systems. The most important difference between clay and silt is that clay consists of clay minerals which have cohesive properties, and as a result, the erosion and deposition of clay beds is influenced by cohesion. The behaviour of cohesive sediment in suspension and in the bed is influenced by flocculation, permeability, effective stress and rheological properties which are related to electro-chemical properties of the base minerals. Silt particles do not have cohesive properties, but there are indications that their erosion behaviour can be apparently cohesive (Roberts et. al., 1998, Van Maren et al., 2009a). Permeability effects are likely to play a role in the behaviour of silt-water mixtures due to the small particles sizes of silt. Such effects result from a difference in timescales between the forcing and the response of the bed and result in apparently cohesive behaviour. Examples are the development of the bed strength with increasing hydrodynamic forcing or the dissipation of overpressures within a compacting silt bed. Such behaviour is characteristic for cohesive material and not for granular material such as silt, and is referred to as apparently cohesive behaviour. In existing literature, the physical processes that control the behaviour of silt are mostly described qualitatively, and silt-specific formulations for hindered settling, compaction and erosion do not exist. Through this thesis, quantitative insights into the physical processes controlling the behaviour of silt-water mixtures have been derived. The overall objectives of this thesis were to *i*) determine the hindered settling behaviour of silt-water mixtures, *ii*) determine the deposition and compaction behaviour of silt beds, and *iii*) determine the erosion behaviour of silt beds.

In contrast to particles larger than 100 μm, the fluid movement around particles smaller than 100 μm is laminar, causing silt particles to settle in the Stokes regime. As a result, the particle shape is of minor influence on the settling velocity and the governing processes for hindered settling of such particles are *i*) return flow and wake formation, *ii*) increased viscosity, and *iii*) buoyancy and reduced gravity. These three effects are combined into a new hindered settling formula (HSF) for silt-sized sediment, which is presented in **Chapter 3**. The HSF accounts for different scaling parameters for the three mentioned processes, which distinguished the HSF from HSF's for cohesive sediment-water mixtures. In addition, the HSF accounts for particle-particle interactions which generates nonlinearity in the increased viscosity. A series of deposition experiments has been carried out in the fluid mechanics laboratory of Delft University of Technology to validate the newly derived HSF. A validation methodology was developed by extending sedimentation theory, established for cohesive sediment, to fine-grained sediment. The derived HSF is found to be in good agreement with results obtained from the laboratory experiments using pure quartz.

An important assumption underlying the hindered settling behaviour of fine-grained sediment-water mixtures is that segregation is a continuous process. The segregation process can strongly influence the deposition and compaction processes and has been studied in **Chapter 4** through a series of deposition experiments carried out at Delft University of Technology. It has been found, that for excess pore-water pressures to develop within silt beds, the timescale for bed formation should be sufficiently small for water to be captured within the bed. Pore-water flow, which is controlled by the beds permeability, results in the dissipation of excess pore-water pressures in self compacting silt beds. The deposition experiments have demonstrated that segregation can result in low permeability beds. Such compaction is characteristic for apparently cohesive behaviour. Therefore, the segregation process is found to be of significant importance for the compaction process of silt beds.

Shear flow induced erosion of silt beds has been studied in **Chapter 5**. A new surface erosion formulation for silt beds has been derived in analogy with Winterwerp et al. (2012), by following a soil mechanics approach. The primary assumption underlying the surface erosion of silt beds is that at zero isotropic stresses at the surface of the bed, the erosion behaviour is dominated by the dissipation of pore-water underpressures. The dissipation rate of pore-water underpressures is related to the permeability parameter and follows from term 2 of the Gibson equation. Term 2 is hence assumed to govern the inflow of water in the silt bed and is therefore considered suitable to describe the surface erosion (and the initial compaction) process of silt beds. It is thereby assumed that silt particles are non-swelling. The silt bed however may increase in volume due to shear-dilatancy as a response to hydrodynamic load conditions. Underpressures then occurring in the soil strengthen the granular skeleton and reflect an apparent bonding strength, which is referred to as apparent cohesion (undrained conditions). The erosion formulation has been tested against experimental data obtained with a Gust Microcosm (erosion chamber). It has been concluded that the proposed surface erosion formulation for silt is in sufficient agreement with experimental data and that the soil mechanics approach for studying the erosion of cohesive sediment beds can be extended to fine-grained sediment beds.

The behaviour of silt-rich sediment mixtures in the real world has been examined with sedimentation and erosion experiments on sediment from the Yangtze River and Yellow River in China (**Chapter 6**). Sedimentation experiments have been carried out at the State Key Laboratory of Estuarine and Coastal Research (SKLEC) of the East China Normal University (ECNU) in Shanghai and erosion experiments have been carried out at the Faculty of Ocean Science and Engineering of Zhejiang University in Hangzhou. Through these experiments, it has been found that the presence of a clay fraction in the sediment composition results in fundamental differences between the settling, deposition, compaction and erosion behaviour of sediment from these systems and the behaviour of pure silt.

Overall, this work contributes to improving the understanding of the behaviour of silt-water mixtures and silt-rich sediment mixtures. New formulations for the hindered settling of fine-grained sediment-water mixtures and the surface erosion of silt beds have been developed. It has been concluded that time-dependent processes play a dominant role in the hindered settling, deposition, compaction and erosion behaviour of silt. The new formulations can be used to

study natural processes in silt-rich sediment systems and can help to understand the impacts of human interventions and/or natural changes on large scale morphological development in rivers and estuaries.

Samenvatting

Vanuit een granulometrisch oogpunt kan sediment worden geclassificeerd als zand, silt en klei. Silt wordt daarbij gedefinieerd als sediment deeltjes groter dan, of even groot als, 2 μm en kleiner dan 63 μm, met kwarts of fledspar als basismineraal. Hierbij wordt opgemerkt dat kwarts- en feldspardeeltjes kleiner kunnen zijn dan 2 μm. Tot op heden blijft de kennisontwikkeling van erosie en depositie processen van silt achter op de kennisontwikkeling van haar zandige of kleiachtige tegenhangers, wat het begrip van grootschalig morfologisch gedrag van door silt gedomineerde sediment systemen belemmert. Het voornaamste verschil tussen klei en silt, is dat klei bestaat uit kleimineralen met cohesieve eigenschappen waardoor erosie en depositie gedrag van slib (cohesief sediment mengsel) sterk wordt beïnvloed door cohesie. Het gedrag van cohesief sediment in suspensie en in het bed wordt beïnvloed door flocculatie, permeabiliteit, effectieve spanningen en reologische eigenschappen welke te relateren zijn aan de elektrochemische eigenschappen van het basismineraal. Siltdeeltjes zijn niet cohesief, echter, er zijn aanwijzingen dat het erosiegedrag van silt bedden schijnbaar cohesief kan zijn (Roberts et. al., 1998, Van Maren et al., 2009a). Hierbij is het waarschijnlijk dat permeabiliteitseffecten een voorname rol spelen in het gedrag van silt bedden vanwege de kleine deeltjesgrootte. Dergelijke effecten vloeien voort uit een verschil in tijdschalen tussen de belasting op het bed en de reactie van het bed en resulteren in dergelijk schijnbaar cohesief gedrag. Voorbeelden hiervan zijn de ontwikkeling van de bedsterkte met toenemende hydraulische belasting, maar ook de dissipatie van grondwater overdrukken in een compacterend silt bed. Dergelijk gedrag is kenmerkend voor cohesief materiaal en niet voor granulair materiaal zoals silt en wordt derhalve aangeduid met de term schijnbaar cohesief gedrag. In de bestaande literatuur worden de fysieke processen die het gedrag van silt bepalen met name kwalitatief beschreven en silt specifieke formuleringen voor hindered setttling, compactie en erosie bestaan niet. Met dit proefschrift zijn kwantitatieve inzichten verkregen in de fysische processen die het gedrag van silt-watermengsels bepalen. De algemene doelstellingen van dit proefschrift waren daarbij *i*) het hindered settling gedrag van silt-watermengsels bepalen, *ii*) het bezinkings- en compatiegedrag van silt bedden bepalen, en *iii*) het erosiegedrag van silt bedden bepalen.

In tegenstelling tot deeltjes groter dan 100 μm is de vloeistofbeweging rond deeltjes kleiner dan 100 μm laminair, waardoor siltdeeltjes bezinken in het Stokes-regime. Als gevolg hiervan wordt de bezinksnelheid slechts in geringe mate beinvloed door de vorm en zijn de bepalende processen voor het hindered settling gedrag van silt: *i*) retourstroom en neervorming, *ii*) verhoogde viscositeit en *iii*) drijfvermogen en gereduceerde zwaartekracht. Deze drie effecten zijn gecombineerd om een hindered settling formulering (HSF) voor silt af te leiden, welke is gepresenteerd in **hoodstuk 3**. De HSF houdt rekening met verschillende schaalparameters voor de drie genoemde processen, waardoor de HSF onderscheidend is ten opzichte van HSF's voor cohesief sediment-water mengsels. Tevens houdt de HSF rekening met interactie tussen deeltjes welke niet-lineare effecten genereren in de verhoogde viscositeit. De nieuw geformuleerde HSF in gevalideerd met behulp van een reeks bezinkings experimenten, uitgevoerd in het vloeistofmechanica laboratorium van de Technische Universiteit Delft. Een validatiemethode is hiervoor ontwikkeld door een voor cohesief sediment gangbare

sedimentatietheorie geschikt te maken voor fijnkorrelig sediment. De afgeleide HSF blijkt goed overeen te komen met resultaten verkregen uit laboratoriumexperimenten met zuiver kwarts.

Een belangrijke veronderstelling die ten grondslag ligt aan het hinderded settling gedrag van fijnkorrelig sediment (waar silt onder valt), is dat segregatie een continu proces is. Het segregatieproces is voorts van significant belang voor depositie- en compactie processen, welke zijn bestudeerd in **hoofdstuk 4** met behulp van een serie deposite experimenten uitgevoerd aan de Technische Universiteit Delft. Het is bevonden dat voor het ontstaan van wateroverspanningen in silt bedden, de tijdschaal voor bedvorming voldoende klein dient te zijn om water in het bed te vangen. Poriewaterstroming, waarvan de snelheid afhankelijk is van de permeabiliteit van het bed, resulteert in de dissipatie van water overspanning in zelf compacterende silt bedden. De depositie experimenten tonen aan dat een lage permeabiliteit het gevolg kan zijn van segregatie. Het compacteren van silt bedden wordt daarbij kenmerkend beschouwd voor schijnbaar cohesief gedrag. Segregatie heeft daarom een significante invloed op het sedimentatie process en bepaalt in sterke mate de compactiesnelheid van silt bedden.

Oppervlakte erosie van silt bedden is bestudeerd in **hoofdstuk 5**. Een nieuwe formulering voor oppervlakte-erosie voor silt bedden is afgeleid in analogie met Winterwerp et al. (2012), waarin een opervlakte-erosie formulering voor zand-slib mengsels is afgeleid volgens grondmechanische principes. De primaire veronderstelling die ten grondslag ligt aan deze oppervlakte-erosie formulering is dat bij afwezigheid van isotrope spanningen aan het oppervlak, het erosiegedrag wordt gedomineerd door de dissipatie van grondwater onderdrukken. De dissipatiesnelheid van grondwater spanningsgradienten is gerelateerd aan de permeabiliteit parameter en volgt uit term 2 van de Gibson-vergelijking. Van term 2 wordt daarom aangenomen dat deze de instroom van water in het silt bed reguleert en wordt daarom geschikt geacht om het oppervlakte-erosieproces (maar ook het initiële compactie proces) van silt te beschrijven. Er wordt daarbij aangenomen dat silt deeltjes niet opzwellen. Het silt bed kan echter in volume toenemen ten gevolge van schuifspanning in reactie op een hydraulische belasting. Grondwater onderdrukken die vervolgens in het bed optreden, versterken het korrel skelet (effectieve spanning) en reflecteren een schijnbare bindingssterkte, dat wordt aangeduid als schijnbare cohesie (ongedraineerde omstandigheden). De erosieformulering is gestaafd met experimentele data verkregen met een Gust Microcosm (erosie meter), uitgevoerd op Deltares. De voorgestelde oppervlakte-erosieformulering voor silt komt voldoende overeen met experimentele gegevens. De grondmechanische benadering gehanteerd om het erosiegedrag van slib te bestuderen kan hierdoor worden uitgebreid tot fijnkorrelige sedimentbedden.

Het gedrag van silt-rijke sedimentmengsels uit natuurlijk systemen van de Yangtze Rivier en de Gele Rivier in China, is onderzocht in **hoofdstuk 6**. Hiervoor zijn sedimentatie-experimenten uitgevoerd bij de State Key Laboratory of Estuarine and Coastal Research (SKLEC) van de East China Normal University (ECNU) in Shanghai en erosie-experimenten zijn uitgevoerd bij de faculteit Ocean Science and Engineering van de Zhejiang University in Hangzhou. Uit deze experimenten is geconcludeerd dat de aanwezigheid van een klei fractie resulteert in fundamenteel verschillend hindered settling, depositie, compactie en erosie gedrag van sediment uit de genoemde rivieren en puur silt.

In algemene zin draagt dit proefschrift bij aan de verbetering van het begrip het gedrag van silt-water mengsels en silt-rijk slib. Nieuwe formuleringen voor hindered settling van fijnkorrelig sediment-water mengsels en oppervlakte erosie van silt bedden zijn ontwikkeld. Gebleken is dat tijdafhankelijke processen een dominante rol spelen in het hindered settling, depositie, compatie en erosiegedrag van silt. De formuleringen kunnen worden gebruikt om natuurlijke processen in silt-rijke sedimentsystemen te bestuderen en kunnen helpen de effecten van menselijke interventies en / of natuurlijke veranderingen op grootschalige morfologische ontwikkeling in rivieren en estuaria te begrijpen.

总结

海岸，三角洲和河流沿岸的泥沙沉积和侵蚀会导致地理形态的变化，这些变化对于社会经济的发展来说，可能是积极的（增加新的土地），又或是负面的（导致航道的淤积）。泥沙按照不同粒径可分为砂，粉砂和粘土。粉砂被定义为粒径大于等于 2μm 且小于 63μm 的颗粒的沉积物，其中石英或长石作为主要矿物。需要注意的是石英和长石颗粒粒径可小于 2μm。在某些环境中，如在中国的黄河和长江，粉砂是沉积物的主要组成。因此，正确理解这些粉砂为主的沉积物的行为才能较好地预测这些河流的形态动力响应。粘土和粉砂之间最重要的区别，是粘土由具有粘性的粘土矿物组成，因此粘土层的侵蚀和沉积都受到粘聚力的影响。粉砂颗粒不具有粘结性，但有迹象表明它们的侵蚀行为具有表观粘聚特性（Roberts 等，1998，Van Maren 等，2009）。然而，迄今为止，我们对粉砂侵蚀和沉积过程的了解，对比砂质土和粘性土来说更少，阻碍了我们对以粉砂主导的河流系统大范围形态行为的理解。

粘性泥沙作为悬疑质和底质的行为受絮凝，渗透性，有效应力和流变性质的影响，这些性质与基础矿物的电化学性质有关。粉砂不具备这种电化学性质。然而，由于颗粒尺寸小，渗透效应可能在粉砂底质的行为中起作用。 这种效果是由压力和底床的响应之间的时间尺度差异引起的，并导致表观粘聚特性。一个例证是底床的强度会随着流体动力强度的增加或压实粉砂底床内超压的消散而增加。这种行为是粘性（电化学带电）材料的特征，而不是颗粒材料如粉砂的特征，并被称为表观粘聚特性。

控制粉砂行为的物理过程大多是定性描述的，并且不存在用于阻碍沉降，压实和侵蚀的粉砂特定公式。本论文旨在对控制粉砂与水的混合物行为的物理过程进行定量分析。本论文的总体目标是：i）确定粉砂与水的混合物的受阻沉降行为，ii）确定粉砂底床的沉积和压实行为，以及 iii）确定粉砂底床的侵蚀行为。

文献研究（第 2 章）揭示了粉砂在压实和侵蚀时可以表现出表观粘聚特性。导致这种粉砂与水的混合物的表观粘聚特性的根本物理过程仍未定义。然而，粉砂底床的低渗透性很可能发挥重要作用。

第 3 章研究了细颗粒沉积物与水混合物的受阻沉降行为。与大于 100μm 的颗粒相比，粒径小于 100μm 的颗粒周围的流体运动是层流，引发粉砂颗粒在斯托克斯体系中产生沉降。结果就是，颗粒形状对沉降速度的影响很小。

阻碍颗粒沉降的控制过程是：i）形成回流和尾流，ii）粘度增加和 iii）产生浮力、减少重力。将这三种效应结合起来形成粉砂沉积物的受阻沉降公式（HSF）。在该 HSF 中，假设颗粒与颗粒相互作用在增加的粘度中产生了非线性。此外，还引入了最小和最大固相含量来解释不同固相含量下粘度增加、回流和尾流的形成。其和 Richardson Zaki HSF（Richardson 和 Zaki，1954）的根本差异是与缩放参数有关。

为了验证新推导的 HSF，在代尔夫特理工大学流体力学实验室进行了一系列的泥沙沉积实验。通过将粘性泥沙的沉积理论推广到细颗粒泥沙中，建立了一种验证方法。所得的 HSF 值与纯石英实验结果吻合较好。在阻碍细粒泥沙沉降过程中，一个重要的假设是分凝运动是一个连续的过程。这种分凝过程对于第四章中研究的沉积和压实过程很重要。

粉砂底床的压实过程被认为部分类似于粘性沉积底床的固结过程。对于在粉砂床中产生过大的孔隙水压力，底床形成的时间尺度应足够小，以便水可在底床内被捕获。由床渗透率控制的孔隙水流导致压实粉砂床中超孔隙水压力的消散。因此，较低的渗透率会在可测量的时间范围内降低压实率。沉积实验表明，低渗透率可能是由分凝作用导致。这种压实率的降低是表观粘聚特性的特征。因此，渗透率是表示粉砂床压实率的参数。

由于粉砂尺度沉积物的压实特性被认为在很大程度上取决于河床渗透率，因此 Gibson（Gibson 等，1967）固结公式（描述渗透率）的第二项被认为足以用于压实粉砂的数学表述。有人认为 Gibson 公式的第 3 项在压实的初始阶段不太重要。

利用 Gust Microcosm (侵蚀室)的实验数据对冲刷公式进行对比，在 Deltares 实验室开展了不同固体含量的细粒泥沙床上的一系列冲刷试验，结果表明，提出的表层泥沙冲刷公式与试验数据吻合较好。然而，与 Roberts 等人(1998)获得的实验数据进行附加对比后表明，尽管趋势基本一致，但数据吻合性较差。此外，研究粘性泥沙床面冲刷的土力学方法也可以推广到细粒泥沙床。

在实验室条件下通过对纯粉砂质泥沙的沉降、沉积、固结和再侵蚀动力特性的测试之后，对自然情况下中国长江与黄河的粉砂-水混合物的动力特性也进行了测试（第 6 章）。为了达到测试目的，采用了与纯粉砂质泥样相同的方式进行了采集和实验室分析。沉降试验开展于上海华东师范大学河口海岸国家重点实验室和冲刷试验开展于杭州浙江大学海洋工程学院。

泥沙沉积过程中的容重变化主要由泥沙固结/压实造成，粉砂质泥沙混合物沉降试验成果显示由于泥沙成分的变化，其密度变化过程表现出不同的特征，Van Ledden et al.(2004)认为，非粘性侵蚀行为和粘性侵蚀行为会在粘土含量为 5 - 10%之间时发生转变。从沉积实验中还发现，粘土含量约为 10%是泥沙沉积为非粘性固结行为与粘性固结行为转换的临界值。

与粉砂床面相似，在采样自长江和黄河以粉砂为主的泥沙混合物沉积实验中，观测到垂直均匀的过剩孔隙水剖面。与纯粉砂试验相比，在粉砂为主的泥水混合物覆盖分离粒状物后形成一个低渗透的外壳，前面显示压实率受上覆粘土-水混合物的控制，据此可以推断这个外壳的形成可能是颗粒大小或泥沙组分分离的结果。在上阶段在以粉砂为主的沉积物密实后期，或者孔隙水会从剩余的空隙粘土絮凝体(固结)排出，或者发生粉砂层的进一步压实。也有可能会发生固结和压实相结合的情况。

综上，本次研究工作有助于增进对粉砂-水混合物和粉砂为主的泥沙混合物行为的了解。研究发现，随时间的变化过程在泥沙的沉降、淤积、压实和侵蚀行为中起主导作用。泥沙组成中粘土组分的存在导致泥沙的沉降、沉积、压实和冲刷特性在纯粉砂和粉砂为主的泥沙混合物之间存在根本差异，更好地理解了粉砂沉积和压实的物理过程。本文研究了细粒泥沙-水混合物的阻碍沉降和粉砂层表面冲刷的新公式，通过试验验证，其总体表现良好。这些公式可用于研究富含粉砂的海岸河口系统的自然过程，并有助于了解人类干预和自然变化对河流和河口大规模形态发展的影响。但对公式的一个重要限制是泥沙混合物未展现粘聚行为。

Chapter 1

Introduction

1 Introduction

1.1 General

1.1.1 Background

Siltation and erosion of sediment occurs in and along coasts, deltas, and rivers. Sediments are a natural resource and therefore siltation has many economic benefits. The term siltation is often used regardless of the composition of the deposited sediment and may be interchangeably used with the term deposition. Floodplain deposits as a result of high river discharges leave a layer of fertile soil on annual bases, which is beneficial for croplands. At locations where siltation rates are high new land is reclaimed from the sea. Both modern and ancient civilizations owe their prosperity to this form of siltation. However, siltation may also have adverse effects, especially in combination with human activities: harbour basin and waterway siltation require costly maintenance programs to safeguard navigation. In addition, human settlements result in river confinement, suppressing its natural course. Consequently, ongoing floodplain deposition reduces the river's flood conveyance capacity resulting in an ongoing demand of riverbank fortification (examples are the Yellow River in China, the Kura & Aras Rivers in Azerbaijan and the river Po in Italy). Lastly, dam construction in catchment areas results in a decrease in sediment supply to coastal regions due to reservoir siltation. This may lead to regression or a halt of the coastline expansion (Yangtze Estuary). Above mentioned examples demonstrate that siltation has both advantages and disadvantages. Moreover, these examples indicate the need for understanding the deposition and erosion behaviour of sediment in particular to predict future morphological developments in natural and anthropogenic environments. This thesis focusses on settling, deposition, compaction and erosion behaviour of silt (Figure 1-1), as these processes are essential for sediment transport.

In sedimentology, a basic distinction is made between sand, silt and clay. Mud is a collective noun for mixtures of mainly clay and silt. The primary distinction between silt and other constituents of natural sediment (amongst others clay, sand and organic matter) is based on particle size and chemistry (Krumbein and Sloss, 1963). Silt is defined as sediment with particles smaller than 63 μm, with quartz or feldspar as base mineral. Clay is the fraction with minerals consisting of phyllo-silicates with particles smaller than 2 μm in general. The most important difference between the clay fraction and the silt fraction is that the clay fraction consists of clay minerals which have cohesive properties (i.e. an electromagnetic attraction between particles resulting in the formation of coagulates known as flocs, which strongly influence the settling, deposition, compaction, and erosion behaviour – see **Chapter 2** for details). As a result of these properties, sediment beds with a sufficient clay fraction show cohesive behaviour. The clay content determines to a large extent the overall behaviour of a sediment mixture. Studies on erosion behaviour of sand-mud mixtures indicate that the bed exhibits cohesive behaviour for clay contents above 5-10% (Van Ledden et al., 2004).

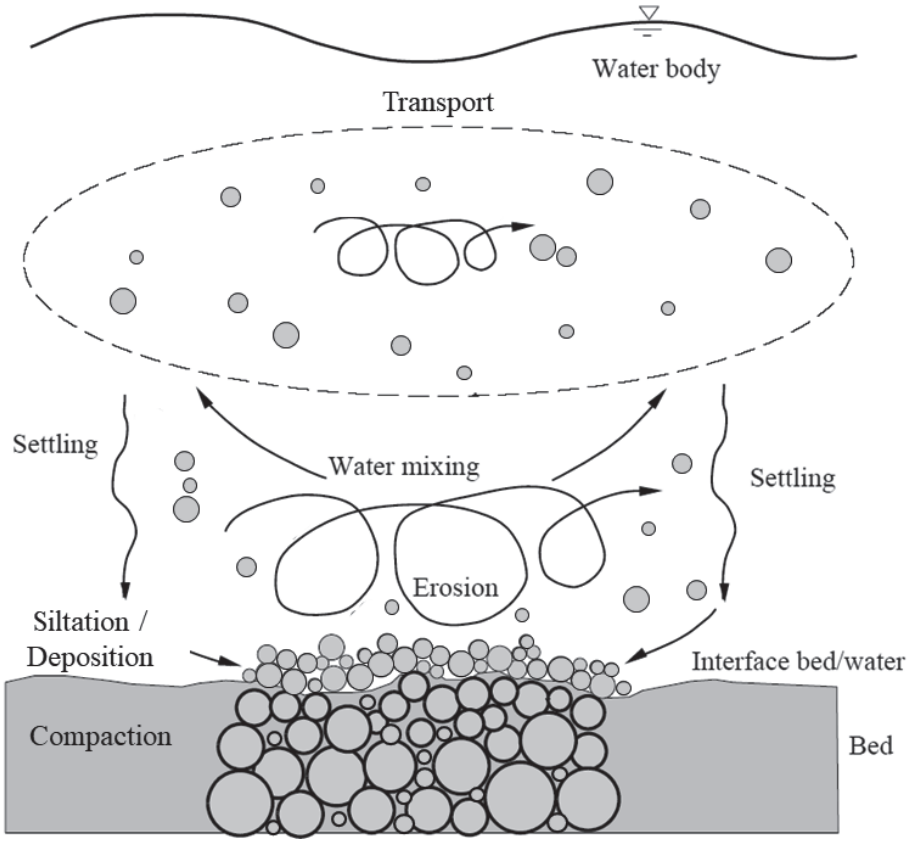

Figure 1-1 Cycle of deposition and resuspension of granular sediment, redrawn after Maggi (2005).

1.2 Problem description

In some environments, such as in the Yellow River and Yangtze River mouth in China, silt is the prevailing sediment fraction. Assessment of the sediment dynamics in these rivers, and its modelling, requires proper understanding of the behaviour of the sediments encountered herein and hence the behaviour of silt in particular. Whether silt depicts cohesive or non-cohesive behaviour has received little scientific attention and is subject of ongoing discussion (Roberts et al., 1998, Van Maren et al., 2009b). A possible explanation for the little scientific attention paid to the specific behaviour of silt-water mixtures and silt-dominated systems might be the locations from where cohesive sediment research originates: mainly the America's and Europa. On these continents, silt-dominated systems are scarce. However, China's Yellow and Yangtze River are examples of natural systems that contain very high (>0.7) silt contents. Due to its small grain size, these rivers may carry large amounts of sediment in suspension. At such high sediment concentrations, settling of sediment is reduced by grain-grain and grain-fluid interaction, collectively described as hindered settling. Locally, the silt content is higher and

can reach up to 0.9. Due to the limited knowledge on erosion and deposition of silt in silt-rich sediment systems, our understanding of the large-scale morphological behaviour of such systems is limited.

Van Maren (2007) and Van Maren et al (2009a, 2009b) qualitatively describes several silt-related hydrodynamic and soil mechanical processes that might play a role in the Yellow River's morphology. The processes, as described by Van Maren (2007) and Van Maren et al (2009a, 2009b), are mainly based on theoretical arguments and lack a thorough experimental base. They suggest that compaction of silt takes time, in contrast with sand in which compaction of a deposited bed is instantaneous. This has implications for the erosion behaviour of silt as well. Erosion experiments with pure quartz particles indeed show a decrease in erosion rate with increasing density (Roberts et al., 1998). Also, their experiments suggest that erosion rates decrease with decreasing grain size (in contrast to sand particles), suggesting cohesive behaviour.

The behaviour of cohesive sediment in suspension and in the bed is influenced by flocculation, permeability, effective stress and rheological properties. These characteristics are related to electro-chemical processes of the base minerals which are absent in silt. However, permeability effects can start to play a role in the behaviour of silt due to the small particle sizes. These effects can result in cohesive like behaviour (such as development of strength of the bed in time), which will be referred to as apparently cohesive behaviour. The apparent cohesion originates from different time scales of the forcing and the response of the bed. The aim of this research is to develop a more thorough insight into the underlying physical mechanisms controlling the behaviour of silt-water mixtures and silt-dominated sediment-water mixtures.

1.3 Hypothesis and objectives

The physical processes that control the behaviour of silt are mostly described qualitatively and silt-specific formulations for hindered settling, compaction and erosion do not exist. This thesis aims at expanding our knowledge on the behaviour of silt-water mixtures in particular and of silt-rich sediment mixtures in natural systems. The following hypotheses are formulated for the behaviour of silt:

- Silt is very fine, hence time scales for settling, compaction and pore water flow are large, determining to a large extent its physical behaviour;
- The permeability of silt beds is an important parameter for its behaviour and is largely influenced by the particle size distribution;
- The time scales of the compaction and erosion processes are sufficiently large, in relation to the forcing timescales (tides, storm surges and flood waves) to significantly influence morphological developments in silt-rich environment;
- The erosion of silt beds can be described from a soil mechanical perspective;
- The deposition behaviour of silt is not influenced by flocculation and hence segregation can occur.

The hypothesis mentioned above result in the following objectives of the present study:

- To determine the hindered settling behaviour of silt-water mixtures;
- To determine the deposition and compaction behaviour of silt beds;
- To determine the erosion behaviour of silt beds.

1.4 Approach

This study sets out to combine laboratory experiments and fieldwork to obtain a better understanding on the behaviour of silt and silt-dominated sediment mixtures. A literature study (**Chapter 2**) is carried out to further identify the unknown physical processes in the behaviour of silt. Analogies with sand and clay are made to position the behaviour of silt within a sedimentological framework.

Laboratory experiments with pure silt are carried out under controlled conditions in the fluid mechanics laboratory of Delft University of Technology (DUT). The experimental results are used to investigate hindered settling, compaction and erosion of pure silt in **Chapters 3, 4 and 5** respectively. New formulations are proposed for the hindered settling of silt and the surface erosion of silt beds.

Field campaigns are carried out in the Yangtze River Estuary and the Yellow River to obtain samples of natural silt dominated sediment mixtures. With these sediment samples, sedimentation experiments are carried out at the State Key Laboratory of Estuarine and Coastal Research (SKLEC), East China Normal University (ECNU) in Shanghai and erosion experiments are carried out at the Faculty of Ocean Science and Engineering of Zhejiang University in Hangzhou. The experiments with sediment from the field serve as case study to identify differences between the behaviour of pure silt and silt-rich sediment in natural systems. The experiments and their results are presented in **Chapter 6**. A synthesis and conclusions follow in **Chapter 7**.

Chapter 2

Literature review

2 Literature review

2.1 General

Individual sediment particles are formed by physical and chemical erosion in source areas, generally decreasing in size by abrasion as they are carried downstream by rivers. Sediment particles range in size from large boulders to colloidal sized fragments. The mineral constituents of sand, silt or clay mainly consist of silicate minerals of which quartz, feldspar, and clay-minerals are the most common. Feldspars are a group of rock-forming silicate minerals which make up as much as 60% of the earth's continental crust. After feldspar, quartz is the most abundant silicate mineral. Silt and sand consist of quartz and feldspar minerals, which are non-cohesive by definition. For analysing deposition and erosion processes, distinction between cohesive and non-cohesive particles on micro scale sediment is essential for understanding its large scale behaviour.

The rate of suspended sediment transport in water is governed by erosion and deposition processes in general. Deposition prevails during relatively low energy conditions, whereas sediment is re-suspended from the bed during more energetic conditions. The shear stress at which sediment starts to erode depends on the grain size (non-cohesive sediment), or on the degree of consolidation and material properties of clay (cohesive sediment). Cohesive sediments consolidate, thereby increasing their resistance against erosion in time, whereas sand forms a rigid bed upon deposition. The erosion threshold of sand therefore only depends on grain size, and is known from Shield's (1936) diagram for the initiation of motion, see e.g. Van Rijn (1984, 2007). Erosion processes of mud beds have received attention since the work of Partheniades (1962), Krone (1962) and Ariathurai and Arulandan (1978). The erosion rate of cohesive sediment beds depends on the degree of consolidation of which our knowledge has advanced significantly since the pioneering work of Terzaghi and Fröhlich (1936), and through the work of e.g. Been and Sills (1981) and Merckelbach (2000). Since the 1990's, more attention has been paid to mixtures of sand and mud. The effect of mud on erosion thresholds of sand-mud mixtures is analysed by e.g. Mitchener and Torfs (1996) and Van Ledden et al. (2004), and of sand on mud beds by Jacobs (2011) and Winterwerp et al. (2012). Similarly, the influence of sand on hindered settling (Dankers and Winterwerp, 2007, Cuthbertson et al., 2008, Cuthbertson et al., 2010, Manning et al., 2010, Manning et al., 2011) and consolidation (Torfs et al., 1996, Winterwerp and Van Kesteren, 2004) is reasonably well understood.

Compared to sand and mud, little specific scientific attention has been given to silt because it often occurs as part of mud of which the properties are strongly influenced by the clay fraction in it. However, sediment mixtures consisting of nearly only silt do occur in natural systems, e.g., the Yellow River and the Yangtze River. Compared to the present state of knowledge on the behaviour of sand, mud, and sand-mud mixtures, little is known about settling, deposition and erosion processes of silt and silt-dominated sediment mixtures.

2.2 Sediment properties

2.2.1 Mineralogy

Minerals are found in large varieties of sedimentary rock and aquatic sediments, the predominant being silicates. Depending on origin, variations can be found in specific gravity and mineral composition. Non-silicate minerals are precipitates of salts like carbonates, oxides and hydroxides, depending on chemical conditions (Winterwerp and Van Kesteren, 2004). This thesis restricts to the interaction between water and minerals, which are generally encountered as silicates and phyllo-silicates. Clay minerals are phyllo-silicates: sheet silicates which form parallel sheets of silicate tetrahedra. These sheets have a large surface area relative to their volume, and their surface is positively charged, which interacts with the ambient water. The surface charge is the main reason why clay exhibits cohesive behaviour. Clay minerals can be divided into the following groups; kaolinite (China clay), smectite (including montmorillonite), illite and chlorite. Quartz and feldspar are silicate minerals which are formed by a framework of silicon–oxygen tetrahedra, resulting in particle like structures, which are inert and non-cohesive by definition. Contrary to the shape of quartz and feldspar (so called tectosilicates), built up from three-dimensional silica tetrahedra, clay mineral are so-called phyllo-silicates and consists largely of two-dimensional silica tetrahedra with aluminium-hydroxide octahedra (gibbsite) or magnesium-hydroxide octahedra (brucite). These sheets of silica tetrahedra and gibbsite or brucite can be combined in various ways to form different clay minerals (Winterwerp and Van Kesteren, 2004). The most important difference between phyllo-silicates (clays) and silicates (silts and sands) is that the former can coagulate in the form of aggregates known as flocs.

Clay minerals can form flocs when suspended in the water column. Flocculation occurs as a result of simultaneous aggregation and break-up, and the resulting floc size is a function of the turbulence level in the water column, the suspended sediment concentration, and the electrokinetic properties of the flocs. These properties are a function of the sediment characteristics, but are also influenced by organic matter and water properties such as salinity and pH (Hiemenz and Rajagopalan, 1997).

2.2.2 Sediment mixtures and classification

The size of clay particles is a few micrometres only whereas sand particles range from a few micrometres to a few millimetres. The size of silt sized particles is found in-between clay and sand sized particles. For practical applications, the transition between clay and silt particles is set to 2 μm and between silt and sand to 63 μm (NEN 5104 Classification, see Table 2-1). It is important to realize that silt particles can still be present in the clay size range and vice versa. Therefore, to distinguish clay and silt particles both size and mineralogical analysis is required. In this thesis, silt is referred to as quartz or feldspar particles larger than 2 μm and smaller than 63 μm.

Table 2-1 Classification of soil based on metric scale (NEN 5104 Classification)[1]

Particle Type	Minimum size	Maximum size	Mineralogy
Colloidal	-	0.1 µm	
Clay	-	2 µm	Clay minerals
Silt	2 µm	63 µm	Quartz, Feldspar
Sand	63 µm	4.2 mm	Quartz, Feldspar
Gravel	4.2 mm	63 mm	Quartz, Feldspar

In natural environments, fine sediment is typically composed of (a mixture of) clay, silt, and (fine) sand. These three fractions are predominantly present in fluvial, estuarine, and coastal systems worldwide, where often either clay or sand is dominant. The contribution of each of these fractions to the total sediment composition determines the sediment behaviour. The properties of silt, sand, clay and mud are addressed hereafter. Here, mud is defined as a mixture of mainly fine-grained sediments such as clays, silt and (fine) sand, organic matter, water, and sometimes gas (Winterwerp and Van Kesteren, 2004).

The particle size distribution (PSD) of a sediment mixture is a primary discriminator to predict its behaviour. Physical properties of both cohesive and non-cohesive sediment are to a large extent related to it. The median diameter (d_{50}) is the size of which 50% of a sediment fraction is finer by weight (50th percentile of the PSD). The gradation parameter (σ_d) is the most common parameter used to describe the gradation of a sediment mixture and is defined as $\sigma_d = 0.5(d_{50} / d_{16} + d_{84} / d_{50})$, where d_{16}, d_{50} and d_{84} are the 16th, 50th and 84th percentile grain diameters, respectively. For $\sigma_d < 1.35$ a grain size distribution is referred to as uniform, which indicates a well sorted sediment mixture. In this case the PSD curve is narrow and the cumulative size distribution is rather steep. Poorly sorted fractions ($\sigma_d > 1.35$) contain a larger variety of particle sizes, which results in a wider PSD curve. It is important to realize that a well-sorted and a poorly-sorted sediment may have a different spreading of particle sizes over the various size-classes, but can have similar d_{50} (Jacobs, 2011). Another method to quantify the grading of a sediment mixture is percentile ratios, for example d_{90}/d_{10} in which the particle sizes d_{10} and d_{90} are the 10th and 90th percentile grain diameter, respectively.

The presence of a clay within a sediment mixture may introduce cohesive behaviour, depending on the percentage. Ternary diagrams are commonly used to classify sediment types by illustrating the mass fractions of sand, silt and clay in the bed (Figure 2.1). Van Ledden et al. (2004) argues that transition in erosion behaviour can be expected when *i*) the bed changes from cohesive to non-cohesive and *ii*) the sediment type determining the governing network changes.

[1] Other classifications differ in the size of the clay-silt and silt-sand boundary (e.g. ASTM D422 and BS 1377)

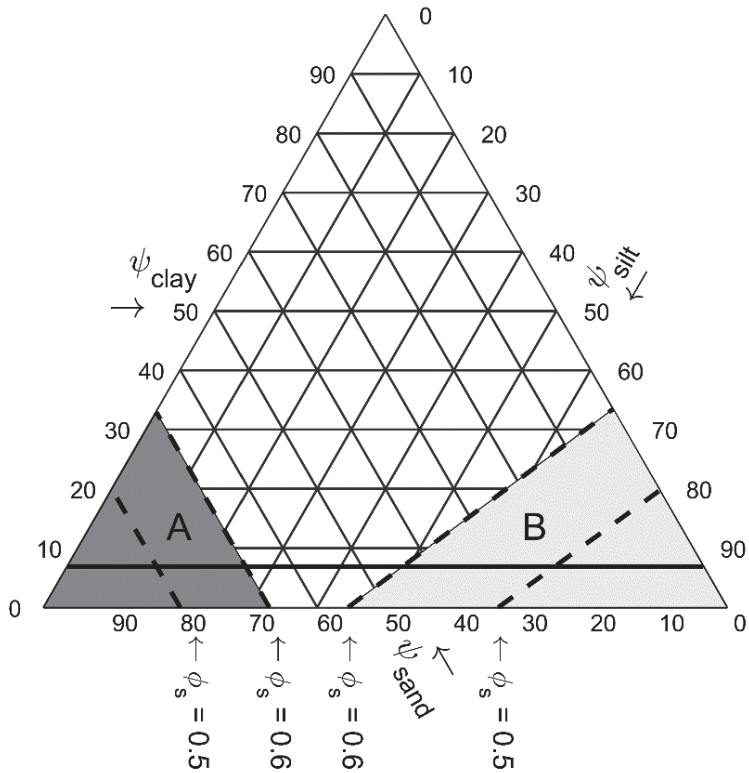

Figure 2.1 Ternary diagram with transition for cohesion and network structures. Ψ represents the solid fraction of sand, silt and clay. I = non-cohesive sand dominated, II = cohesive sand dominated, III = non-cohesive mixed, IV = cohesive clay dominated, V = cohesive silt dominated, VI = non-cohesive silt dominated network structure. Dotted lines represent transition to sand or sand-silt dominated network structures for overall solid contents of 0.5 and 0.6. The horizontal solid line represents a clay content (8%) for the transition between cohesive and non-cohesive behaviour. Shaded areas A and B indicate the area of sand and silt dominated network structures, respectively. Redrawn after Van Ledden et al. (2004).

The type of network structure of a sediment mixture depends on the overall solid content. Granular skeletons occur when sand and/or silt particles are in contact. A sand network structure occurs when the volume fraction of sand particles (Ψ_{sa}) exceeds critical values ranging from 40-50% (Floss, 1970, Kuerbis et al., 1988) to 70-80% depending on solid content (Van Ledden et al., 2004). Silt particles can form a network structure when the volume fraction of the silt particles (Ψ_{si}) is higher than 43%. In other cases, the clay fraction forms a network structure. Cohesive or non-cohesive erosion behaviour is determined by the clay content. A transition is found at clay contents (Ψ_{cl}) of 5-10%. Because of the cohesive properties of the clay particles, very open-structured networks can be formed, requiring only a small clay volume fraction relative to the pore fraction left by the silt and sand particles. Sand and silt particles can then be treated as single entities, whereas the volume-filling network is formed

by the clay fraction (Merckelbach, 2000). Subzones in the ternary diagram, which classify a soil based on the formed network structure are shown in Figure 2.1. Sand and silt dominated skeletons are positioned in areas A and B, respectively. Since its main constituents are quartz and feldspar, pure silt is classified as non-cohesive from a mineralogical point of view and it can be positioned in the bottom right corner of Figure 2.1.

2.2.3 Density definitions

Physical properties (and formulations for describing physical properties) of sediment-water mixtures often scale with bulk parameters. For example, the volume concentration of a sediment-water mixture is defined as the ratio between the volume of the solids and the total volume of the mixture. Figure 2.1 shows that bulk parameters also define the boundaries of network structures formed by either sand, silt or clay. This section presents an overview of the bulk parameters and its definition of sediment-water mixtures as used in this thesis. Fully saturated (no air) conditions are assumed.

The solid content ϕ_s is defined by the ratio between the volume of solids and the total wet volume. The porosity n is the ratio between the water volume and the total wet volume, and therefore $\phi_s + n = 1$. Densities of the solids, water and bulk material (water + solids) are defined by the ratio between the mass of the constituent and the related volume. The relation between density, solid content and mass concentration is visualized in Figure 2.2. The mass density of silt particles is typically 2650 kg/m^3.

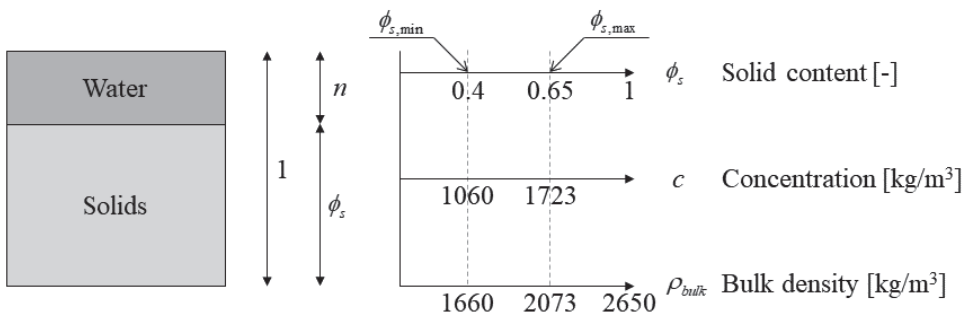

Figure 2.2 Definitions of bulk properties (based on a mass density of water 1000 kg/m^3 and a mass solid density of 2650 kg/m^3) .

The various density definitions are shown in Table 2-2. The minimum solid content ($\phi_{s,\min}$) is used to define the solid content at the loosest packing of a soil. Similarly, the maximum solid content ($\phi_{s,\max}$) is applied to define the solid content at the densest packing of a soil. Theoretically, the minimum and maximum packing of a granular soil can be estimated from the possible arrangements of uniform spheres. The loosest packing of uniform spheres ($\phi_{s,\min}$) corresponds to a solid content of 0.52 while the densest packing ($\phi_{s,\max}$) corresponds to a solid content of 0.74. These packing limits do not hold for soils with non-uniform grains. The minimum and maximum solid content of sand-silt mixtures as a function of the relative

contribution of the sand and silt fraction is defined by Van Kesteren (1996b), based on a theoretical analysis of network structures, which is supported by measurements. The solid content of a 100% silt skeleton ($\phi_{s,si}$) is found to vary between 0.4 and 0.65, whereas the solid content of a 100% sand skeleton ($\phi_{s,sa}$) ranges from 0.54 to 0.65. Sand-silt mixture can show even larger solid fractions (up to ϕ_s = 0.82) when the PSD closely follows the curve for optimum packing conditions (Fuller and Thompson, 1907).

2.3 Behaviour of sediment-water mixtures

The behaviour of sediment-water mixtures can be classified in various regimes, which are defined by the combination of shear rate $\dot{\gamma}$ (rate of the external loading with unit 1/s) and solid content ϕ_s. Each regime is characterized by the influence of sediment particles on the water flow, in relation to the shear rate. Understanding these regimes is important for understanding the behaviour of sediment-water mixtures. Various regimes are discussed in section 2.3.1. Next, the literature study- focusses on hindered settling and sedimentation theory (section 2.3.2), compaction (2.3.3) and erosion (section 2.3.4) of silt-water mixtures.

Table 2-2 Nomenclature used in this thesis

Parameter	Symbol	Definition	Relation	Unit
Specific density	ρ_s	mass density solids	mass solids / volume solids	[kg/m^3]
Density water	ρ_w	mass density water	mass water / volume water	[kg/m^3]
Bulk density	ρ_b	sediment density	mass solids / total wet volume	[kg/m^3]
Porosity	n	volume of pores / total wet volume	$1-\phi_s$	[-]
Void ratio	e	volume of pores / volume of solids	$\frac{1-\phi_s}{\phi_s}$	[-]
Mass concentration or dry density	c or ρ_{dry}	mass solids / total wet volume	$\rho_s \frac{\rho_b-\rho_w}{\rho_s-\rho_w}$	[kg/m^3]
Solid content or volume concentration of solids	ϕ_s	volume solids / total wet volume	$\frac{\rho_b-\rho_w}{\rho_s-\rho_w}$	[-]

2.3.1 Regimes

Static versus dynamic regime

Basic distinction is made between static and dynamic regimes. The static regime of a sediment-water mixture is defined as the situation in which all particles are at rest at zero shear rate.

Variation in solid content is a result of variation in packing of particles. The particle density is thereby assumed to be constant, both in time and space. The minimum and maximum solid content of a granular skeleton is thus a function of particle shapes and the grain size distribution. Coussot (2005) defined two sub-regimes within the static regime:

1. Frictional regime ($\phi_s > \phi_{s,\max}$): solid fractions exceeding the maximum possible packing for sediments and form solid rocks, which is a gradual geological process. Upon reaching $\phi_s = 1$ no more voids are present. The granular structure has disappeared.
2. Lubrication regime ($\phi_{s,\min} < \phi_s < \phi_{s,\max}$): upon reaching $\phi_{s,\min}$ particles support each other and via particle rearrangement and the solid fraction can increase up to $\phi_s = \phi_{s,\max}$. Direct contact between particles exists.

The mechanical properties of sediment-water mixtures become manifest when exposed to shear. For that, Coussot (2005) defines the dynamic regime without horizontal water flow as follows:

3. Collision regime ($\phi_s < \phi_{s,\min}$): solid particles do not form a network structure and particles settle in water. As the total volume of water and particles remains the same, the water has to move in opposite direction as the particles, which influences the settling of other particles.

Laminar versus turbulent response

At low flow velocities and low concentration the streamlines are straight and the flow is laminar. At larger flow velocities, turbulent motions generate non-orderly flow patterns, unsteady vortices and rapid variation of pressure and velocity in space and time. The transition between laminar and turbulent flow can be expressed with the dimensionless Reynolds number, relating the inertial forces to the viscous forces through:

$$\mathrm{Re} = \frac{uL}{\nu} \tag{2.1}$$

where u is the flow velocity, L a characteristic length and ν is the fluid's kinematic viscosity (1.004×10^{-6} m^2/s for water of 20°C). The flow around a settling particle can also be considered laminar or turbulent, and expressed with the Reynolds number. The diameter of the particle is hereby the characteristic length scale: for large particles the flow around the particle is turbulent whereas for small particles the flow is laminar. Silt sized particles settle in a laminar (Stokes) regime whereas particles with $d > 100$ μm settle in a turbulent regime.

The regime in which sand sized particles and silt sized particles settle is different. Generally, the fluid movement around particles with $d < 100$ μm is laminar, causing silt particles to settle in the Stokes regime (see the next subsection). As a result, the particle shape is here of minor influence on the settling velocity. Another consequence of the small particle sizes in the silt

range is the small settling velocity, resulting in long time during which particles can stay in suspension.

Within the collision regime, the type of dynamic response changes significantly when exposed to horizontal flow. The laminar versus turbulent response and the macro-viscous versus grain-inertia response are considered relevant for positioning the behaviour of silt-water mixtures, and are summarized next.

Macro-viscous versus grain-inertia response

During flow conditions with high solid content (but below $\phi_{s,\min}$), the regime is influenced by particle-particle collisions. Three regimes are proposed by Bagnold (1954): the macro-viscous regime, the transitional regime and the grain-inertia regime. In the macro-viscous regime, the sediment-water mixture behaves like a fluid and the viscous fluid stresses dominate the grain collision stress. In the grain-inertia regime, the grain collision stresses are dominant. The ratio between grain collision stress to viscous fluid stresses in a granular flow with interstitial Newtonian fluid is expressed by the Bagnold number. The Bagnold number is used to distinguish the various regimes and is defined as:

$$Ba = \frac{\rho_s d^2 \lambda^{1/2} \dot{\gamma}}{\mu} \qquad 2.2$$

In which ρ_s is the particle density, d is the particle diameter, $\dot{\gamma}$ is the shear rate and μ is the dynamic viscosity of the interstitial fluid. The parameter λ is the linear concentration defined as:

$$\lambda = \frac{1}{\left(\phi_{s,\max} / \phi_s\right)^{1/3} - 1} \qquad 2.3$$

The macro-viscous regime is characterized by low Bagnold numbers (Ba < 40). At large Bagnold numbers (Ba > 450) the granular flow is in the grain-inertia regime. At interstitial Bagnold numbers (40 < Ba < 450), the flow is in a transitional regime. Figure 2-3 shows the variation of the Bagnold number as a function of solid content for various shear rates and particle sizes (63, 200 and 500 μm). Since the number of grain-grain collision increases with concentration and shear rate, more energy is required to keep the particles in suspension. With decreasing particles size however, the flow is able to keep smaller particles (silt) suspended at very high concentration in the macro-viscous regime.

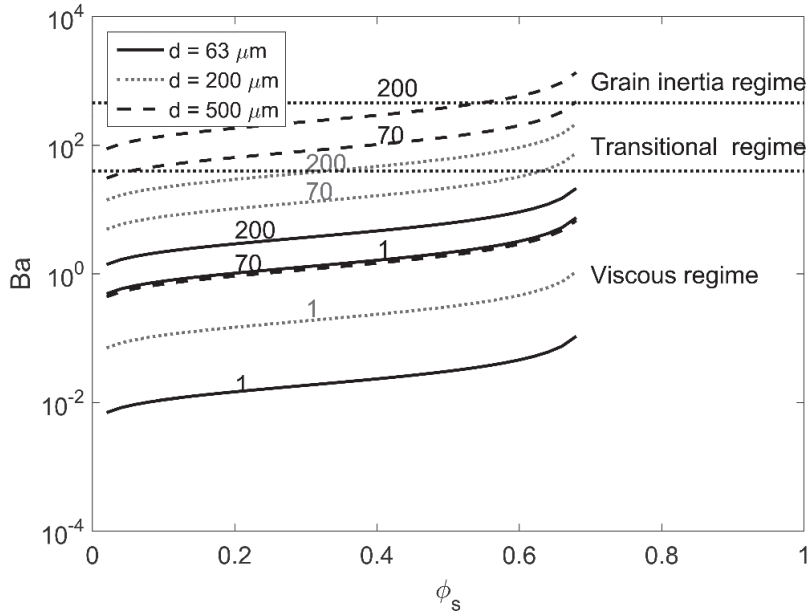

Figure 2-3 Bagnold number *Ba* as function of solid content. Shear rates are indicates by numbers along lines.

Drained versus undrained soil mechanical response

The drained shear strength is the shear strength of the soil when pore-water pressures, generated during the course of shearing the soil, are able to dissipate during shearing. Drained conditions imply that no pore-water over- or underpressures develop in the soil and hence pore-water pressure gradients are negligible. Conceptually, *the* undrained shear strength of a soil does not exist as it depends on a number of factors. Undrained conditions occur when the shear rate is faster than the rate at which the induced pore-water pressure gradients can dissipate.

For loosely packed intermediate permeable soils, such as silt beds, the shear strength depends on the shear rate (Randolph and House, 2001, Chung et al., 2006). Figure 2-4 shows a range in shear strength in transition from undrained to drained loading conditions as the shear rate is reduced, obtained from experiments in a low permeability soil. The dimensionless number V on the x-axis is a Péclet-like number (explained below) and is used to express the variation from drained to undrained response. The results show fully drained condition for vd/c_v around 0.5, and undrained conditions for vd/c_v greater than 20.

Whether the erosion process of cohesive sediment beds is drained or undrained is assessed using the Péclet number by Winterwerp and Van Kesteren (2004). The Péclet number for pore-water pressure dissipation is defined as:

$$Pe_w = \frac{V\ l}{c_i} \qquad 2.4$$

where l is a length scale and c_i is the isotropic consolidation coefficient. The consolidation coefficient c_i for the dissipation of pore-water pressure is strongly dependent on the permeability and packing of the bed. As a result of shearing, deformations occur, which induce pore-water flow. If the permeability is low, pore-water over- and underpressures can develop. The increase in pore-water pressure Δp^w, divided by the pore-water pressure increment in undrained loading as a result of the applied total isotropic stress (stationary external loading) Δp, is shown in Figure 2-5 for drained and undrained conditions as a function Pe_w.

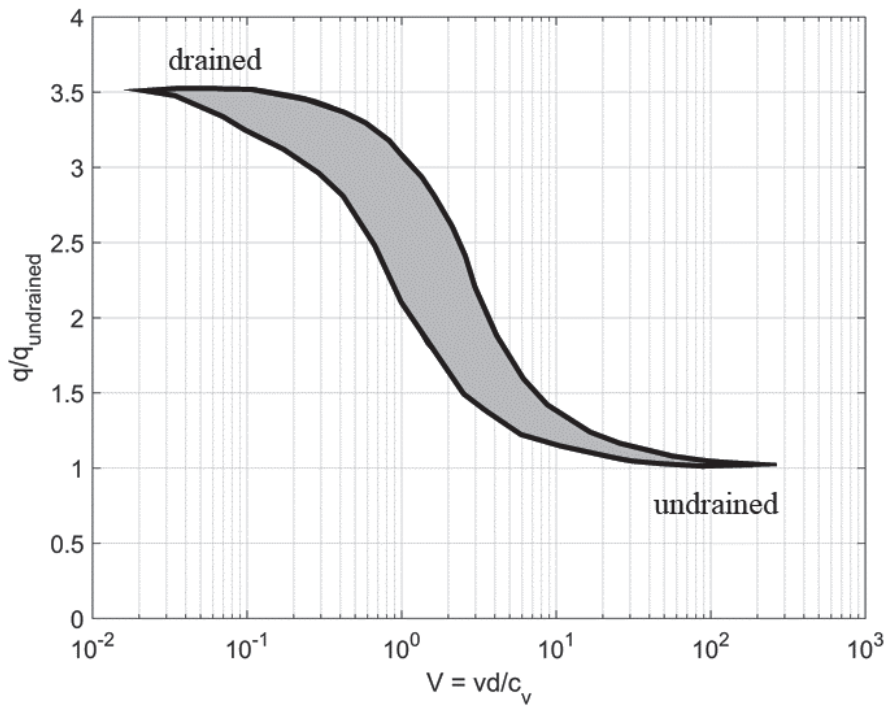

Figure 2-4 Experimental derived range of constant penetration test results, q is the soil resistance, v is the shear velocity, *d* is a length scale and c_v is the consolidation coefficient. Shaded area represents the variation in normalized resistance as function of deformation velocity V (Redrawn after Randolph and House 2001).

Fully drained conditions prevail near the origin of Figure 2-5 at $Pe_w < 1$, represented by a straight line in the diagram, tangent to the fully drained curve. At high Pe_w ($Pe_w > 10$) the curve asymptotically approaches fully undrained conditions.

Freshly deposited silt beds can be considered as low permeability soils and are therefore likely to show shear rate dependant undrained behaviour. The possible undrained soil mechanical behaviour of silt beds in combination with a low permeability is therefore of importance when studying erosion behaviour.

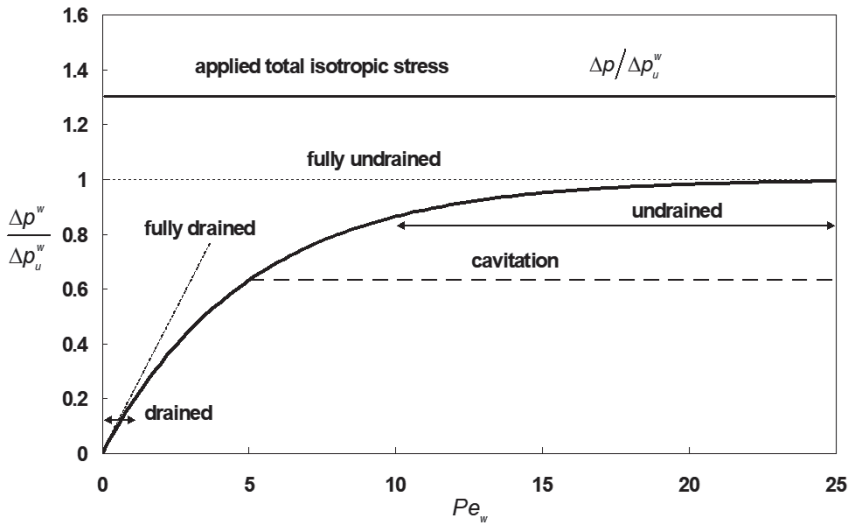

Figure 2-5 Response of pore-water pressure to external loading for drained and undrained conditions [after Winterwerp and Van Kesteren (2004)].

Concept of critical state

The critical state concept is introduced by Schofield and Wroth (1968a) and is applied to the erosion of sand-mud mixtures by Jacobs (2011) and Winterwerp et al. (2012). The critical state concept can be used to relate the characteristics of a sediment-water mixture to mechanical behaviour. The state of a soil indicates a specific relationship of packing and applied forcing. Generally, three types of soil behaviour may occur upon yielding of which two of these types exhibit volume variations which generate pore-water flow. Contraction occurs when the total volume of a soil decreases during yielding, which typically occurs for loosely packed soils. Dilation occurs when the total volume increases, which occurs for more densely packed soils. The third kind of yielding occurs at the critical state, during which no pore volume variations occur and hence no pore-water pressure gradients are generated. Latter type of yielding occurs for a specific relation between the packing and the stress state (Jacobs, 2011).

2.3.2 Hindered settling and sedimentation theory

The deposition process of silt-water mixtures can be described with a particle flux term for the hindered settling regime and a particle flux term for the compaction regime. A sketch of the flux function is presented (Figure 1-1). Following the static and dynamic regime in section 2.3.1, it is proposed to divide the flux function for silt-water mixture into three phases (which may partly overlap). These are:

1. A hindered settling phase, which ends upon reaching the minimum solid content $\phi_{s,\min}$;
2. A phase of compaction, which occurs between the loosest and densest packing of the bed, after silt particles have formed a network structure and effective stresses start to build up;
3. A phase beyond the densest packing where geological processes play a role. This phase is not further addressed in this thesis.

Quantification of the flux functions during the different phases is key in understanding the behaviour of silt.

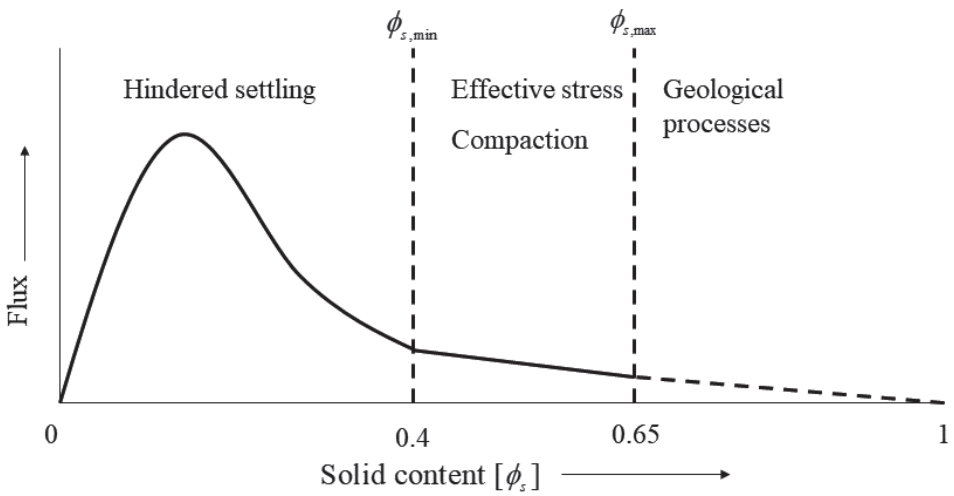

Figure 2-6 Sketch of the flux as function of the solid content ϕ_s. Three processes are incorporated in the flux: hindered settling, the generation of effective stress and the effect of compaction. Minimum and maximum solid content follow from the loosest and densest packing of a 100% silt skeleton (Winterwerp and Van Kesteren, 2004).

Settling and hindered settling

Silt settles as individual particles (and not as aggregates such as often observed for clay particles). The particle Reynolds number is an important discriminator in determining the settling regime of individual particles. Within the range of silt-sized sediment, the particle Reynolds number is low ($Re_p < 1$), indicating laminar flow around a particle when settling in an infinite fluid. Physically, this settling velocity represents a balance between the fluid drag force and the gravitational force. In the regime of laminar flow, Stokes' law (Equation 2.5) can be used to calculate the settling velocity of a single particle $w_{s,0}$.

$$w_{s,0} = \frac{(s-1)gd^2}{18\nu} \quad \text{for} \quad \mathrm{Re}_p = \frac{\mathrm{w}_{s,0} d}{\nu} < 1 \qquad 2.5$$

where s is the specific density of the solids, g the gravitational acceleration, d is the particle diameter and ν is the fluid's kinematic viscosity. According to Van Rijn (1993), equation 2.5 is also valid for non-spherical sediment particles (with d = sieve diameter; which is the diameter of a sphere equal to the length of the side of a square sieve opening through which the given particle will just pass (Van Rijn, 1993)) in the range of 1 μm < d < 100 μm.

The settling velocity of individual particles in a settling sediment-water mixture is usually related to the single particle settling velocity, combined with a hindrance function $f(\phi)$, where ϕ is the volumetric fractional concentration of the settling units, defined as the solid content relative to the solid content at the minimum packing of particles in the bed $(\phi_s / \phi_{s,\min})$. The retardation of individual units in the hindered settling regime is often expressed by the $(1-\phi)$ term. Richardson and Zaki (1954) studied the hindered settling effect of glass particles with sizes in the range of 35 μm to 1000 μm and alumina powder with a particle size of about 5 μm. Scott (1984) incorporated these retardation effects in a modified Richardson and Zaki (1954) hindered settling formulation (further abbreviated as the RZ formulation) for granular mixtures:

$$w_s = w_{s,0}(1-\phi)^n \qquad 2.6$$

where n is an empirical exponent varying between 1 and 5, which is constant for a particular particle size. The exponent in equation 2.6 is often referred to as the Richardson-Zaki exponent n (further abbreviated as the RZ exponent) and is a bulk parameter. Baldock et al. (2004) found a dependency between the RZ exponent and particle size, and elaborated this dependency for particles within the size range 200 μm < d_{50} < 1000 μm), resulting in an expression for n:

$$n = 4.4(d_{50,ref} / d_{50})^{0.2} \qquad 2.7$$

where $d_{50,ref}$ = 200 μm. It is not yet known to what extent equation 2.7 is valid for the silt size range. Wan and Wang (1994) found a dependency between n and grain size based on experimental data, resulting from work done by Qian (1980b). Maximum constant values for n of 4.65 for Reynolds number smaller than 0.4 and minimum values for n of 2.5 for Reynolds numbers surpassing 10^3 – 10^4 were found. Xia and Wang (1982) conducted experiments with uniform sand (d_{50} = 67 μm) and obtained an n-value of 7, which is larger than the maximum n-value found by Qian (1980b) and larger than predicted by the formulation by Baldock et al. (2004), the latter being 5.6. Qian (1980b) also performed settling experiment with non-uniform fine sand with d_{50}'s of 61 μm and 87 μm. From these experiments it is concluded that non-uniform particles follow the same law as the one for uniform particles. However, extrapolation of equation 2.7 into the silt size particle range leads to unrealistic high values of n (n > 5.5). Chien and Wan (1998) have shown that an exponent n = 7 performs well within the silt size range, but also refer to studies where n becomes constant with decreasing particle size (Figure 2-7). Extensive overviews of (group) settling velocity formulas are presented in Van Rijn (1993) and Wan and Wang (1994). Most formulae however, were derived from experiments with particles larger than 63 μm. Therefore, the applicability to silt-sized material remains questionable.

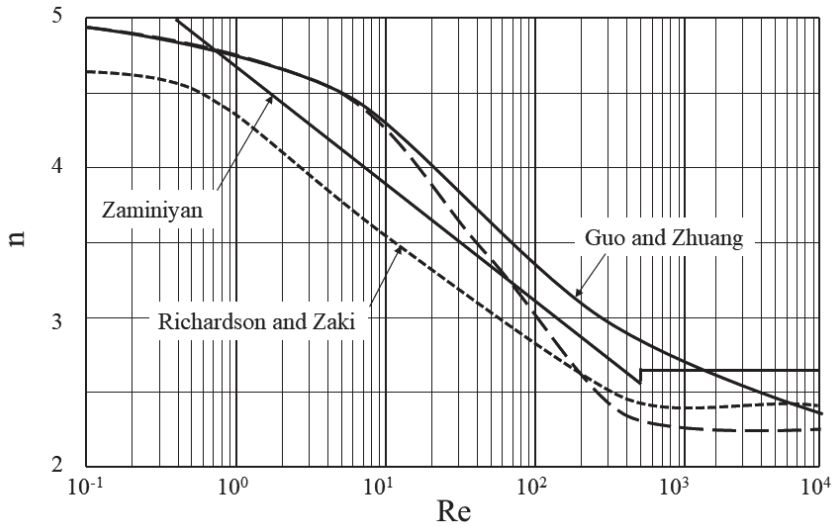

Figure 2-7 Relationship between *n* and particle Reynolds number [redrawn after Chien and Wan (1998)]

Sedimentation theory

Kynch (1952) studied the sedimentation of highly concentrated sediment-water mixtures in which the settling process was determined from a continuity equation (see Dankers (2006) for a thorough elaboration on Kynch's theory). First, a vertical particle flux is defined as:

$$S = w_s \phi \tag{2.8}$$

In which w_s is the effective settling velocity and ϕ is the volumetric concentration. Hindered settling effects are introduced by assuming that effective settling velocities reduce with increasing concentration;

$$w_s = w_{s,0} f(\phi) \tag{2.9}$$

Where $f(\phi)$ is a function describing the effects of concentration on the settling velocity, $f(0) = 1$ and $f(1) = 0$. The vertical one-dimensional volume balance equation can be written as:

$$\frac{\partial \phi}{\partial t} + \frac{\partial S}{\partial z} = 0 \tag{2.10}$$

Where *t* is time and *z* is the vertical coordinate, positive downward. Combining equations 2.8, 2.9 and 2.10 results in:

$$\frac{\partial \phi}{\partial t} + w_{s,0} F(\phi) \frac{\partial \phi}{\partial z} = 0 \tag{2.11}$$

With

$$F(\phi) = \frac{d}{d\phi}\left[\phi f(\phi)\right] \qquad 2.12$$

Equation 2.11 is a 1-D wave equation describing the settling of sediment-water mixtures in which $w_{s,0}$ is constant (uniform sized particles or aggregates). The wave equation is hyperbolic and its solution allows for the formation of shocks. It can be solved by integrating along characteristic lines in the (z,t) plane (method of characteristics). These characteristics lines are given by Equation 2.13:

$$\frac{\mathrm{d}z}{\mathrm{d}t} = w_{s,0}F(\phi) = w_{s,eff} \qquad 2.13$$

By analysing lines of equal solid content (isolutes) measured during sedimentation experiments, the effective settling velocity $w_{s,eff}$ can thus be determined. This methodology will be applied in **Chapters 3 and 6** to analyse measurements from deposition experiments.

2.3.3 Compaction

Densification is an increase in solid content of a sediment bed in time, and can be the results of consolidation or compaction. For mud, consolidation occurs when a space-filling network is formed by cohesive sediment flocs. The flocs below a certain reference plane have to carry the weight of the sediment above this plane at equilibrium. The weight of sediment above that plane induces a stress within the bed, which expels pore-water from the flocs and the spaces between the flocs. Freshly deposited flocs largely consist of water which is squeezed out during the process. During consolidation, the effective stress increases and the pore-water over pressure reduces.

Silt does not form flocs, and therefore the densification mechanism is different from the densification mechanics of cohesive sediment. Nevertheless, silt beds have been observed to exhibit cohesive-like densification behaviour, which, in this thesis, is referred to as compaction. Roberts et al. (1998) and Lick et al. (2004) observed that the solid content of silt beds may increase with time, and that erosion rates of these beds decrease with increasing solid content. Unfortunately, this change in solid content is not explained as no pore-water pressure measurements were carried out during the compaction process, and therefore no understanding of the physical backgrounds of the compaction process could be obtained. Since silt does not flocculate, it is suggested that the permeability of the bed primarily influences compaction. For silt beds, compaction is considered to be a more appropriate term to express the dissipation of excess pore-water pressure and densification since silt particles cannot be squeezed or broken, as occurs during the consolidation of cohesive sediment beds.

An analogy between the compaction process of silt beds and the consolidation process of cohesive sediment beds is attributed to the low permeability of both types of beds. Excess pore-water pressures, induced by the overlying bed, cannot flow out of the bed directly. Over time, these excess pore-water pressures dissipate, thereby increasing the solid content of the bed. This compaction process is likely to be governed by pore-water pressure dissipation rates and may be much faster for silt beds than for cohesive sediment beds. **Chapter 4** of this thesis elaborates on the compaction of silt beds.

2.3.4 Erosion

The rate of suspended sediment transport is governed by erosion and sedimentation processes. For particles, the initiation of motion depends on the balance between the drag and lift force due to the flow and the gravitation forces on the particle. The erosion behaviour of non-cohesive material, as a function of particle size, is reasonably well known from Shields' (1936) diagram for initiation of motion. Here, θ_{cr} (equation 2.14) is the critical Shield parameter which depends on hydraulic conditions near the bed, the particle shape and the particle position relative to other particles:

$$\theta_{cr} = \frac{\tau_{cr}}{(\rho_s - \rho_w) g d} = \frac{u_{*cr}^2}{\Delta g d} \qquad 2.14$$

$$D_* = \left(\frac{(s-1)g}{\nu^2} \right)^{1/3} d_{50} \qquad 2.15$$

in which u_{*cr} is the critical bed shear velocity and τ_{cr} is the critical bed shear stress. The hydraulic conditions near the bed are expressed by the Reynolds number Re. Many experiments have been performed to determine θ_{cr} as a function of Re, of which overviews are presented in Van Rijn (1993) and Miedema (2011). The Shields curve in terms of θ_{cr} as a function of Re is not considered practical since the critical bed shear stress can only be obtained by iteration. A more practical way is to present the shield curve in terms of the dimensionless mobility number θ and the dimensionless particle diameter D_* (Figure 2-8).

In general, three regimes are distinguished in Shield's diagram. For the large particles (d_{50} > 6-7 mm) the critical mobility number is independent of particle size and becomes constant. For intermediate sized particles (approximately 500 μm < d_{50} < 6-7 mm) the critical mobility number decreases with decreasing grain size. For particles with d < 500 μm, the critical mobility number increases with decreasing grain size. The most general explanation for this latter increase lies in the compensation for the velocity term in Shield's stability parameter, which is no longer valid in the viscous sub-layer. In the range of silt sized (2 μm < d_{50} < 63 μm) material (grey area in Figure 2-8) however, additional (cohesive) forces start influencing the erosion threshold. In literature however, it is recognized that the Shields criterion does not apply to this size fraction.

Attempts to quantify and model the erosion of silt beds are based on empirical (Dou et al., 2001) and mechanistic (Roberts et al., 1998, Lick et al., 2004) approaches. In addition, various explanations for apparent cohesion are given in which the physical mechanisms are described. These mechanisms are related to interparticle forces, or are related to bulk properties of the sediment (Miedema, 2011, Ternat et al., 2008). For dredging applications, Van Rhee (2011) has presented a pick-up function for sediment erosion under the influence of high flow velocities. In this study an altered Shields value has been derived by taking the permeability into account.

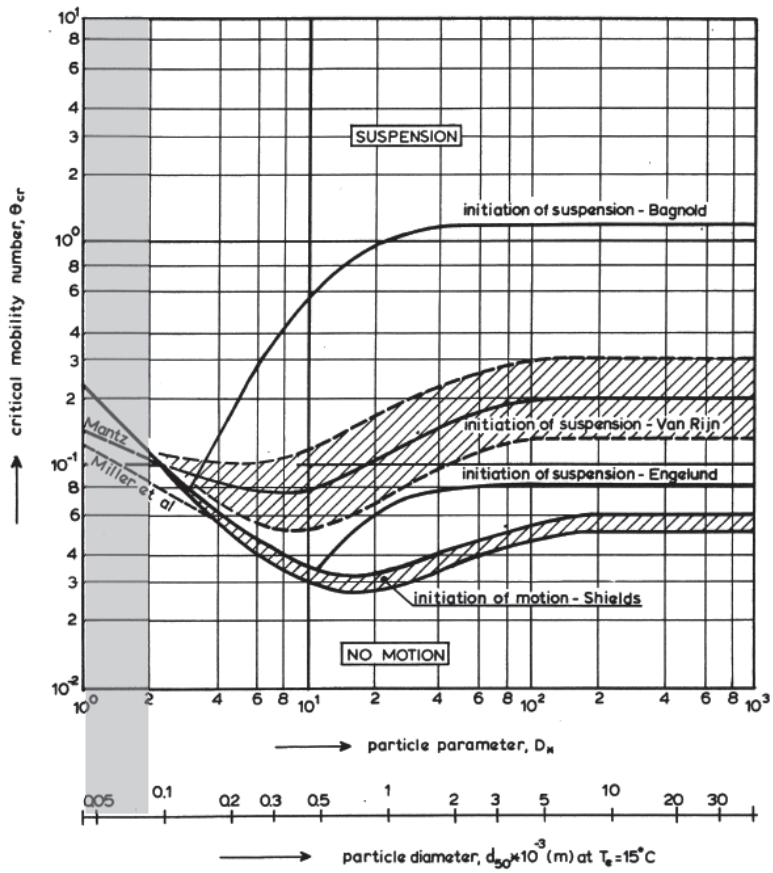

Figure 2-8 Initiation of motion and suspension for a current over a plane bed, $\theta = f(D_*)$, (Van Rijn, 1989).

Roberts et al. (1998) observed that for pure silt beds, the critical bed shear stress for erosion increased with increasing solid content, indicating apparently cohesive behaviour. They observed erosion of bed sediments as chunks, referred to as undrained erosion or mass erosion. The phenomena mass erosion is known from cohesive sediment.

Mass erosion is also observed in the Yellow River, where sediment blocks are eroded from the bed, emerge at the water surface, and are transported downstream (Wan and Wang, 1994). Mass erosion is the result of bulk failure of the sediment and is explained from a soil mechanical perspective by Winterwerp and Van Kesteren (2004), and Jacobs (2011) and Winterwerp et al. (2012). They have found that the dominating erosion mechanism in cohesive sediment beds is a soil mechanical response of the bed to the hydrodynamic forcing for which three erosion modes are defined; floc erosion, surface erosion and mass erosion. Similar types

of behaviour are expected to occur during the erosion of silt beds, although the physical mechanisms may differ. Based on the stress state of the bed, the shear rate and the timescale of the beds response, the following erosion modes are expected to occur in silt beds:

1. Particle erosion: individual particles are picked up from the bed. The upward flow-induced force should exceed the downward gravitational force.
2. Surface erosion: occurs when the bed is at or below its critical state, i.e. the bed water content has to increase before failure (erosion) can occur. To increase the bed water content, water has to enter the bed, in case of surface erosion by inflow through the bed surface. For granular sediment this process is known as volumetric dilatancy.
3. Mass erosion: the difference between surface erosion and mass erosion is determined by the timescale of the loading. Mass erosion is considered an undrained process whereas surface erosion is considered a drained process.

Surface erosion of silt beds will be explained from a soil mechanical perspective in **Chapter 5** of this thesis.

2.4 Summary

From the literature study it has become clear that the behaviour of sand and mud has received much more scientific attention than that of silt-water mixtures. No specific literature on hindered settling and compaction of silt beds is found. The little available research mainly focuses on erosion of silty sediment beds, but ignores deposition processes. Based on the information available, it seems that silt can show apparently cohesive behaviour while compacting and eroding. In these processes, the permeability parameter seems to be of paramount influence. The settling behaviour of silt is expected to show similarities with both non-cohesive and cohesive settling behaviour, since the physical processes are partly similar. These suggestions are derived from field observations (Wan and Wang, 1994), laboratory experiments (Roberts et al., 1998) and modelling work (Van Maren et al., 2009a, Van Maren et al., 2009b).

The underlying physical mechanisms resulting in the apparently cohesive behaviour of silt-water mixtures remain undefined. At present, a widely accepted descriptions of the sedimentation and erosion behaviour of silt dominated sediment mixtures is lacking. Therefore, the properties and behaviour of silt-water mixtures will be investigated and quantified through a series of laboratory experiments in **Chapter 3** (hindered settling), **Chapter 4** (sedimentation and compaction) and **Chapter 5** (erosion). The link with natural silt-dominated sediment system is made in **Chapter 6**, where dedicated experiments with natural silt-dominated sediment mixtures are discussed.

Chapter 3

Hindered settling of silt

3 Hindered settling of silt[2]

3.1 Introduction

The settling of sediments can be investigated through analytical and empirical methods. The first method is based on sedimentation theory resulting from mass and volume balance equations obeying physical laws. Herein, settling processes are studied by observing the bulk behaviour of settling sediment-water mixtures. Pioneering work in this field has been done by Kynch (1952) and more recently Bustos (1999). The second method is based on laboratory experiments, generally leading to empirical formulations. An important study within this field is done by Richardson and Zaki (1954) resulting in a formulation that relates settling velocity to particle size and concentration. Later, this formulation was slightly improved by Scott et al. (1984). Dankers and Winterwerp (2007) combined these methods to obtain a physics-based formulation for the hindered settling of mudflocs, resulting in an improved hindered settling formulation. The present research follows the methodology of Dankers and Winterwerp.

During periods of low energetic conditions, a sediment bed may accrete as a result of deposition. Deposition is governed by the settling velocities of sediment particles and the sediment concentration. Therefore, the settling velocity is a key parameter in quantifying the deposition flux. **Chapter 2** (literature study) recounts that settling of individual sediment particles, and hindered settling of (highly) concentrated sediment suspensions are treated extensively in literature for both sand and cohesive sediment. However, data and information on the hindered settling of silt is scarce, possibly because of the rare occurrence of silt-dominated river and associated coastal systems. Another reason might be the difficulty of isolating silt sized particles.

The largest difference between the settling of sand sized particles and silt sized particles is the regime in which these particles settle. Generally, the fluid movement around particles with $d <$ 100 µm is laminar, causing silt particles to settle in the Stokes regime. As a result, the particle shape is here of minor influence on the settling velocity. Another consequence of the small particle sizes in the silt range is the small settling velocity, resulting in long times during which particles can stay in suspension. This leads to the possible occurrence of high concentrations of suspended silt. This process precedes the phenomenon of mass deposition, which is characteristic for the Yellow River.

In this chapter more insight into the physical processes governing the hindered settling behaviour of silt is obtained by using state-of-the art sedimentation theory, which is validated by means of laboratory experiments.

3.2 Hindered settling formulations

In this section, a new hindered settling formulation (HSF) for silt is derived in analogy with the work of Winterwerp (2002) and Dankers and Winterwerp (2007). Later, this formulation is validated with laboratory experiments and compared with existing HSF's for (fine) sand. Some basic principles on hindered settling effects are discussed first, of which details have been

[2] *Parts of this chapter are based on Te Slaa, S., van Maren, D. S., He, Q., & Winterwerp, J. C. (2015). Hindered settling of silt. Journal of Hydraulic Engineering, 141(9), 04015020.*

addressed in section 2.3.2. Mandersloot et al. (1986) recognized three regimes in deposition of particles in a liquid:

1. The dilute or clarification regime, in which the settling particles move individually although not necessarily without some fluid-dynamic interaction;
2. The hindered settling regime which is normally attained only at substantial volumetric concentrations of the settling particles;
3. The compaction or consolidation regime, in which freshly deposited particles are compressed by the overburden of additional particles that settle on the bed.

This chapter focuses on the first two regimes for which the Stokes' settling velocity (Stokes, 1851) for individual particles is used as starting point:

$$w_{s,0} = \frac{(s-1)gd^2}{18\nu} \quad \text{for} \quad \mathrm{Re}_p < 1 \tag{3.1}$$

The single-particle settling velocity may increase due to flocculation processes or decrease due to hindered settling. Flocculation processes however, require a clay fraction, which is not considered here. The reduction of hindered settling is often parameterized with semi-empirical Richardson and Zaki (1954) formulation:

$$w_s = w_{s,0}(1-\phi)^n \tag{3.2}$$

in which ϕ is the volumetric solid content, defined as the solid content relative to the solid content at the minimum packing of particles in the bed ($\phi_s / \phi_{s,\min}$), and n is an empirical exponent, also referred to as the Richardson-Zaki (RZ-) exponent. Apart from the influence of particle shape, the RZ-formulation assumes to implicitly incorporate all processes related to hindering the settling velocity of individual particles in clear water. These processes are extensively discussed by Winterwerp and Van Kesteren (2004). Here, it is assumed that physico-chemical effects do not influence the hindered settling of silt. Hence, aggregation or coagulation does not occur in fine grained sediment-water mixtures. Therefore, the governing processes for hindered settling of particles are:

1. *Return flow and wake formation*: A falling particle generates a return flow and a wake, reducing the effective settling velocity of other particles which are affected by this return flow. The return flow is the net upward directed flow, generated by the downward moving particle; the upward directed flow closes the volume balance (with respect to a fixed reference frame) of the interstitial fluid. This return flow due to settling stops upon reaching the minimum solid content of the bed. Therefore, this retarding effect should scale with $(1-\phi_s / \phi_{s,\min})$.

2. *Increased viscosity:* The collisions of granular particles are elastic. The rheological behaviour of granular materials is thus dependent on whether the individual particles are in contact or not. Such collisional effects are accounted for in the increased viscosity. The viscosity increases exponentially with solid content since the number of particle collisions is a function of the surface area of all particles together. No formulations exist for the increased viscosity of silt-water mixtures. However, two formulations for the increased

viscosity of granular material exist. The first formulation, proposed by Krieger and Dougherty (1959), is derived from theoretical arguments:

$$\mu_{eff} = \mu_0 (1 - \phi_s / \phi_{s,\max})^{-2.5\phi_{s,\max}} \quad 3.3$$

where $\phi_{s,\max}$ is the solid content at the maximum packing of the particles. The second equation, derived by Quemada (1985), is essentially empirical and is obtained from fitting datapoints:

$$\mu_{eff} = \mu_0 \left(1 + \frac{3}{4} \frac{\phi_s}{\phi_{s,\max} - \phi_s}\right)^2 \quad 3.4$$

3. *Buoyancy or reduced gravity:* Following the same reasoning as above, the settling velocity of an individual particle settling in the remainder of a suspension with increased bulk density decreases with a factor $(1-\phi_s)$.

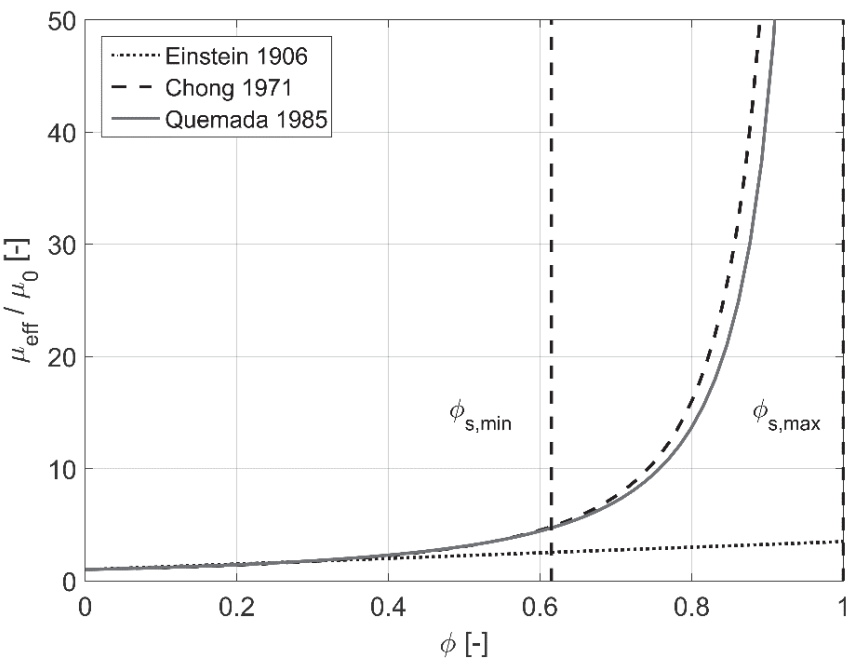

Figure 3-1 Normalized increased viscosity according to equations 3.3, 3.4 and Einstein (1906)

In both formulations for the effective viscosity, μ_{eff} approaches infinity when ϕ_s approaches $\phi_{s,\max}$, but remains finite for ϕ_s close to $\phi_{s,\min}$ (Figure 3-1). In the range between $\phi_{s,\min}$ and $\phi_{s,\max}$ particle movement is still possible, and the mixture is expected to develop yield strength. Note that both formulations reduce to Einstein's formulation for increased viscosity for small

solid contents. In the following, viscosity formulations 3.3 and 3.4 are tested in HSF's, as none has been derived specifically for silt.

Winterwerp (2002) combined the three mentioned effects for flocculated matter in a HSF of the form:

$$w_s = w_{s,0} \langle \text{Return flow} \rangle \text{ x } \langle \text{Bouyancy} \rangle \text{ x } \langle \text{Increased viscosity} \rangle \qquad 3.5$$

accounting for all three effects. Substituting equations 3.3 and 3.4 into equation 3.5 yields two HSF's for granular, elastic material which may be valid for silt-sized sediment:

$$w_s = w_{s,0} \frac{(1-\phi_s / \phi_{s,\min})^m (1-\phi_s)}{\left(1-\phi_s / \phi_{s.\max}\right)^{-2.5\phi_{s,\max}}} \qquad 3.6$$

$$w_s = w_{s,0} \frac{(1-\phi_s / \phi_{s,\min})^m (1-\phi_s)}{\left(1+\frac{3}{4}\frac{\phi_s}{\phi_{s,\max}-\phi_s}\right)^2} \qquad 3.7$$

The introduction of $\phi_{s,\min}$ and $\phi_{s,\max}$ in the HSF's 3.6 and 3.7 implies that increased viscosity, and return flow and wake formation scale with different solid contents. Upon reaching the minimum solid content, a network of particles is formed and settling velocities reduce to zero. Therefore, scaling of the return flow and wake formation with $\phi_{s,\min}$ seems justified. Previous argumentation implies that the validity of the HSF's ranges between $0 < \phi_s < \phi_{s,\min}$. The scaling parameter of the increased viscosity is more difficult to determine, since a clear definition of the viscous regime is difficult to give. Since $\phi_{s,\min}$ and $\phi_{s,\max}$ depend on particle size and particle size distribution (Winterwerp and Van Kesteren, 2004), the influence of the difference between the minimum and maximum solid content $(\Delta\phi_s = \phi_{s,\max} - \phi_{s,\min})$, is examined for HSF 3.6 (Figure 3-2b).

The exponent *m* in equations 3.6 and 3.7 is introduced by Dankers (2006), while deriving a hindered settling formulation for mud, and accounts for possible non-linear effects. For *m* = 1 the return flow is linear and only the volume balance of sediment settling in a liquid is accounted for. Other hydrodynamic effects generated by the settling particles (for example acceleration and deceleration of flow, and the curvature of streamlines) are incorporated in the exponent m (Dankers and Winterwerp, 2007). Dankers' analysis is valid for uniform sediment sizes and cannot be applied directly to a non-uniform silt mixture.

As part of this thesis, the behaviour of the widely accepted RZ formulation 3.2 is compared with equations 3.6 and 3.7 in the silt size range. For this purpose, the parameter *n* in equation 3.2 is set to 4.4, the value corresponding to the smallest tested particle size (200 μm). For particles larger than 200 μm, the *n* value increases with increasing particle size (Baldock et al., 2004). In equations 3.6 and 3.7, the parameters $\phi_{s,\min}$ and $\phi_{s,\max}$ are set to 0.40 and 0.64, corresponding to the minimum and maximum solid content of a silt dominated skeleton, respectively (Figure 3-2a). In addition, the results for equations 3.6 and 3.7 are shown with *m* = 1 and *m* = 2, accounting for possible nonlinear effects in the return flow and wake formation. Both formulations for increased viscosity yield almost the same hindered settling behaviour:

the maximum difference in $w_{s,eff} / w_{s,0}$ does not exceed 1% over the whole range of ϕ_s. At both low $(\phi_s < 0.04)$ and high ($\phi_s > 0.35$) solid contents, equations 3.2, 3.6 and 3.7 are in good agreement as well. In these regions differences in $w_{s,eff} / w_{s,0}$ do not exceed 2%. In the range of $0.04 < \phi_s < 0.35$, the difference in $w_{s,eff} / w_{s,0}$ between equation 3.2 and both equations 3.6 and 3.7 increases first, reaches a maximum of 6% around $\phi_s = 0.2$ and then decreases again. Here, equation 3.2 gives lower values. The differences are the most pronounced in the range $0.05 < \phi_s < 0.25$.

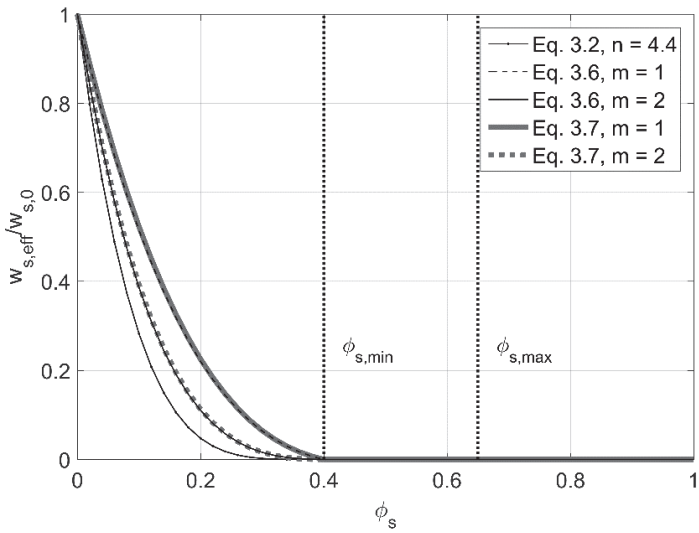

(a)

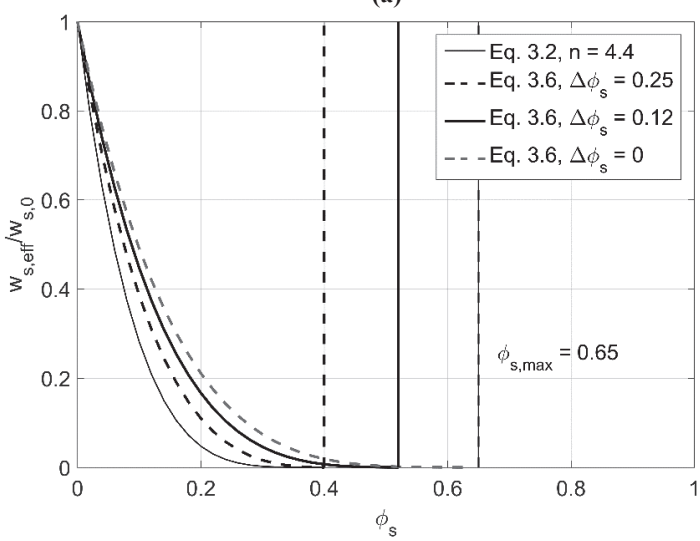

(b)

Figure 3-2 Comparison of the differences in behaviour of HSF's 3.2, 3.6 and 3.7 (a) and sensitivity plot of variation in $\Delta\phi_s$ in equation 3.6 (b).

The presented results are quantitatively similar to variations between the minimum and maximum solid content ($\Delta\phi_s = \phi_{s,\max} - \phi_{s,\min}$) in equation 3.7, which are not shown in the figure for reasons of clarity. Van Kesteren (1996a) shows that $\phi_{s,\max}$ is 0.65 for 100% silt skeletons. In Figure 3-2b, $\phi_{s,\max}$ is set to 0.65 while $\phi_{s,\min}$ is varied, leading to $\Delta\phi_s$ values of 0.25, 0.12 and 0.0. An increase in $\phi_{s,\min}$ leads to an increase in $w_{s,eff} / w_{s,0}$ over the whole range of ϕ_s.

From the above it is concluded that the performance of equations 3.6 and 3.7 is quantitatively similar. However, it is preferred to use equation 3.6 because this equation has a stronger theoretical basis compared with the more empirical equation 3.7. To validate the newly derived HSF, a series of settling experiment is carried out with fine grained sediment mixtures using settling columns. The application of sedimentation theory which has been used to analyse these experiments is explained first in the next section.

3.3 Application of sedimentation theory

The solution of the 1D-wave equation for the sedimentation of sediment-water mixtures is discussed in section 2.3.2 and forms an important basis for further analysis. In this section the application of this solution to laboratory experiments is explained. The solution to the 1D-wave equation implies that the slope of a characteristic line within the $\phi_s(z,t)$-plot represents an effective settling velocity:

$$\frac{\mathrm{d}z}{\mathrm{d}t} = w_{s,0}F(\phi) = w_{s,eff} \qquad 3.8$$

Where $F(\phi) = \mathrm{d}[\phi f(\phi)] / \mathrm{d}\phi$, $f(\phi)$ is a HSF (e.g. 3.2), t is time and z is the vertical coordinate, positive downwards. Dankers (2006) used this theory to derive effective settling velocities from the settling curve of a cohesive-sediment water mixture. For that, a mono-dispersed mixture is assumed, which implies that $w_{s,0}$ is constant. For non-uniform PSD's, a modification of the above mentioned solution of the 1D-wave equation is required. Here, this has been done by making the particle size d implicit, resulting in a formulation for the characteristic lines within the *(z,t)*-plane:

$$\frac{\mathrm{d}z}{\mathrm{d}t} = w_{s,0}(d)F(\phi) = w_{s,eff}(d) \qquad 3.9$$

A consequence of using d in equation 3.9 is that effective settling velocities can no longer be normalized with a single clear water settling velocity ($w_{s,0}$). Hence, the complete PSD needs to be taken into account. To clarify the settling behaviour of multiple granular fractions, Figure 3-3 illustrates the settling behaviour of an initially homogeneously concentrated sediment-water mixture with two granular size fractions. Fractions 1 and 2 are assumed to have initial solid content $\phi_{s,0,1}$ and $\phi_{s,0,2}$ respectively, with $d_1 < d_2$ and $w_{s,eff,1} : w_{s,eff,2} = 1:2$. At the upper interface (highest level z where particles of that fraction are present) of each fraction, all particles of that fraction settle with a single velocity $\left[w_{s,eff} = w_{s,0}f(\phi)\right]$. This results in the segregation of the mixture in the upper part of the column, since $w_{s,0,2} > w_{s,0,1}$ and the sum of the solid fraction at t_0 (ϕ_0) is uniform. The interface of fraction 1 will always lower in the remainder of the suspension with solid content equal to $\phi_{s,1}$, whereas the interface of fraction

2 settles in the full suspension where $\phi_s = \phi_{s,1} + \phi_{s,2}$. The evolution of the two interfaces in the (ϕ_s, z)-plane is schematized in Figure 3-3. In addition, the figure shows the characteristic lines in the *(z,t)*-plane, corresponding with the interface lowering in time. These characteristics present solid content isolines (isolutes). The above implies that effective settling velocities for both fractions can be derived from the slope of the isolutes.

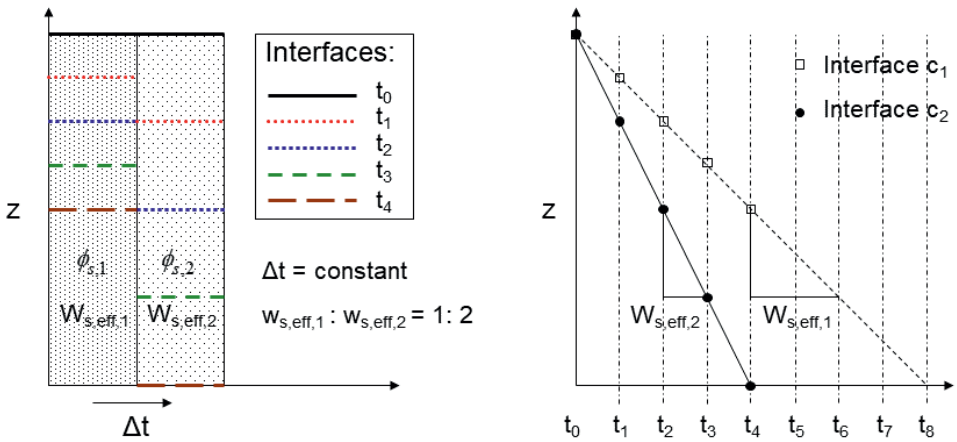

Figure 3-3 Illustration of the settling behaviour of a sediment-water mixture with two granular fractions.

The principle illustrated in Figure 3-3 holds in general for initially homogeneously graded sediment-water mixtures and it assumes that segregation is a continuous process. Since the interface of the fraction with the largest particles lowers first, the interface of the fraction with the second largest fraction lowers in the remaining sediment-water mixture, of which the solid content equals the total solid content minus the solid content of the coarsest fraction. This process repeats itself for each finer fraction until only the lowering interface of the fraction of the smallest particles remains. While the finest fraction settles, an upper interface I_U is visible owing to the colour contrast between the sediment-water mixture and the water column above it. The behaviour of such multiple size fractions is illustrated in Figure 3-4, yielding a fan of descending isolutes, of which the point of origin is found in the water level at t_0. A lower interface I_L develops following the formation of the bed. Latter process is not discussed in this chapter.

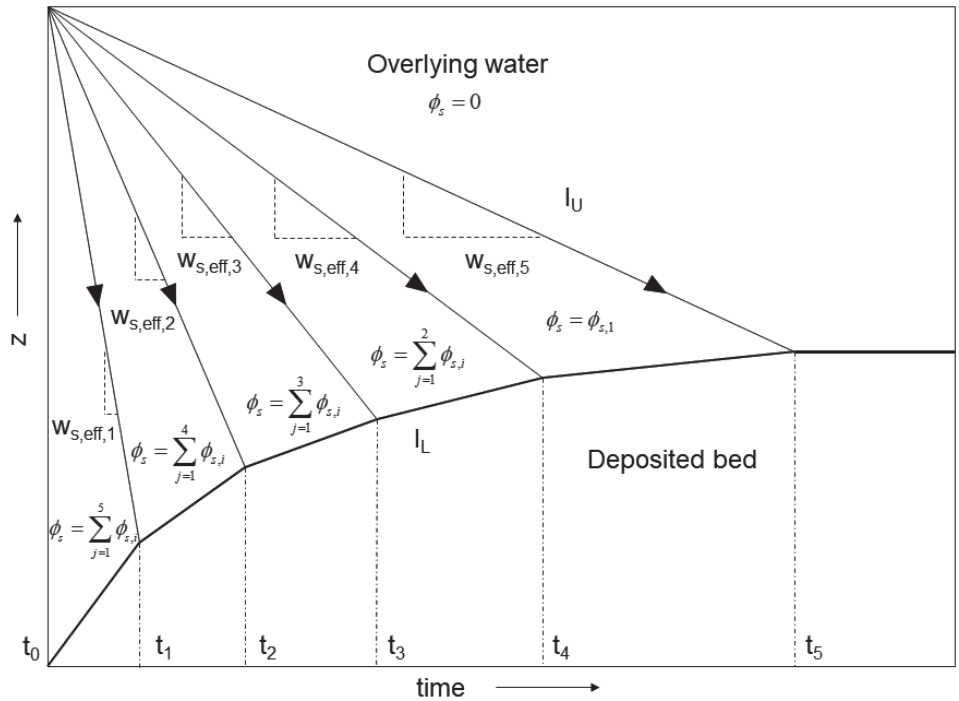

Figure 3-4 Settling behaviour of graded granular sediment with 5 sediment fractions and uniform initial solid content distribution. Arrows represent characteristics lines, I_u and I_l are the upper and lower interface respectively.

Despite the non-uniformity of $w_{s,0}$ in graded sediment-water mixtures, the bulk settling behaviour can now be assessed by evaluating the complete fan of isolutes. Before applying such an evaluation to laboratory experiments, an analytical test is given which demonstrates how to analyse a fan of isolutes.

Consider the settling behaviour of silt #1 (sediment mixture used in the settling experiments in section 3.4 with PSD shown in Figure 3-8) at various initial homogeneously distributed solid contents (e.g. $\phi_{s,0}$ = 0.04, 0.18, 0.29 and 0.43). The RZ-equation (equation 3.2) is used to compute effective settling velocities for i size bins within the PSD. For that, the PSD is discretised. The effective settling velocity of each internal interface (a total of i interfaces) is computed based on the local solid content and corresponding particle diameter by:

$$w_{s,eff,i} = w_{s,0}(d_i)\left(1 - \sum_{j=1}^{i} \phi_{s,i} / \phi_{s,\min}\right)^n \qquad 3.10$$

Where $w_{s,0}$ is computed for each size bin i via equation 3.1 and $\phi_{s,\min}$ is arbitrarily set at 0.53. The effective settling velocity for each size bin $(w_{s,i})$ can be computed from the initial solid content. The effective settling velocities computed for the corresponding size bins and initial

solid content are shown by connected points of equal colour in Figure 3-5. The coloured lines formed by connected points present the effective settling velocities that occur in the experiments in time, at which the largest settling occurs first. Each line corresponds with an initial solid content and each point corresponds with a particle size representing the size bin, and represent the slope of an isolute. The isolutes of all settling fractions form a fan in the *(z,t)*-plane. Every initial solid content gives an unique fan. All possible combinations of effective settling velocities and solid content are enclosed by an envelope (black continuous and dotted curve in Figure 3-5).

The upper and lower boundary of this envelope present all possible effective settling velocities of the largest and smallest particles within the PSD which can be used to analyse a fan obtained from measurements. In Figure 3-5, logically, all possible effective settling velocities for silt #1 fall within the boundaries enclosed by this envelope since the settling velocities are generated with the same HSF used to evaluate the output.

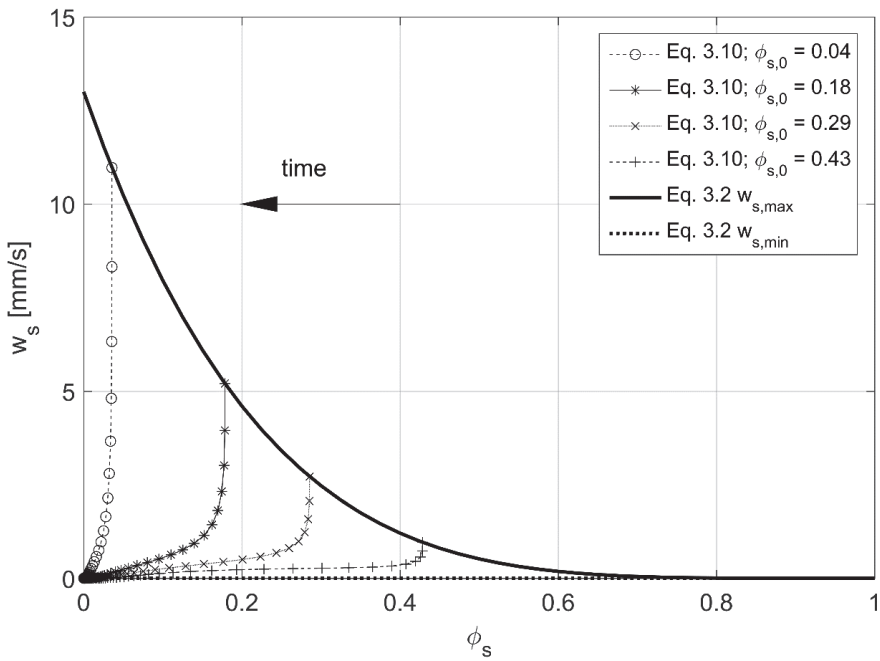

Figure 3-5 Results of computed (equation 3.2 and 3.10) settling velocities for demonstration of the derivation of settling velocities isolutes (equation 3.9). Coloured lines present the settling velocities computed for one initial solid content in time with PSD of silt #1. The black solid and black dotted curves (following x-axis) form an envelope enclosing all possible effective settling velocities (following equation 3.2 and using n = 4.4) for the maximum and minimum particle size in silt #1, respectively. The black lines form the upper and lower bound values for all possible combinations of settling velocities and solid fractions.

The previous discussion on the application of sedimentation theory to settling experiments with graded-sediment water mixtures provides the following insights:

- Isolutes can be constructed from solid content timeseries measured at constant levels within a settling sediment-water mixture. The effective settling velocities can be calculated using equation 3.9 if the initial solid content $(\phi_{s,0})$ is uniform;
- A quantitative comparison between various HSF's can be made by constructing an envelope enclosing the area of measured $w_{s,eff}(\phi)$.

3.4 Experiments

3.4.1 Experimental set up

To test the derived HSF for the settling behaviour of fine grained sediment-water mixtures, deposition experiments are carried out in cylindrical settling columns (Figure 3-6), in which homogeneously distributed graded sediment-water mixtures are allowed to settle at varying initial solid contents. First, an experiment was performed at a low solid content. Next, more sediment of the same sediment mixture was added to the column after which the experiment was repeated at larger solid contents. Prior to each experiment the column was stirred up thoroughly with a stirrer for some minutes to obtain a homogeneous solid content. The columns are equipped with conductivity sensors to measure solid content with time; these sensors are placed at regular intervals along the column wall and are connected to a conductivity concentration meter (CCM). The measurement frequency of the CCM is 1 Hz. To reduce the influence of the sensors on the settling sediment-water mixture, the sensors are installed flush following the curvature of the wall. Since conductivity measurements are sensitive to temperature fluctuations, the columns are equipped with a temperature probe as well. A scale bar attached to the column wall enables the measurement of the development of the interface between the clear water and the sediment-water mixture. Ten pore water pressure ports are mounted in the column walls at 5.0 cm spacing, starting at 5.0 cm from the impermeable base plate. In addition, one port is located at a level of 1.0 m above the base plate, which is used for reference pressure measurements, since it is always located above the sediment bed. Each port entry was provided with a porous plastic filter to prevent sediment leaks. The ports were connected via small tubes to a pressure-measuring unit. This method has been previously used by Bowden (1988) and later by Merckelbach (2000). The pressure-measuring unit houses one pressure transducer. This pressure transducer can be connected to any of the pressure ports, one at a time. The transducer is adjustable to a variable water head level for calibration purposes. The accuracy of the pore water pressure values from calibration is 1 mm water head, or 10 Pa.

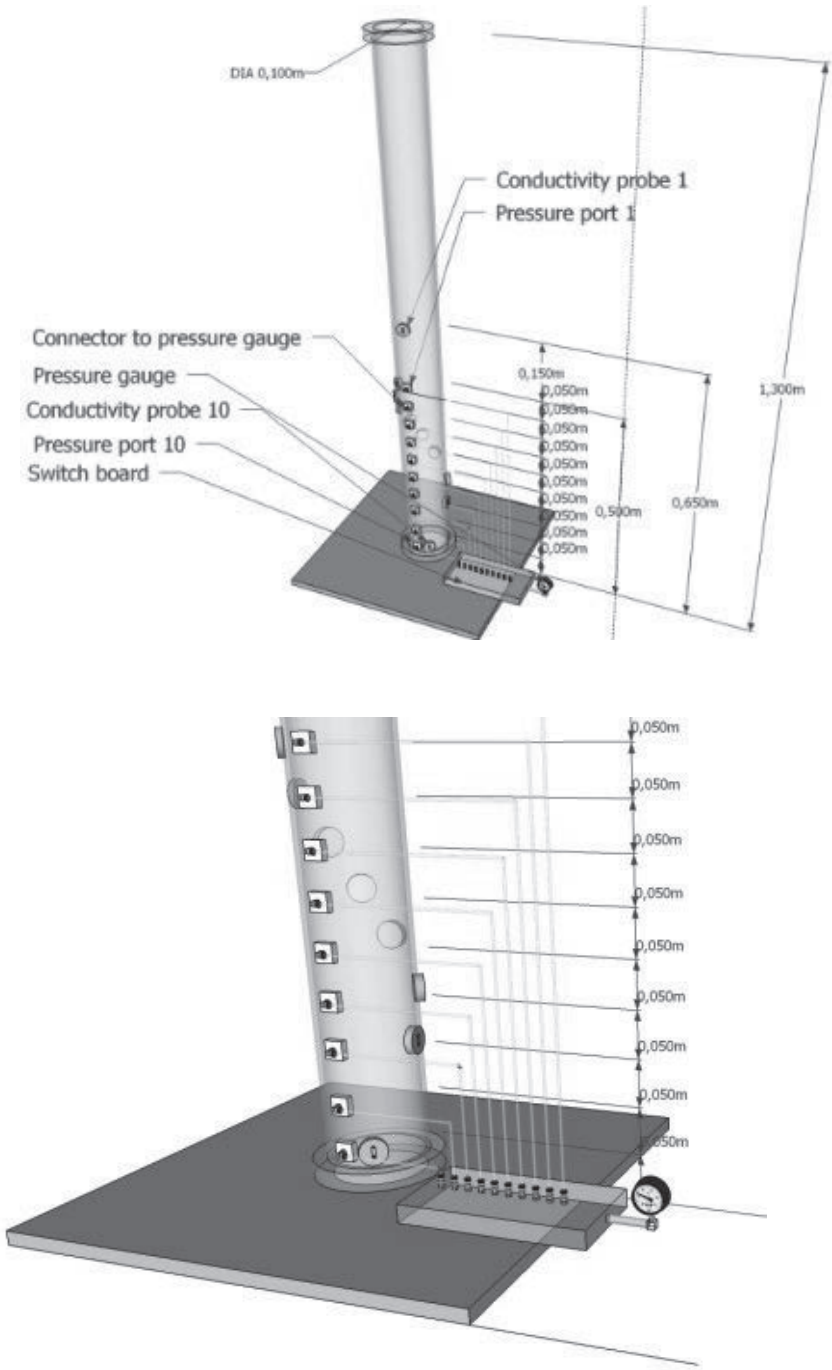

Figure 3-6 Settling column with locations of conductivity probes and pressure ports (upper sketch) with close up of excess pore water measuring points (lower sketch).

The solid content is measured using electrical conductivity. This is done with a Conductivity Concentration Meter (CCM) developed by Deltares. The principle of a CCM measurement is based on the conductivity gradient of a sediment-water mixture as a result of the gradient in non-conductive sediments in the monitored area. The CCM houses 20 ports, which can measure simultaneously. Each port is connected to a double platinum electrode probe, mounted in the wall of the column, flush with its curvature to minimize the influence of the probes on the deposition process. Each pair of probes is placed with a vertical distance of approximately 1 cm. All columns house 10 conductivity probes at 5, 15, 20, 25, 30, 35, 40, 45, 50 and 65 cm from the base plate. The top probe was placed at a higher level with the aim to function as a reference measurement in the overlying clear water in later stages of the experiments. Since conductivity measurements are sensitive to temperature fluctuations, the columns are placed in an air-conditioned environment, but nonetheless not free from temperature fluctuations. In order to correct for temperature fluctuations, the temperature inside the columns is measured at the tip of a 50 cm long temperature probe. The sensitivity of the temperature probes has a resolution of ± 0.1 °C. Temperature and solid content measurements inside a single column are always carried out simultaneously.

3.4.2 Conductivity Probes

Theory of conductivity measurements

The electrical conductivity of a medium is sensitive to temperature, salinity, pH and solid content fluctuations. Here, pH and salinity are constant in all experimental series and hence the measured conductivity is a function of temperature and solid content only. Fresh water is used in all experiments. The electrical conductivity of water as function of temperature is generally non-linear. However, the degree of nonlinearity is relatively small in a temperature range of environmental monitoring (0 - 30 °C) and a linear equation is commonly used to represent this relation (Sorensen and Glass, 1987). The temperature is generally kept between 20 °C and 25 °C. Therefore, the conductivity of water (K_w) and the sediment-water mixture (K_m) can be described by:

$$\begin{aligned} K_w &= K_{w,ref}(1+\kappa\Delta T) \\ K_m &= K_{m,ref}(1+\lambda\Delta T) \end{aligned} \qquad 3.11$$

where $K_{w,ref}$ and $K_{m,ref}$ are reference conductivities, ΔT the difference with a reference temperature and κ and λ coefficients describing the influence of temperature on conductivity. A linear relation between solid content and electrical conductivity was found by Dai et al. (2009), which can be written as:

$$\phi_s = \left(1 - \frac{K_m}{K_w}\right) a \qquad 3.12$$

where a is a calibration parameter. Equation 3.12 describes the solid content as a function of temperature and electrical conductivity.

Calibration and accuracy

In each column, a series of sedimentation experiments is carried out with one sediment mixture. These mixtures are obtained from grinding pure quartz. The sediment used for the calibration of the probes is similar to the sediment used in the experiments. The following function is used to express the measured conductivities in terms of ϕ_s:

$$V = \alpha T + \beta\phi_s + \gamma T\phi_s + \varepsilon \quad \rightarrow \quad \phi_s = \frac{V - \alpha T - \varepsilon}{\beta + \gamma T} \tag{3.13}$$

where V is the output voltage of a conductivity measurement, T the temperature, ϕ_s the solid content and α, β, γ, and ε are coefficients. Thus, the linear influence of temperature, the linear influence of the solid content and one cross term for the influence of temperature and solid fraction are taken into account. The coefficients α, β, γ, and ε are determined by calibration against experimental data for solid content and temperature.

In a specially designed calibration beaker samples of known solid content are prepared, and the output voltage of the CCM is measured for different temperatures, obtained by slightly heating the sample. The measurement error of each sensor system (temperature, electrode distance and wiring) is defined as the root mean square error (RMSE, σ_ε^2) of the measured solid content (M) and the observed solid content (O) for each temperature - solid content combination i. In addition, the RMSE is determined for each individual solid content, for which a characteristic (for all columns) result (for silt #1) is shown in Figure 3-7. The RMSE (σ_ε^2) is defined as:

$$\sigma_\varepsilon^2 = \sqrt{\frac{\sum (M_i - O_i)^2}{n}} \tag{3.14}$$

Since the RMSE varies only little over the range of predetermined ϕ_s, the accuracy of each probe is defined as the overall (for all solid contents) RMSE of the calibration. For all probes in each column, the overall accuracy in ϕ_s is found to be below 0.011, corresponding with a mean error in concentration smaller than ± 29.15 kg/m^3 $\left(c = \phi_s \rho_s\right)$.

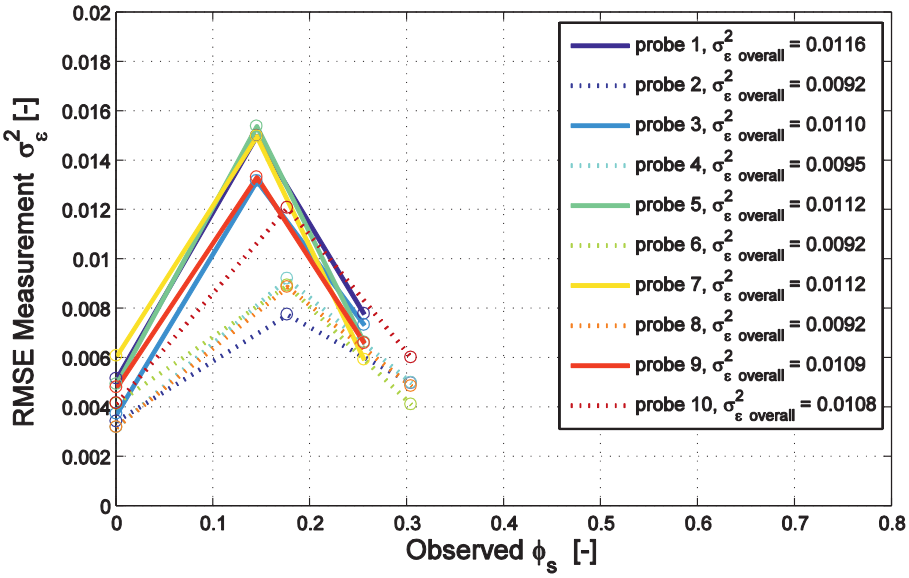

Figure 3-7 Calibration errors for all probes in column of silt 1. Overall RMSE's for each probe are depicted in the legend.

Sediment

Three fine-grained sediment mixtures are used which consist for more than 99% of quartz particles and have median particle sizes (d_{50}) of 29, 36 and 75 µm (Table 3-1). These sediment mixtures are referred to as silt #1, silt #2 and silt#3, respectively. The PSD's are measured by laser diffraction with a Malvern particle sizer (results in Figure 3-8). The materials used for the tests are all wide graded ($4 < d_{90} / d_{10} < 10$).

Table 3-1 Properties of PSD's of used sediment mixtures.

ID no.	d_{10} [µm]	d_{50} [µm]	d_{90} [µm]	d_{90}/d_{10} [-]
Silt #1	6	29	59	9.8
Silt #2	13	36	75	5.8
Silt #3	35	75	158	4.5

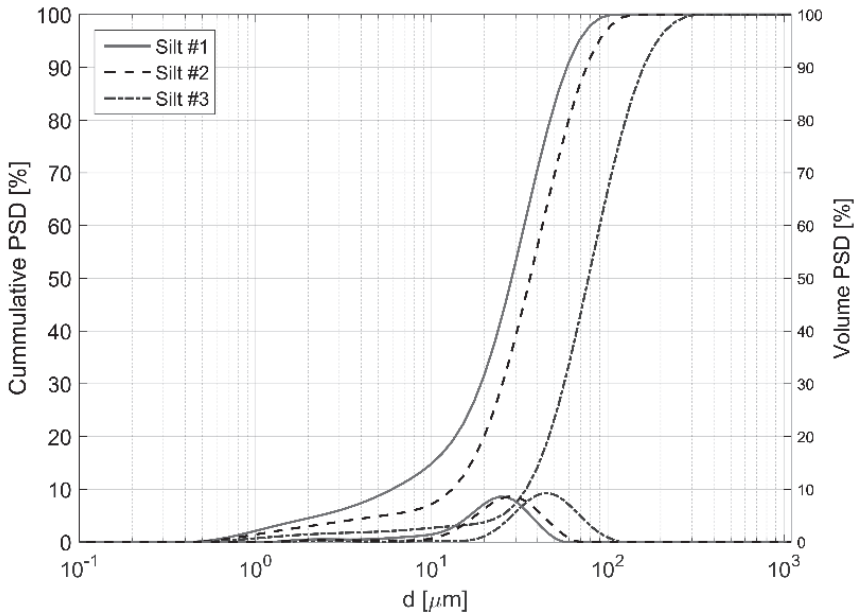

Figure 3-8 Volume and cumulative volume particle size distributions of sediment mixtures as used in the sedimentation experiments.

Experimental series

A different settling column is used for each sediment mixture. In each column, a series of settling experiment is carried out through a stepwise increase of the initial solid content. At the start of each experiment, the sediment-water mixture in the columns was homogeneously mixed, after which it was allowed to settle. In every experiment, the solid content was measured at all vertical measuring positions in the columns. In total 33 experiments were carried out. When visually observed, the upper interface of the settling sediment-water mixture was measured and recorded as well. The solid content time series allows for the computation of effective settling velocities by using sedimentation theory, as described in the previous section. Application of sedimentation theory to the results of the experiments are discussed in the next section.

3.5 Results and analysis

Clear water settling velocities and minimum solid content

Prior to the quantitative analyses of the hindered settling behaviour of sediment-water mixtures, the clear water settling velocities and the solid content at the loosest packing of the bed are determined. Characteristic particle sizes are used to compute ($w_{s,0}$) by using Stokes's (1851) equation (Table 3-2). These velocities are later applied to determine hindered settling effects.

Table 3-2 Clear water settling velocities (Stokes) for characteristic diameters of used silt mixtures.

ID no.	w_s corresponding to d_{10} [mm/s]	w_s corresponding to d_{50} [mm/s]	w_s corresponding to d_{90} [mm/s]
Silt #1	0.03	0.76	3.12
Silt #2	0.15	1.17	5.05
Silt #3	1.10	5.07	22.4

In total 33 settling experiments are carried out during which solid content timeseries are measured. The initial solid contents for each experimental series is shown in the legend of the top panels of Figures 3.12 to 3.14. These timeseries are used to asses settling behaviour in general and to analyse the characteristic lines.

Solid content measurements at low ϕ_0 (tests 5) and high ϕ_0 (test 12) with silt #1 (Figure 3-10) are discussed first. After t_0, particles settle and deposit on the base plate, resulting in a solid content increase in the lower part of the column, and a solid content decrease (down to $c = 0$) in the upper part of the column. While the bed builds up from the base plate, the minimum solid content ($\phi_{s,\min}$) is measured. The measured minimum solid content of each silt mixture is shown in Figure 3-9 and the minimum measured value of $\phi_{s,\min}$ is used for further analyses.

Figure 3-9 shows a decrease in minimum solid content with increasing d_{50}, which is unexpected since $\phi_{s,\min}$ is assumed to decrease with increasing silt content (Van Kesteren, 1996a). Increasing d_{50} implies increasing (fine) sand content and thus decreasing silt content. The differences are small ($\Delta\phi_s \approx 0.015$), but exceed the accuracy of the solid content measurements. When considering the gradation, the sediment mixture with the widest gradation (silt #1) has the highest $\phi_{s,\min}$ (0.485), while the d_{50} is lowest (29 µm). The sediment mixture with the narrowest gradation (silt #3) has the lowest $\phi_{s,\min}$ (0.463), while the d_{50} is largest (75 µm).

The development of a vertical gradient in the solid content profile (Figure 3-9) is considered to be the result of segregation and the overburden of deposited particle on the bed. The resulting vertical solid content gradient is more prominent at low solid contents, implying that at higher solid contents segregation reduces, which is a hindered settling effect. The occurrence of hindered settling is further supported by visual observations of a sharper upper interface between the clear water and the settling sediment-water mixture (I_U in Figure 3-4) at higher solid contents. The interface between the overlying clear water and the settling solids is of different origin than as observed by Diplas and Papanicolaou (1997) and Dankers and Winterwerp (2007). The zones of equal solid content as observed in these studies are the results of hindered settling; the settling particles have lost their individual settling properties. Therefore, the observed segregation in the present experiments is considered characteristic for the hindered settling of fine grained sediment-water mixtures.

Construction of isolutes

Isolutes are constructed in the (z,t)-planes for all 33 experiments. Rising and descending isolutes are visualized by coloured contour plots (Figure 3-11), which are obtained by vertical interpolation of the solid content measurements with time and space. The rising isolutes represent the accreting bed and the descending isolutes represent the settling particles.

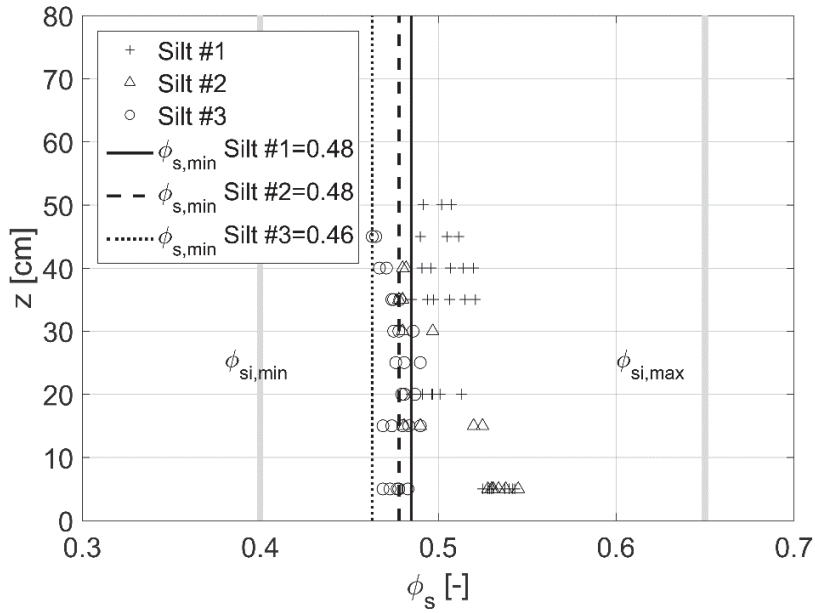

Figure 3-9 Measured solid content upon deposition at various levels in all experiments. Vertical solid grey lines indicate minimum and maximum solid content for a 100% silt skeleton (Winterwerp and Van Kesteren, 2004).

The steps in the rising isolutes are the result of vertical interpolation of the solid content measurement. Therefore, in the area just above the deposited bed, the reliability of the solid content in the contour plots is less accurate. After deposition, the isolutes in the bed are horizontal.

In addition to the coloured contour plot of the solid content, measurements of predefined solid fraction (from $\phi_s = \phi_{s,0}$ to $\phi_s = 0$ in steps of 0.01) at various elevations are highlighted with red squares (Figure 3-11a and b). Through the points of equal solid content, an isolute is constructed by applying a least-square fit. These isolutes are fixed at the water level at t_0. At this point, the solid content decreases from $\phi_{s,0}$ to 0 with time. Therefore, this point is singular and forms the origin of all isolutes. Hence, a fan of isolutes, with its origin at the water level, defines the settling velocities of the internal interfaces. At low initial solid contents (Figure 3-11a), the isolutes diverge stronger than for the high initial solid contents (Figure 3-11b), which is the result of hindered settling. Figure 3-11 shows that the characteristic lines, extrapolated to the initial conditions at the water level, follow the measured line of equal solid content (isolutes) in the water column, which justifies the application of sedimentation theory.

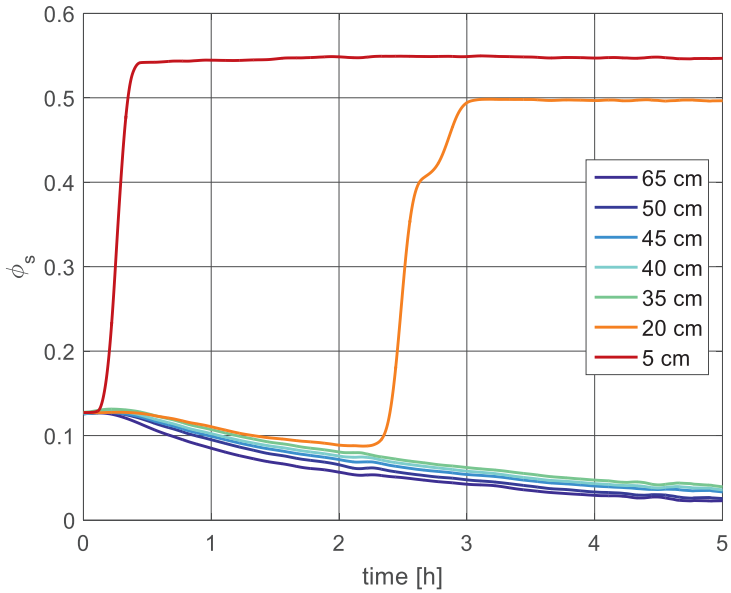

(a)

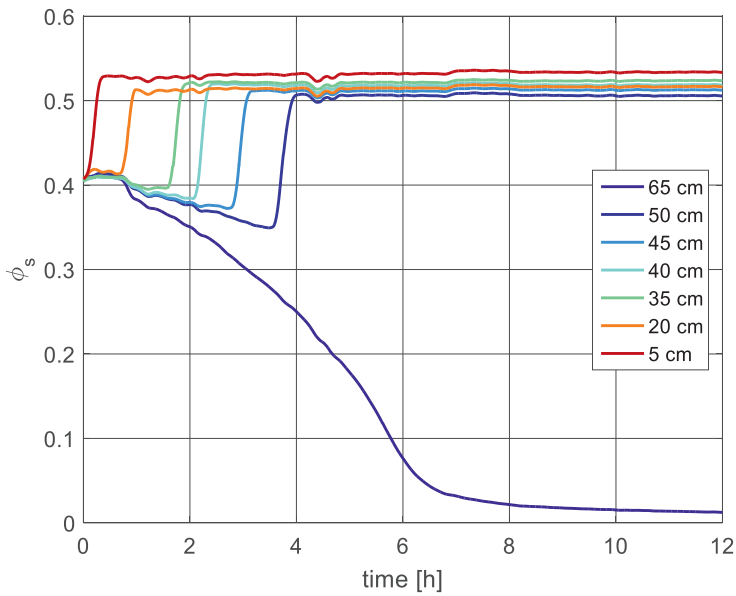

(b)

Figure 3-10 Measured solid content (ϕ_s) time series for test 5 (top, $\phi_0 = 0.127$) and test 12 (bottom, $\phi_0 = 0.409$) for silt #1. Recording levels of solid content time series are indicated in the legend.

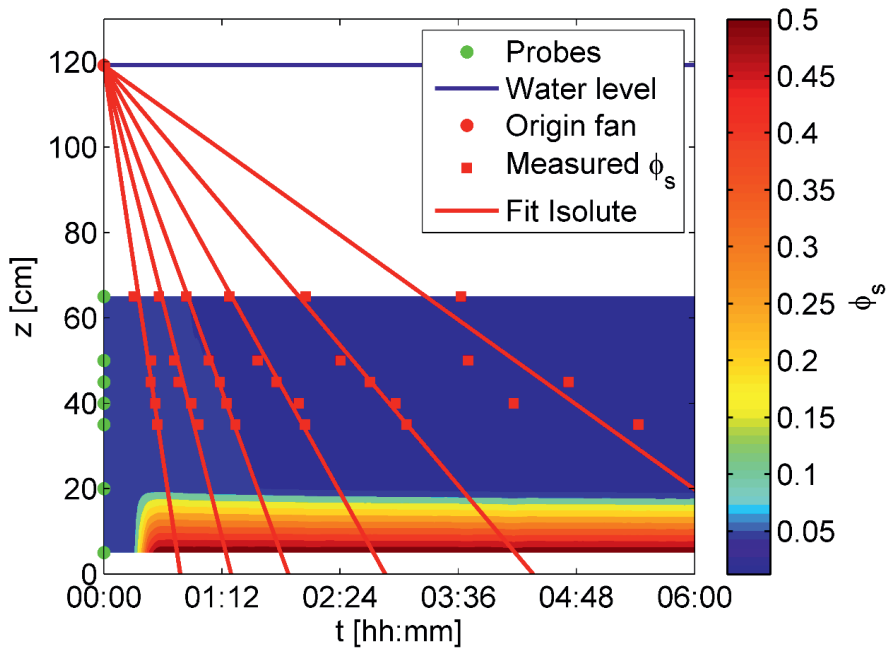

(a)

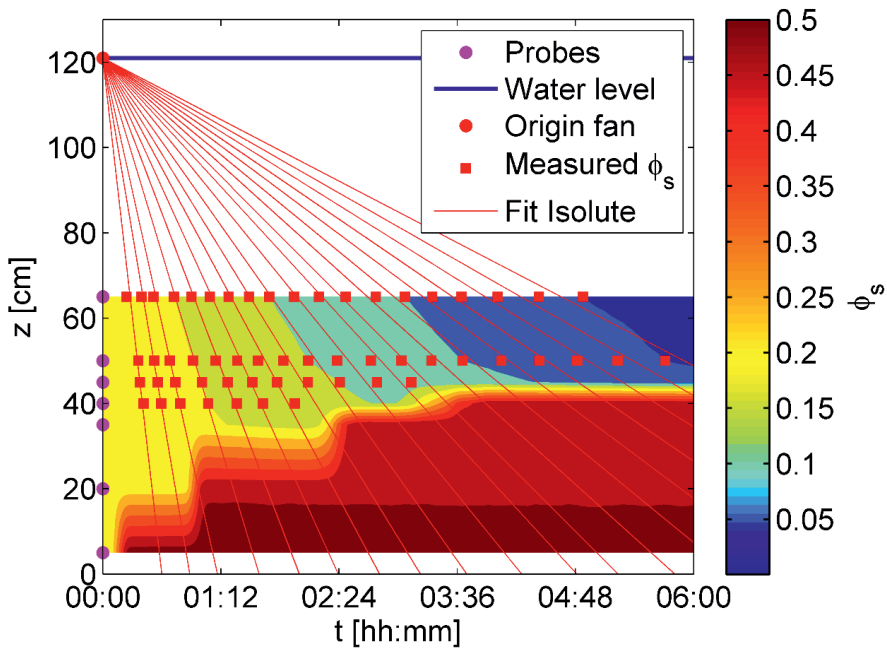

(b)

Figure 3-11 Results of settling tests 3 (top) for $\phi_{s,0}$ = 0.076 and test 8 (bottom) for $\phi_{s,0}$ = 0.219 for silt #1. In both figures $\Delta\phi_s$ = 0.01 for all subsequent isolutes. The slope of the computed isolutes in the hindered settling regime represents an effective settling velocity.

Accuracy of solid content measurements

The applicability of the method developed in section 3.3 to analyse effective settling velocities depends on the initial solid content and the measurement accuracy. At low initial solid content, the solid content of the size bin (within the discretised PSD) of the largest particles is below the measurement accuracy. As a consequence, isolutes corresponding to the settling velocities of the largest particles cannot be constructed. The accuracy of the solid content sensors is $\Delta\phi_s$ = 0.011, corresponding with a concentration of 29 kg/m^3. Hence, the solid content of a size bin should exceed 0.011 for the effective settling velocity to be derivable. At low initial solid content, the effective settling velocities of the largest particles cannot be derived. The solid content of the bin with the largest grain size increases with increasing initial solid content and becomes measurable above a certain initial solid content. The upper boundary of the $w_{s,eff}$–envelope in the bottom panels of Figures 3-12 to 3-14 has been corrected to the measurement accuracy and represent the effective settling velocity of the largest particle size for which the measurements are accurate (ϕ_s >0.011). The above explains why the envelopes initially show an increase in $w_{s,eff}$. When the solid content of the bin of largest particles exceeds 0.011, the $w_{s,eff}$–envelope follows the uncorrected HSF and decreases with increasing solid content. The same reasoning for the accuracy holds for the lower envelope boundary (black dotted line coinciding with the x-axis in Figure 3-5). Here, the variation in $w_{s,eff}$ is much smaller due to the influence of hindered settling effects at large solid contents. Therefore, the best quantitative comparison can be performed by assessing the upper boundary of the HSF-envelope only, for which the initial solid content is required to be known. The accuracy of the method can be improved by: *i*) narrowing the particle size distribution and *ii*) increase the accuracy of the solid content measurement.

Analysis of Hindered Settling Formulations

A common method (Tomkins et al., 2005, Cuthbertson et al., 2008) to analyse settling velocities is by normalization with the clear water settling velocity ($w_s / w_{s,0}$). For the experiments performed in this research, the measured settling velocities are a function of the solid content and the PSD. Therefore, normalization with a clear water settling velocity is not possible. Instead, the sedimentation theory as described in section 3.3 has been applied. A series of fans is derived from tests with varying $\phi_{s,0}$. The top panels in Figures 3-12 to 3-14 combine the results of these series for all three sediment mixtures. Each point in aforementioned graphs present a line in the fan. Unfortunately, the settling velocities at low solid contents cannot be determined due to the measurement accuracy of the conductivity probes (c< 30 kg/m^3). Nonetheless, the results have been evaluated with the HSF derived for fine grained sediment (equation 3.6) and with equation 3.2 by constructing envelopes (bottom panels in Figure 3-12, Figure 3-13 and Figure 3-14). Here, evaluation is done for HSF's 3.2 and 3.6, thereby varying m in the latter, and using $\phi_{s,\min}$ from measurements (Figure 3-9). Only the upper boundary of the envelope is used, since the measurements of the smallest velocities are too sensitive for the solid content sensors. For some data points the computed settling velocities exceeded the values determined with the RZ-formulation using n = 4.4, especially at the larger solid contents. Larger n-values would lead to a further deviation from measurements.

All data points fall within the envelope using equation 3.6 with a return flow exponent $m = 1$. Using $m = 2$ yields more data points outside the envelope.

Standard methods to evaluate the settling velocities are by means of a sedimentation balance or by optical techniques (Eisma et al., 1996). The present study demonstrates that the settling behaviour of fine graded sediment can also be evaluated by using sedimentation theory. Since all isolutes are represented by straight lines, a single solid content timeseries is sufficient to construct the fan of isolutes from which all effective settling velocities are derived. The measurement should preferably be performed just above the level of the bed to measure the range of solid fractions between $\phi_{s,0}$ and 0.

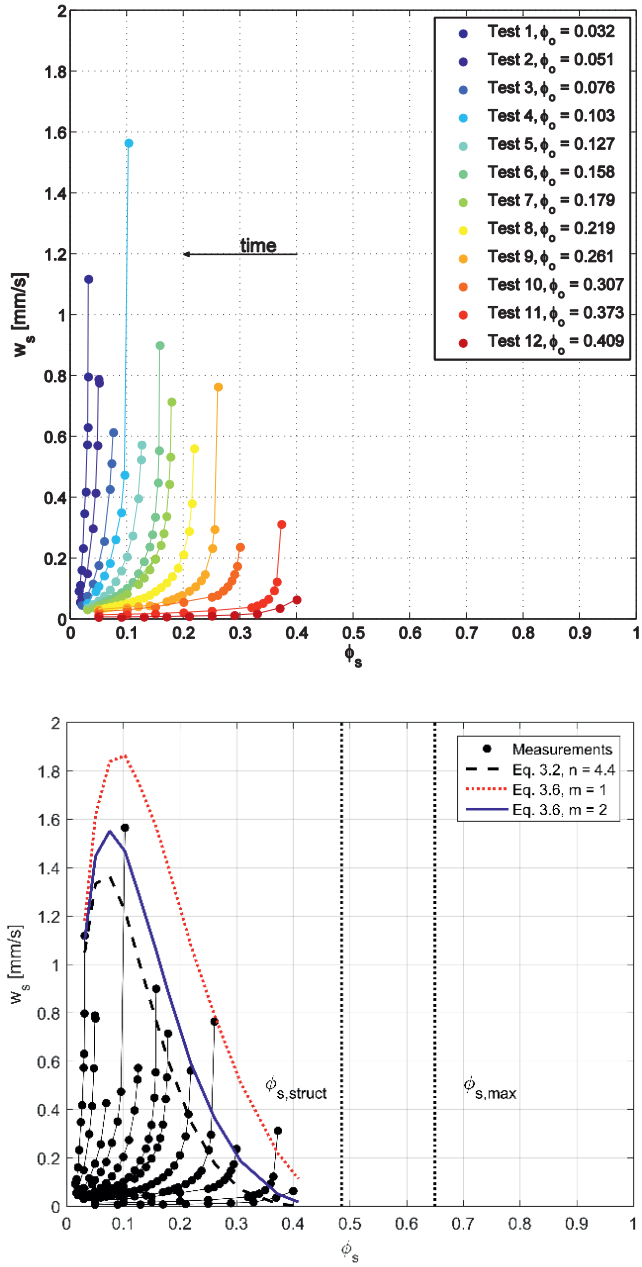

Figure 3-12 Derived effective settling velocities for silt #1, d_{50} = 29 µm (top). Connected points present settling velocities measured within a single experiment. The bottom figure presents the upper limit of the envelope enclosing all computed settling velocities for various HSF's.

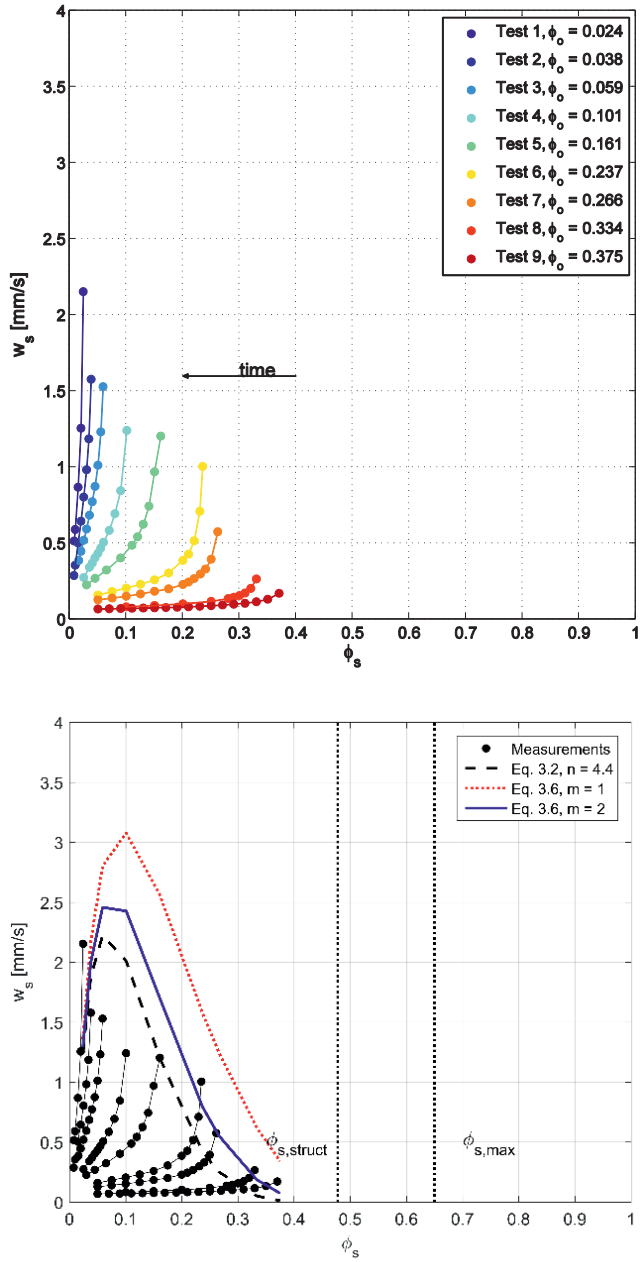

Figure 3-13 Derived effective settling velocities for silt #2, d_{50} = 36 µm (top). Connected points present settling velocities measured within a single experiment. The bottom figure presents the upper limit of the envelope enclosing all computed settling velocities for various HSF's.

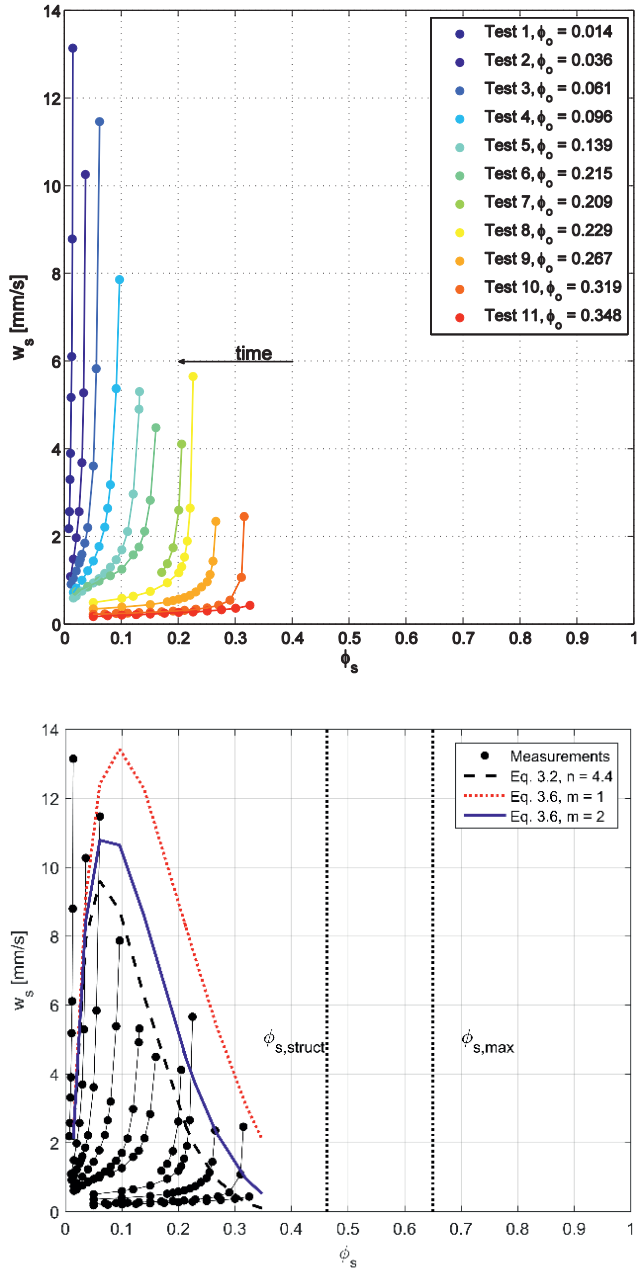

Figure 3-14 Derived effective settling velocities for silt #3, d_{50} = 75 µm (top). Connected points present settling velocities measured within a single experiment. The bottom figure presents the upper limit of the envelope enclosing all computed settling velocities for various HSF's.

3.6 Discussion and conclusions

Performance of the new hindered settling formulation for silt

The derived HSF for silt is tested against experimental data obtained from laboratory experiments. Important parameters are the minimum solid content $\phi_{s,\min}$, the maximum solid content $\phi_{s,\max}$, PSD and the exponent of non-linearity in the return flow m. The first two parameters can be obtained from standard geotechnical porosity measurements ASTM-D4253 (2006), whereas the latter can be obtained from measurements or theoretical analysis. A practical estimation of the minimum solid content is based on particle size distribution and is given by Wu and Wang (2006). From the present experiments no consensus on the non-linearity of the return flow could be determined, but it is likely to be found in the range between $m = 1$ and $m = 2$. The allocation of the appropriate scaling parameters to the corresponding physical processes should be considered carefully.

Wan and Wang (1994) analysed settling velocities of silt sized material by using the maximum solid content ($\phi_s = 1$) instead of the minimum solid content in equation 3.2. As a result, n-values as high as 7 are obtained. Interestingly, the results of equation 3.2 with $n = 7$ and $\phi_{s,\min}$ agree well with equation 3.6, when using $m = 1$ up to $\phi_s \approx 0.25$ (Figure 3-15). Chien and Wan (1999) concluded that equation 3.2 fits best with the data of Qian (1980a) when using $n = 4.91$. However, the application of such high n-values lacks a physical background, since settling velocities become nonzero at volume solid contents beyond the minimum solid content. The example above illustrates the importance of applying the appropriate scaling parameters.

Figure 3-15 shows that equation 3.6 compares favourably with the data of Qian (1980a), even at the largest solid contents. These results are obtained with $\phi_{s,\min}$ and $\phi_{s,\max}$, which are realistic parameters for silt. Hence, it is concluded that equation 3.6 is more robust for fine grained sediment, which is in fair agreement with results obtained from laboratory experiments.

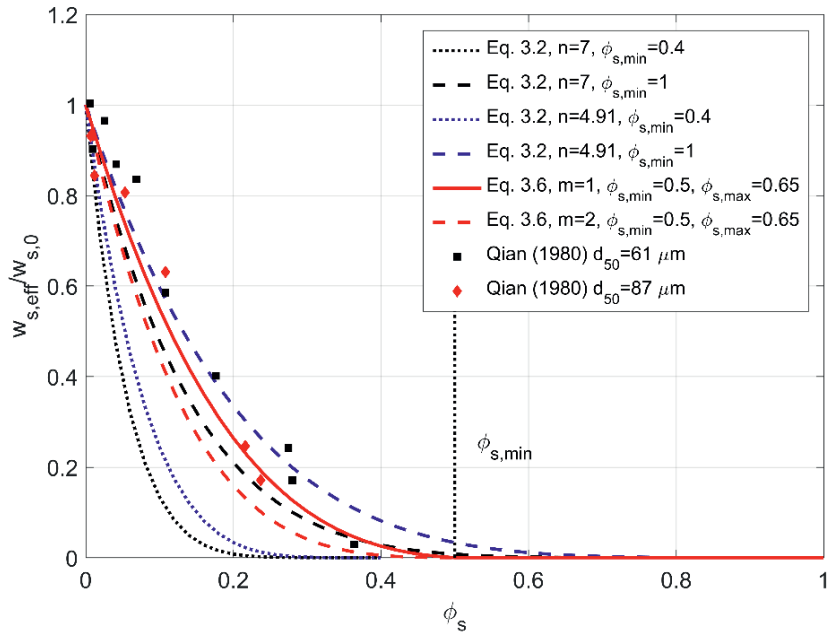

Figure 3-15 Comparison of Richardson-Zaki HSF and derived HSF for silt with data from Qian (1980) using different values for $\phi_{s,min}$, $\phi_{s,max}$, *m* and *n*.

Comparison with Real World Silt

Zhang et al. (2008) have performed measurements on particle size fractions of selected samples from the Yellow and Yangtze River. They concluded that there are large variations in sediment composition in the Yellow and Yangtze River estuarine sediments, with silt being dominant in most cases. However, on average, Yangtze River sediments consist of 66% silt (4-63 µm), 20% clay (<4 µm) and 14% sand (>63 µm). The Yellow River sediments consist of 62% silt, 16% clay and 22% sand. Most of the particle sizes fall in the size range of medium silt (16-32 µm) to coarser silt (32-63 µm). Mineralogy analyses of clay minerals show that illite is the dominant clay mineral in both Yellow and Yangtze Rivers. Kaolinite contents are slightly higher in the Yangtze River and chlorite contents are about equal. Results are shown in Table 3-3. Xu et al. (2009b) also performed a mineralogical analysis on the silt fraction in the Yangtze River. It was concluded that the silt fraction consists of quartz and feldspar. These observations emphasize the importance of understanding the behaviour of silt, as it is present in large quantities in both river systems. In Figure 3-16, electron microscope photos of the grinded pure quartz (as used in present experiments) and sediment from the lower reaches of the Yellow River system are compared. The sediment from the Yellow River was taken from an area with a low clay fraction, hence no clay minerals can be identified on the photo. It can be seen that, despite a difference in size, the particles show a large resemblance in shape and roundness. This indicates that the fine grained sediment used in present experiments, and the HSF derived from it, are representative for real world silt.

Table 3-3 Summary of sediment compositions of bulk estuarine sediments from the Yellow and Yangtze River. n represents the number of samples. Data after Zhang et al. (2008).

	The Yellow River (n=129)			**The Yangtze River** (n= 100)		
	Minimum	Maximum	Mean ± SD	Minimum	Maximum	Mean ± SD
Clay (%)	5	41	16 ± 6	0	52	20 ± 10
Silt (%)	12	82	62 ± 15	9	83	66 ± 14
Sand (%)	0	83	22 ± 19	0	91	14 ± 18

Note: n represent the number of samples (data from (Zhang et al., 2008)

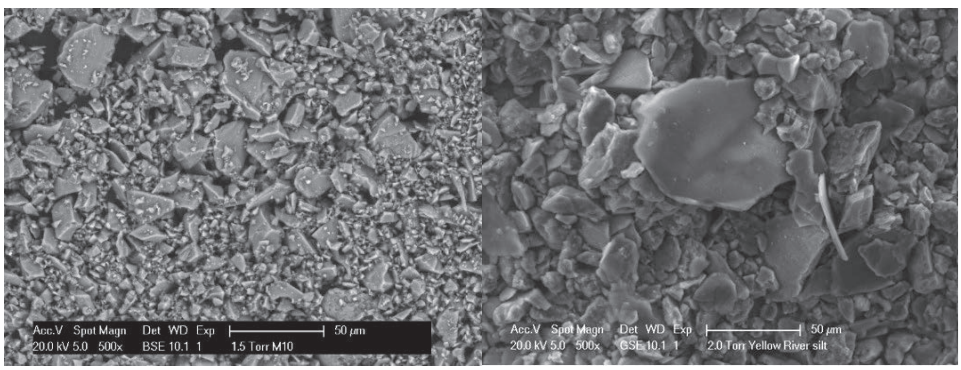

Figure 3-16 Electron microscope picture of (left) grinded quartz as used in settling experiments; (right) sediment samples found in the lower Yellow River (Weihe River).

Implications for in-situ silt suspensions

An obvious but important conclusion concerns the range of measured settling velocities. The measured effective settling velocities range between 0.01 and 3 mm/s. Under these conditions, w_s is much smaller than vertical turbulent velocity fluctuations under open channel flow conditions, and therefore, following Uittenbogaard (1994) the silt-water mixture can be treated as a single-phase fluid. The vertical turbulent velocity fluctuations are typically in the range of several centimetres per second in open channel flow (Nezu and Nakagawa, 1993). Since the effective settling velocities are so small, silt can be kept in suspension over long distances. For conditions with sufficient sediment supply, concentrations can reach up to several hundreds of kg/m^3. Such high concentrations significantly influence the hydrodynamics of silt suspensions.

A turbulent shear flow collapses when the flux Richardson number exceeds a critical value Ri_c (Turner, 1979). The flux Richardson number is essentially the ratio between the energy required to mix sediment over the water column and the available kinetic (mixing) energy provided by the flow; hence Ri_f can be regarded as an efficiency parameter for vertical mixing (Winterwerp, 2006). Winterwerp (2001) introduced a stability diagram which distinguishes sub-saturated flow (normal flow conditions) from super saturated flow (high concentration leading to a collapse of sediment concentration and the formation of fluid mud) and hyper-concentrated sub-saturated flow. These flow regimes can be distinguished based on the flux

Richardson number Ri_f and a critical value Ri_c. When $Ri_f < Ri_{cr}$ conditions are sub-saturated and when $Ri_f > Ri_{cr}$ conditions are supersaturated. At very small concentrations, buoyancy effects are not important. At larger concentration, but still in the sub-saturated regime, sediment induced buoyancy effects become important effecting vertical mixing. With further increasing concentration, capacity conditions are exceeded and the suspension gets saturated, followed by a collapse of the turbulent flow field. At much larger concentration, sub-saturated conditions are re-established, as the vertical sediment flux decreases because of hindered settling effects and hence the energy required to mix sediment over the water column reduces. This regime is referred to as the hyper-concentrated regime. Winterwerp (2001) identifies four regimes within the stability diagram:

- Super-saturated conditions; the turbulent flow is unstable and cannot carry the sediment load available;
- Sub-saturated, low concentrated; no sediment-fluid interactions and the amount of sediment carried by the flow is far below its capacity;
- Sub-saturated, high concentrated; pronounced sediment-fluid interaction and the amount of sediment carried by the flow is close to its capacity;
- Sub-saturated, hyper-concentrated; pronounced sediment fluid interaction.

Winterwerp (2001) writes the flux Richardson number as:

$$Ri_f \propto \frac{\rho_s - \rho_w}{\rho_s} \frac{g h w_{s,0} \phi_{s,\min}}{\rho u_*^3} f(\phi_s) \qquad 3.15$$

In which h is the water depth and $f(\phi_s)$ presents a HSF. The choice of HSF applied however, has important consequences for the fluxes. A stability diagram (Figure 3-17) can be used to analyse the behaviour of sediment-laden flows for varying HSF's and flow velocities. As expected, a decrease in flow velocity ($u_2 < u_1$, Figure 3-17b) results in super-saturated conditions at lower concentrations. In the sub-saturated, low concentrated regime, the different HSF's show similar behaviour; the Ri_f increases with ϕ_s and super-saturated conditions are met at only slightly smaller ϕ_s for the newly derived HSF. The concentration range over which the flow is unstable, is larger for the newly derived HSF in comparison with the RZ formulation. This implies that stable conditions require higher sediment concentrations. The higher Ri_f peak in the stability diagram of the newly derived HSF implies that super-saturated conditions occur at lower flow velocities. The wider range of ϕ_s over which super-saturated conditions occur implies a smaller range of ϕ_s over which the flow stabilizes.

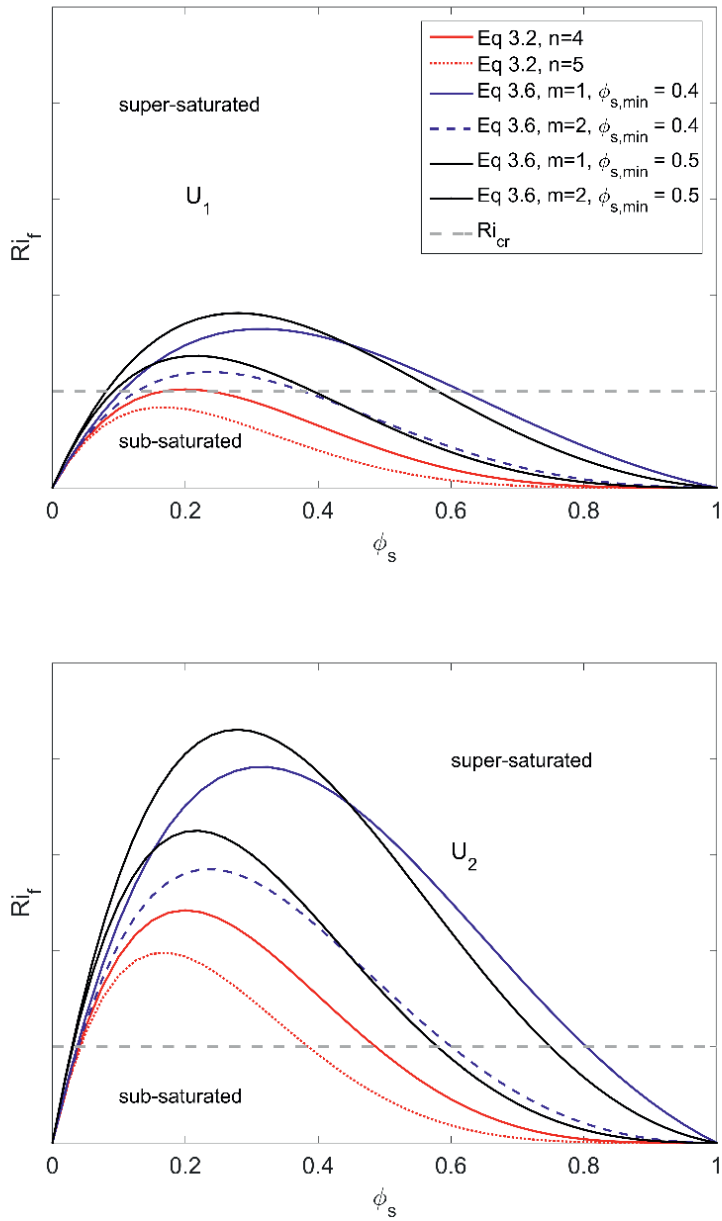

Figure 3-17 Stability diagram for sediment-laden flow, showing stability curves for different HSF's for two different (top and bottom) flow velocities $U_2 < U_1$ ($\phi_{s,max} = 0.6$).

Modelling applications

The HSF derived for silt is compared with existing HSF's for mud and sand. For that , a number of equations which have been presented earlier in this thesis are shown once more. The equation on the hindered setting of mud flocs (equation 3.22) is presented for the first time. An overview is presented on the relation between parameters in the HSF's for sand, silt and clay. The clear water settling velocities of flocs is given first by (Winterwerp and Van Kesteren, 2004):

$$w_{s,r} = \frac{\alpha}{18\beta}\frac{(\rho_s - \rho_w)\mathrm{g}}{\mu} D_p^{3-n_f} \frac{D_f^{n_f-1}}{1+0.15\,\mathrm{Re}_f^{0.687}} \qquad 3.16$$

Where α and β are shape dependant coefficients (which become unity for spheres), Re_f is the floc Reynolds number, D_p is the diameter of the primary mud flocs, D_f is the floc diameter and n_f is the fractal dimension (n_f = 3 for spheres). For spherical particles, equation 3.16 reduces to:

$$w_{s,r} = \frac{(s-1)\,\mathrm{g}D_f^2}{18\mu} \propto \frac{(\mathrm{s}-1)\,\mathrm{g}d^2}{18\mu} = w_{s,0} \qquad 3.17$$

Which is identical to the clear water settling velocity of silt and sand particles with d < 100 μm. For sand particles (100 < d < 1000 μm), which settle outside the Stokes regime, the following clear water settling velocity is applicable (Van Rijn, 1993):

$$w_{s,0} = \frac{10\mu}{d}\left[\left(1+\frac{0.01(\mathrm{s}-1)\,\mathrm{g}d^3}{\mu^2}\right)^{0.5} - 1\right] \qquad 3.18$$

The most common HSF for sand (RZ formulation 3.19, equal to equation 3.2; repeated here for clarity) combines all hindered settling effects in the n-exponent. This formula performs well at relative low concentrations, but becomes less accurate upon approaching the minimum solid content.

$$w_s = w_{s,0}(1-\phi)^n \qquad 3.19$$

The influence of particle size on the hindered settling of sand is given by equation 3.20, following Baldock et al. (2004):

$$n = 4.4(d_{50,ref} / d_{50})^{0.2} \qquad 3.20$$

Where $d_{50,ref}$ is 200 μm. The HSF's for clay 3.21 and silt 3.22 both include the effects of return flow and wake formation, buoyancy and increased viscosity (note that equation 3.20 is equal to equation 3.6, but repeated here for clarity). The major differences between these formulations are found in the scaling parameters of the hindered settling processes and the formulation for the increased viscosity, resulting in a different form of the equations.

$$w_s = w_{s,0}\frac{(1-\phi_s/\phi_{s,\min})^m(1-\phi)}{\left(1-\phi_s/\phi_{s.\max}\right)^{-2.5\phi_{s,\max}}} \qquad 3.21$$

$$w_s = w_{s,0} \frac{(1-\phi_f)^m (1-\phi)}{1+2.5\phi_f} \qquad 3.22$$

Where $\phi_f = c / c_{gel}$ is the volumetric solid content relative to the minimum solid content of the bed, in which c is the mass concentration of a mud and c_{gel} is the gelling concentration, defined as the mass concentration at which flocs form a space filling network (equivalent to the minimum solid content of granular sediment). Table 3-4 gives an overview of the different scaling parameters. Equation 3.22 relates to equation 3.21 by 1) adjusting the increased viscosity formulation for cohesive sediment flocs to spherical particles 2) adjusting the definition of the volume concentration and 3) adjusting the return flow parameter m.

Conclusions

The commonly applied Richardson and Zaki formulation for hindered settling performs well for the modelling of the hindered settling of sand. In this formulation, the n-exponent and minimum solid content $\phi_{s,\min}$ are tuning parameters that depend on particle size, particle size distribution and particle shape. Empirical studies (Baldock et al., 2004) show that the n-exponent increases with decreasing particle size up to a maximum of approximately $n = 4.4$, corresponding to a particle size of 200 μm, which is far from the silt size range, but higher n-values are not tested. The largest difference between the settling of sand and the settling of silt sized particles is the hydrodynamic regime in which these particles settle individually. The fluid movement around settling particles with $d > 100$ μm (sand) is turbulent, which causes these particles to settle outside the Stokes regime. As a result, the particle shape and size influence the settling velocity (in addition to other hindered settling effects). These geometrical effects are all incorporated in the n-exponent, which complicates the distinction between geometrical effects and other hindered settling effects. Since the fluid movement around particles with $d < 100$ μm is laminar, silt particles to settle in the Stokes regime and their geometry do not influence the settling velocity.

Physical reasoning has resulted in a HSF for silt accounting for the governing processes of *i*) return flow and wake formation, *ii*) sediment induced buoyancy effects, and *iii*) increased viscosity. This formulation is derived in analogy with Dankers and Winterwerp (2007), describing the hindered settling of cohesive sediment. A fundamental difference between their HSF and the HSF derived here is that for silt-water mixtures, particle-particle interactions generate nonlinearity in the increased viscosity. Fundamental differences with the RZ-HSF are related to scaling parameters. Since the individual processes do not all scale with the same parameters, as is suggested in the RZ formulation, the HSF for silts as presented in this chapter accounts for physical processes for which ϕ_s is scaled with $\phi_{s,\min}$ and $\phi_{s,\max}$.

The derived HSF (equation 3.6) is in good agreement with results obtained from laboratory experiments using pure quartz and silt from the Yellow River. In the hindered settling formulation for silt, no physical processes characteristic for cohesive sediment are included, indicating that the hindered settling of silt can be described by non-cohesive processes. In natural environments, the occurrence of the hydraulic transport of pure silt suspensions is not

known. More frequently, silt is transported together with clay aggregates at constant ratios. As a results, the ratio of the clay and silt fraction approaches constant values in morphological stable conditions, see Berger (1968) for example. When applying equation 3.6, it should be accounted for that the formula is derived for non-flocculated material. Particle aggregation has not been accounted for. The analysis demonstrates that hinder settling in graded (fine) sediment is important.

Based on the experimental results, sedimentation theory established for cohesive sediment has been extended to non-cohesive fine-grained sediment. The hindered settling formulation for silt can be used for modelling purposes (hydraulic engineering) and optimization of sediment transport issues (river engineering). The applied measurement technique and analysis show that by constructing isolutes in the (*t*,*z*)-plane, even a single-point timeseries measurement of suspended sediment concentration in a settling column can provide *i*) the particle size distributions and *ii*) the hindered settling of silty sediment.

Table 3-4 Overview of parameters and definitions as used in hindered settling formulation for sand, silt and clay.

Fraction	Eq.	Return flow parameter *m*	Relative volumetric solid content	Increased viscosity formula	Return flow and wake formation
Sand	3.19	Not applicable	$\phi = \phi_s / \phi_{s,\min}$	Implicitly accounted for	-
Silt	3.21	$1<m<2$	$\phi = \phi_s / \phi_{s,\min}$	$\left(1-\phi_s / \phi_{s.\max}\right)^{-2.5\phi_{s,\max}}$	$\left(1-\phi_s / \phi_{s,\min}\right)^m$
Clay	3.22	$m=2$	$\phi_f = c / c_{gel}$	$1+2.5\phi_f$	$\left(1-\phi_f\right)^m$

Chapter 4

Compaction and deposition of silt

4 Compaction and deposition of silt

4.1 Introduction

4.1.1 Consolidation and compaction

During consolidation of cohesive sediment beds, effective stresses build up and flocs break up, which is accompanied by a volume reduction of the sediment mass. The physical processes controlling the consolidation of cohesive sediments are described extensively (Terzaghi and Fröhlich, 1936, Been, 1980, Bowden, 1988, Toorman, 1999, Merckelbach, 2000, Winterwerp and Van Kesteren, 2004, Dankers, 2006). Figure 4-1 shows typical profiles of hydrostatic pressures (p_{hydr}), total water pressures (p_{wat}) and excess pore-water pressures (p_e) in a partly settling and partly consolidating cohesive sediment-water mixture.

The limited amount of available data (Jepsen et al., 1997, Roberts et al., 1998) on the compaction process of silt beds shows that, also in freshly deposited silt beds, the volume of the total sediment mass reduces with time, which suggests that excess pore-water pressures are being generated and dissipated in the bed. Over time, these excess pressures are assumed to dissipate until the pore-water pressure equals the hydrostatic pressure. However, these studies do not elaborate on the physics that control the underlying mechanisms. Whether hydrostatic, total and excess pore-water pressures in compaction silt beds resemble the profiles as shown in Figure 4-1 is hence unknown. Nonetheless, the results suggest that the bed's permeability is controlling the compaction of silt. The compaction process is further elaborated on in section 4.1.2. In this chapter more insight into the physical processes governing the compaction of silt beds is obtained by means of laboratory experiments.

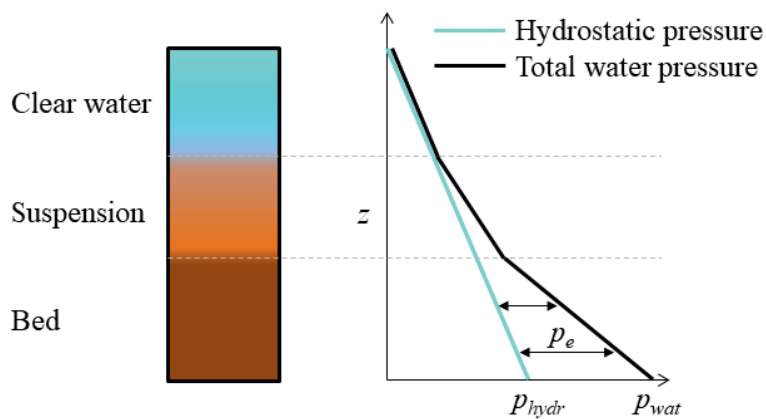

Figure 4-1 Hydrostatic pressure (p_{hydr}) and total water pressure (p_{wat}) in partly settling and partly consolidating cohesive sediment-water mixture. Arrows indicates the excess pore-water pressure (p_e).

4.1.2 Compaction of silt

The compaction behaviour of silt is compared with the consolidation behaviour of cohesive sediment. First, a homogeneous cohesive sediment-water mixture is considered which is initially in the stage of (hindered) settling (Figure 4-2). During settling, two interfaces develop in the (z,*t*)-plane: a lower rising bed – mixture interface, and an upper falling mixture – water interface. The point where the rising and falling interface intersect is referred to as the point of contraction. The bed below the lower interface carries the weight of the sediment above this plane and is in a state of consolidation. At the onset of consolidation (phase I), flocs first come in contact with each other and effective stresses (σ_v') are small. In a later stage of consolidation (phase II), effective stresses are generated due to the self-weight of the sediment and the dissipation of excess pore-water pressures. The process of consolidation comes to halt when all excess pore-water pressure has dissipated.

The physical processes governing the two stages of consolidation can mathematically be described by the Gibson (1967) equation, based on which a set of equations for the consolidation of sand-mud mixtures at low sand concentration is derived by Merckelbach et al. (2002) and Merckelbach and Kranenburg (2004). Below (equation 4.1), the consolidation equation for mud is presented:

$$\underbrace{\frac{\partial \phi_s^m}{\partial t}}_{\text{term 1}} + \underbrace{\frac{\partial}{\partial z}\left(k \frac{\rho_s - \rho_w}{\rho_w} (\phi_s^m)^2 \right)}_{\text{term 2}} - \underbrace{\frac{\partial}{\partial z}\left(\frac{k \phi_s^m}{g \rho_w} \frac{\partial \sigma_{zz}^{sk}}{\partial z} \right)}_{\text{term 3}} = 0 \qquad 4.1$$

where, ϕ_s^m is the solid content of mud, k is the permeability, ρ_s is the solid density, ρ_w is the water density and $\delta\sigma_{zz}^{sk} / \delta z$ is the vertical effective stress gradient. It is noted that the Gibson equation has been derived for the consolidation of mud. Nonetheless, in this chapter the compaction process of silt beds is compared with the consolidation process of mud beds by means of the Gibson equation. During consolidation phase I, effective stresses in a consolidating mud suspension are in a phase of build-up and are generally low. The generation of effective stresses is caused by the compression of flocs and is hence the results of the outflow of porewater. Therefore, it may be argued that term 3 is of less importance during consolidation phase I.

To verify latter argument, the timescales of term 2 and term 3 of equation 4.1 are quantified. The timescale of term 2 follows from the solution of equation 4.1 in which term 3 is neglected and relates to:

$$T_{\text{term 2}} \propto \frac{\delta}{k\phi} \qquad 4.2$$

Similarly, the timescale of term 3 follows from the solution of equation 4.1 in which term 2 is neglected and relates to:

$$T_{\text{term 3}} \propto \frac{\delta^2}{c_v} \tag{4.3}$$

in which δ is the initial thickness of the sediment layer (order decimetres) and c_v is the consolidation coefficient. For silt, typical permeability values are in the range of $1x10^{-6}$ to $1x10^{-8}$ m/s, typical values for c_v are in the range of $1x10^{-5}$ to $1x10^{-6}$ m^2/s (Mohr et. al., 2013) and typical solid fractions are in the range of 0.4 to 0.5. For mud, typical permeability values follow from a fractal approach (Merckelbach and Kranenburg, 2004) and are in the order of $1x10^{-4}$ to $1x10^{-5}$ m/s at the onset of consolidation. Values for the coefficients of consolidation are in the order of $1x10^{-7}$ to $1x10^{-8}$ m^2/s. For silt, the timescale of term 2 is indeed found to be several orders of magnitudes larger than for term 3, whereas for mud, the timescale of term 3 is dominant.

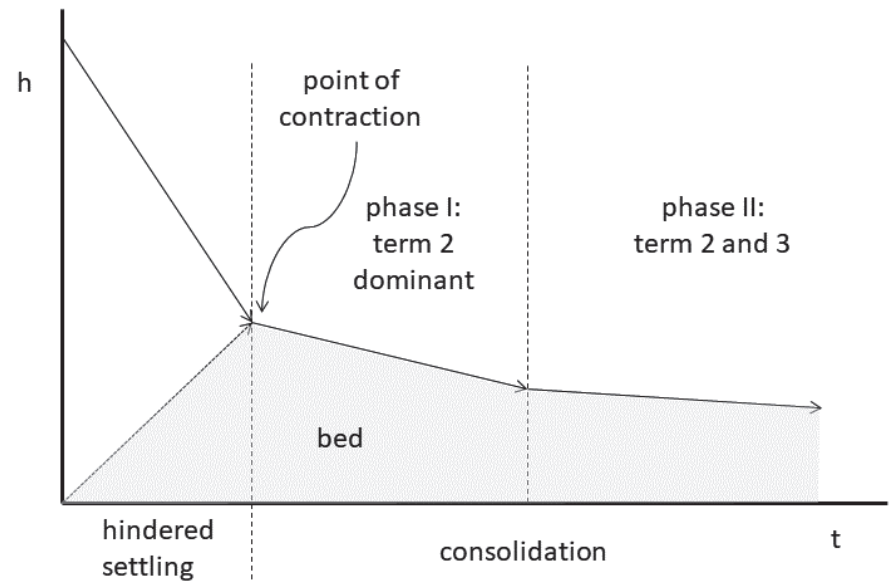

Figure 4-2 Development of interfaces in a settling and consolidating cohesive sediment-water mixture. Solid black line indicates the falling sediment-water interface. Black dotted line indicates the rising bed-mixture interface. Grey shaded area presents the volume occupied by the bed.

The compaction process of silt beds is considered to be partly analogous to the consolidation process of mud beds. For excess pore-water pressures to develop in silt beds, it is anticipated that the timescale for bed formation should be sufficiently small for water to be captured within the bed. The generation of excess pore-water pressures result in low effective stresses. Pore-water flow, which is controlled by the beds permeability, results in the dissipation of excess pore-water pressures in compacting silt beds. A sufficiently low permeability results in compaction within a measurable timeframe. Effective stresses are thus considered to be low during the initial stage of compaction. With the argument that term 3 of the Gibson equation

is of less importance during the initial stage of compaction, a simplified Gibson equation, where term 3 is neglected, and in which term 2 includes the permeability parameter, is considered to be suitable to describe the initial compaction process of silt. This is also convenient, since fluid flow is the dominant process during (hindered) settling, and hence allows for a continuous mathematical description of the hindered settling phase and initial compaction. Moreover, the permeability parameter can easily be quantified with the Kozeny-Carman equation (explained in the next section).

4.1.3 Permeability of silt beds

Formulae predicting the permeability of porous media are widely available (Lambe and Whitman, 1979, Carrier, 2003, Chapuis and Aubertin, 2003). An important general conclusion of these studies is that the permeability of soils can be accurately modelled as long as clay particles are absent. A common method to compute the permeability of granular beds is by using the classic Kozeny-Carman (KC, Kozeny (1927) and Carman (1938 and 1956)) equation which relates permeability k to the void ratio e by:

$$k = C_{kc} \frac{g}{\mu_w \rho_w} \frac{1}{S^2 D_R^2} \frac{e^3}{1+e} \tag{4.4}$$

Here, μ_w is the fluid's dynamic viscosity (10^{-3} Ns/m^2 at 20 ^{o}C), g is the gravitational acceleration, ρ_w is the density of the pore fluid, S is the surface area per unit mass (specific surface area), $D_R = \rho_s / \rho_w$, and C_{KC} is an empirical parameter, for which Carman (1939) found an optimum value of 0.2 to fit experimental data. Equation 4.4 is rewritten in terms of the solid content ϕ_s using $\phi_s = 1/(1+e)$:

$$k = C_{kc} \frac{g}{\mu_w \rho_w} \frac{1}{S^2 D_R^2} \frac{(1-\phi_s)^3}{\phi_s^2} \tag{4.5}$$

The specific surface area S can be calculated by:

$$S = \frac{F}{\rho_s} \sum_1^N n_i / d_i \tag{4.6}$$

where F is a shape factor to account for angularity of individual soil particles (see Table 4-1), d_i is the mean particle size of a size bin of the grain size distribution and n_i is volume percentage of particles in the corresponding bin. In Figure 4-3 the specific surface area is presented for uniform spheres as a function of particle size. Below d = 10 μm, the specific surface increases rapidly with decreasing particle size, indicating that a 'long tail' of small particles in the PSD has a large influence on the permeability of the soil.

Table 4-1 Shape factors (Fair and Hatch, 1933).

Shape	F
Spherical particles	6
Rounded particles	6.1
Worn	6.4
Sharp	7.4
Angular	7.7

Carrier (2003) accounted for the grain size distribution by using a more precise definition of d_i:

$$d_i = d_{ll}^{0.404} \times d_{lu}^{0.595} \quad 4.7$$

Here, d_{ll} is the lower limit of a size bin within the PSD, and d_{lu} the upper limit of the size bin. These limits are determined by the grain size measurement procedure. Note that the sum of the exponents in equation 4.7 is not equal to 1, which is probably the results of rounding off. Chapuis and Aubertin (2003) used the results of numerous permeability tests to assess whether the KC-equation provides good permeability predictions of homogenized specimens. They concluded that it can be used to estimate the k-value of a soil in the range of 10^{-1} to 10^{-11} m/s, usually within a factor 3 of the measured k-value. To further test the KC-equation for silt, permeability measurements have been carried out which are described in the next section.

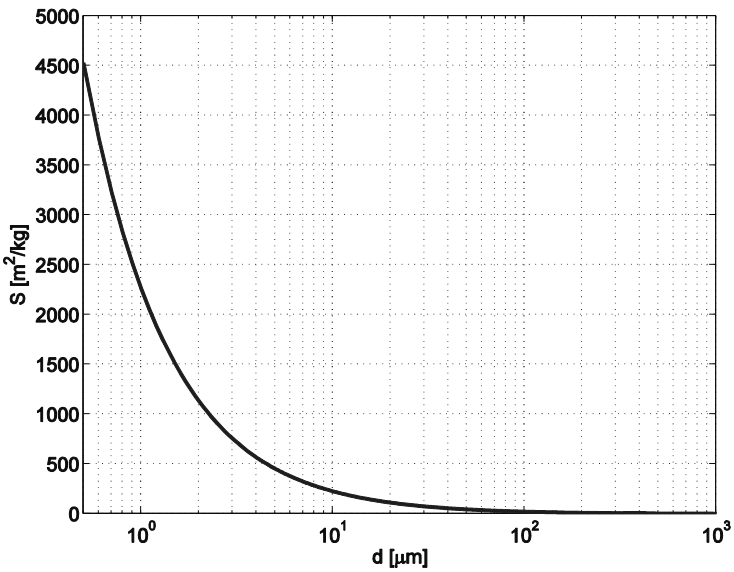

Figure 4-3 Specific surface area for uniform spherical particles as function of the particles diameter.

4.2 Experiments

Deposition experiments are carried out in the Fluid Mechanics Laboratory of Delft University of Technology. Settling columns (similar to the columns as described in **Chapter 3**), equipped with conductivity sensors and pressure gauges, are used to measure the evolution of the density and excess pore-water pressure over time. To verify the applicability of the KC-equation to silt, permeability values of pure silt mixtures are measured separately by means of a falling head apparatus at Deltares.

4.2.1 Permeability measurements

Experimental procedure

The goal of the permeability measurements is to test the application of the KC-equation (equation 4.5) to silt sized material. The permeability is tested by means of falling head tests (NEN-5124, 1993, ASTM-D5084, 2006). These tests are performed on four fine grained sediment mixtures, hereafter referred to as silt #4 to silt #7, of which the PSD's are presented in Figure 4-4 and characteristics are shown in Table 4-2. The specific surface areas are calculated using equation 4.7. Note that different sediments are used in the permeability experiments (silt #4 to #7) from the ones used in the deposition experiments (silt #1 to #3) for reasons of availability.

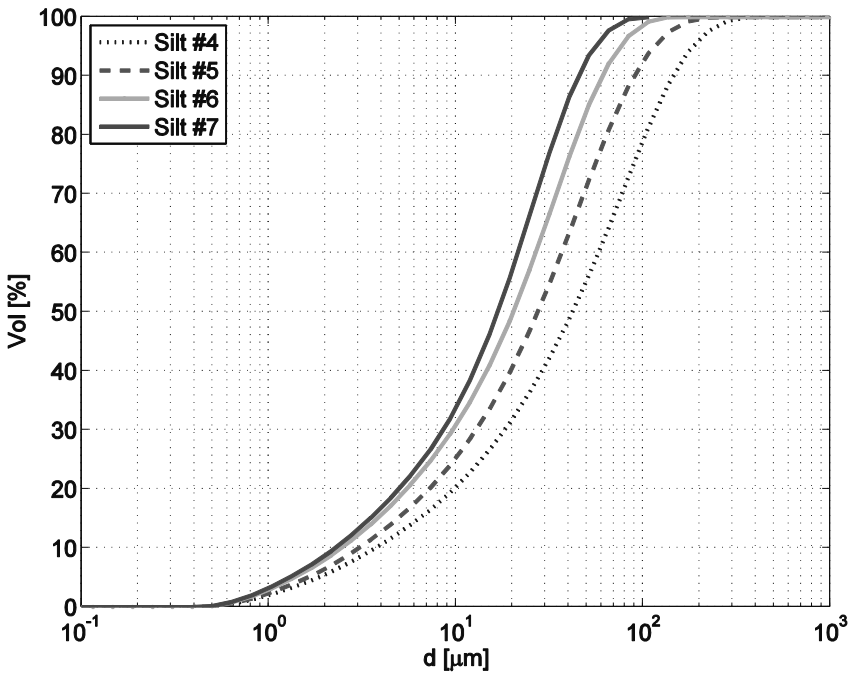

Figure 4-4 Grain size distribution of used sediment mixtures, measured with a Malvern.

Table 4-2 Mean particle size and specific surface area for silts used in falling head tests.

ID no.	d_{50} [µm]	S [m^2/kg]
Silt #4	42	2331
Silt #5	27	2797
Silt #6	20	3409
Silt #7	17	3719

The falling head permeability test involves flow of water through a soil sample (approximately 4 cm in height) connected to a standpipe, which results in a water level difference. The standpipe also allows measuring the volume of water passing through the sample.

For each test, a new sample was prepared. To obtain fully saturated soils, all samples were prepared in the experimental setup by gently pouring dried (24 hr at 105 °C) silt in de-aired and demineralized water. After pouring sufficient material in the experimental setup, a compressive load was applied to enable testing at multiple packing densities. The total mass and height of the soil samples was recorded to monitor the density. Next, a vertical head difference was applied, which generated an upward fluid flow through the sample. This yields a falling head as function of time.

The permeability measurements were performed at relatively high solid contents since the application of a compressive load hampers permeability measurements at solid contents close to the minimum packing. Producing a sample at its loosest packing is also cumbersome due to the generation of an overburden by the weight of the overlying grains. In latter situation the soil samples may not be isotropic.

The time required for the water in the standpipe to drop from the upper to the lower level is recorded. On the basis of the test results, the permeability of the sample can be calculated by equation 4.8, which is a practical application of Darcy's law ($Q=kAi$, where A is the cross section area to flow and i is the hydraulic head difference):

$$k = \frac{aL}{A\Delta t} \log \frac{h_u}{h_l} \qquad 4.8$$

in which a is the area of the standpipe, L is the height of the sample, A is the cross section of the sample and h_u and h_l are the upper and lower water levels in the standpipe using the same water head reference.

4.1.1 Deposition experiments

Sediment properties

The deposition experiments have been carried out in cylindrical settling columns as shown in Figure 3.6. Fine-grained sediment-water mixtures were allowed to settle and deposit at high initial concentrations. Similar sediment mixtures as in the hindered settling experiments described in **Chapter 3** have been used, of which the grain size distributions are shown in Figure 3.8. The corresponding characteristic diameters are shown in

Table 4-3. Note that these sediment mixtures differ from the sediment mixtures used for the permeability measurements in section 4.3.1.

Table 4-3 Properties of particle size distribution of used fine-grained sediment mixtures.

ID no.	d_{10} [µm]	d_{50} [µm]	d_{90} [µm]	d_{90}/d_{10} [-]	S [m^2/kg]
Silt #1	6	29	59	9.8	225
Silt #2	13	36	75	5.8	157
Silt #3	35	75	158	4.5	74

Experimental procedure

The sediment-water mixtures of silt #1, silt #2 and silt #3 were homogeneously mixed at initial solid contents of 0.47, 0.42 and 0.38, respectively. These high initial solid contents were chosen in order to have a substantial bed volume to monitor the ongoing physical processes and to minimize segregation during deposition. Solid content and pore-water pressure measurements have been carried out for a period of 18 days. The absolute accuracy of the solid content measurement is found to be ϕ_s=0.011 (section 3.4.2).

The pressure ports connected to the settling column were used to construct pore-water pressure profiles, see Figure 3.6. These ports are equipped with a porous polymer filter in the wall of the column to prevent sediment leaks. This means that in the tubes between the column and the pressure transducer, only pore fluid is present. The excess pore-water pressure profile was derived from the difference between the measured pore-water pressure and the hydrostatic pressure. In addition to the pore-water pressure and density measurements, the level of the water-bed interfaces was recorded with time.

4.3 Results and analysis

4.3.1 Permeability measurements

The results of the permeability measurements are shown in Figure 4-5. Since the specific surface areas increases from silt #4 to silt #7, a permeability reduction with increasing silt ID # is to be expected. In addition, for a single silt #, a permeability reduction with increasing solid content is expected from the KC-equation. It is noted that silt #6 shows the largest scatter in the permeability measurement. The falling head measurements show a trend of increasing permeability with increasing solid content for silt #4 and to a lesser extent for silt #5. Latter observations are in contrast with expectations. Interestingly, the solid contents of the samples increase with increasing grading (d_{90}/d_{10}). For silt #6 and #7 no clear relation between solid content and permeability was observed. The measurements further show a slight trend of increasing permeability with lower silt ID # (lower specific surface area): the measured permeability values of silt #4 and #5 are slightly larger than those of silt #6 and #7.

The anomaly found above may be the result of particle rearrangement and/or air inclusion within the sample during the measurement. The poorly noticeable trend of decreasing permeability with increasing solid content suggests that preparation methods may not be sufficiently accurate to produce homogeneous samples. Overall it is concluded that the influence of grading and particle arrangement (segregation) on the permeability is large. This

implies that the occurrence of segregation during the deposition experiments (discussed in the next section) may result in significant variations in the vertical permeability profile of the bed.

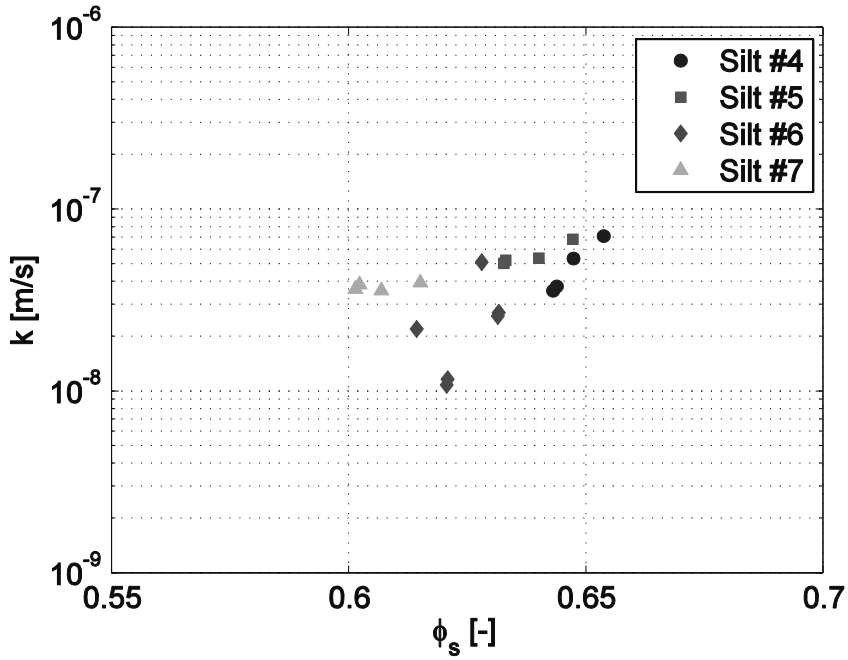

Figure 4-5 Results of falling head permeability measurements.

The measured permeability values of the fine grained sediment mixtures are compared with permeability values computed using the KC-equation (equation 4.5). The comparison (Figure 4-6) shows that the KC-equation overestimates the measured permeability. However, most data falls within the range of $[k/3 < k < 3k]$, similar to the measurement done by Chapuis and Aubertin (2003). Two measurement of silt #6 fall just outside this range. Nonetheless, based on present permeability experiments, the accuracy found by Chapuis and Aubertin (2003) is achieved and therefore it is concluded that the KC-equation is suitable to be used for the computation the permeability parameter for silt sized sediment in the present experiments.

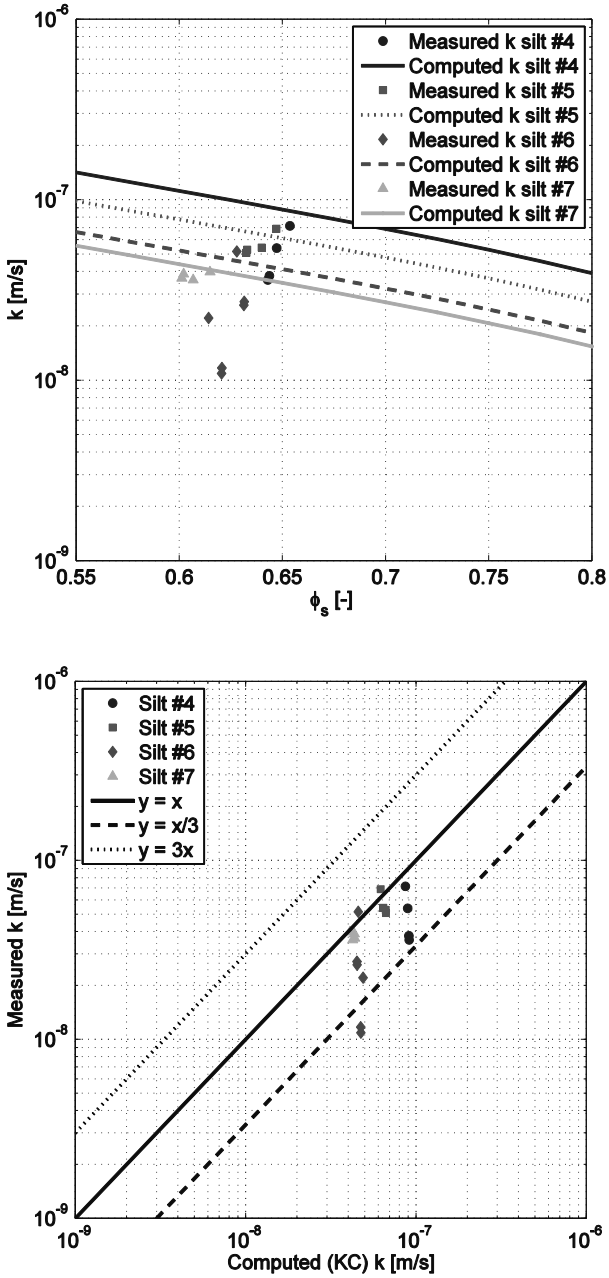

Figure 4-6 Upper panel: measured and computed (KC-equation) permeability as function of solid content. Lower panel: comparison of measured and computed permeability values.

4.3.2 Deposition experiments

After mixing the fine grained sediment-water mixture uniformly in the columns, the particles start to settle. A clear interface between the settling sediment-water mixture and the overlying water was visible. The development of the interface, relative to the initial interface level, shows a sharp transition (point of contraction), which characterizes the end of the hindered settling phase (Figure 4-7). The slope of the interface in the hindered settling regime represents an effective settling velocity, which is characteristic for the PSD and the initial concentration (see **Chapter 3**). Here, the focus will be on the processes beyond the contraction point, where the interface represents the bed level.

The bed level of silt #1 remained constant, whereas the bed levels of silts #2 and #3 lowered in time. The explanation of the stationary bed level of silt #1 can be twofold: *i*) the duration of the experiment is too short (18 days) or *ii*) silt #1 is not compacting. Solid content (Figure 4-9) and pore water (Figure 4-10) measurements indeed show that silt #1 is not compacting (discussed later in this section). The bed levels of silt #2 and silt #3 were lowering 0.65 cm and 0.70 cm over the first 17 and 18 days, respectively. Note that the bed of silt #3 showed a relatively large drop between days 7 and 8. The discontinuity was also observed in the pore water and density measurements, where both measurements showed a small increase after day 7. This may have been caused by external influences (for example vibrations) or local discontinuities in the bed (for example channel development).

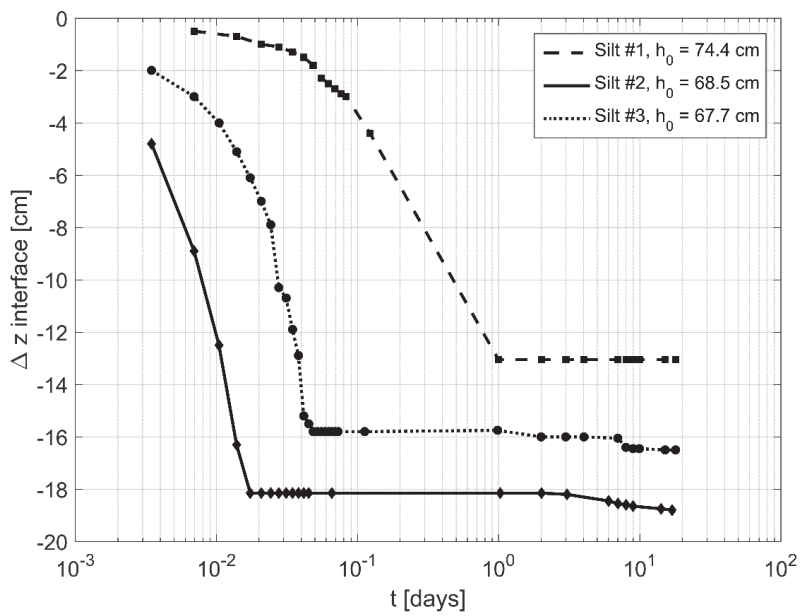

Figure 4-7 Interface development during deposition processes of silt # 1, 2 and 3.

In section 4.1.2 it was hypothesized, that the time scales for densification of silt beds are determined by the beds permeability. To test this hypothesis, the velocity of the pore water outflow is estimated from the experiments using three methods: *i*) volume balance based on volume occupied by the bed material, *ii*) volume balance based on density measurements, *iii*) volume balance of pore water. The results of these methods are discussed below. The compaction behaviour will be further discussed by comparing the velocity of the pore water outflow with the permeability value. The measured solid fractions in the bed are roughly between 0.45 and 0.6. Corresponding computed (with equation 4.5) permeability values are in the range of $5x10^{-5}$ to $1x10^{-6}$ m/s (Figure 4-8) and are used for the comparison.

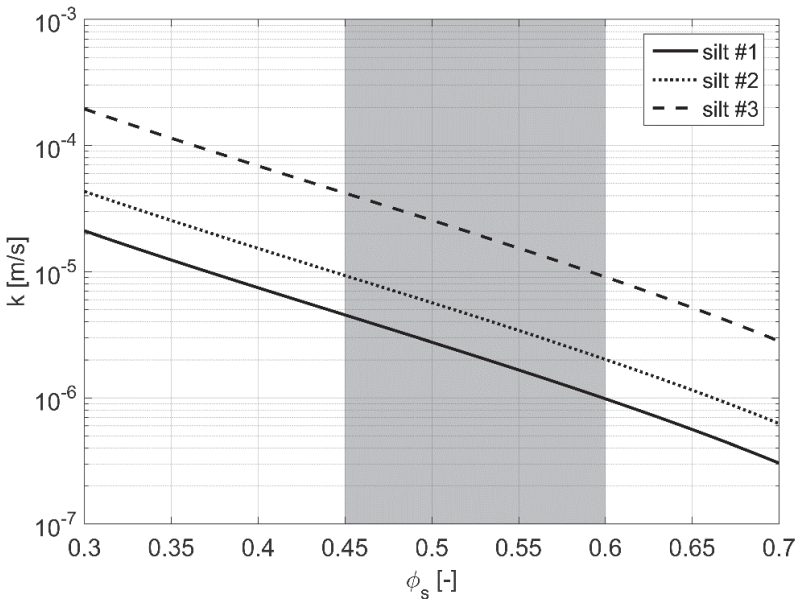

Figure 4-8 Computed permeability values (lines) of silt #1, silt #2 and silt #3, as function of solid content. The measured range of solid contents indicated by the grey area.

Method 1: volume balance of the bed material

An estimation of the permeability can be provided by assessing the average lowering of the bed levels in relation to the solid content increase over the first 17 and 18 days for silt #2 and silt #3, respectively. The solids content in the top layer of the bed upon reaching the contraction point, is approximately 0.51 and 0.49 for silt #2 and silt #3, respectively (Figure 4-9). The volume of solids V_{sol} that is replaced by water V_{wat} can be determined from the volume balance:

$$V_{tot} = V_{sol} + V_{wat} = \phi_s V_{tot} + (1-\phi_s)V_{tot} \qquad 4.9$$

The pore-water velocity in the bed is estimated from the volume of water that is expelled from the bed during the measurement. This results in average pore water flow velocities through the top layer of the bed of 1.6×10^{-9} m/s and 1.8×10^{-9} m/s for silt #2 and silt #3, respectively. These values are much lower than can be expected from the computed permeability. The difference will be discussed in section 0.

Method 2: volume balance following density measurements

The largest solid content increase (Figure 4-9) is observed between $t_{initial}$ and t = 1 day. In this period the mixture developed from a suspension into a rigid bed. After t = 1 day, the solid content development is approximately in the range of the accuracy of the measurement sensors (ϕ_s =0.011). In the bed of silt #1 no trend in solid content development can be observed and all profiles overlap within the range of accuracy. In the beds of silt #2 and #3 an increasing trend in solid content can be observed which is slightly larger than the accuracy of the conductivity sensors. The increase in solid content in the upper layers is slightly larger than in the lower layers of the formed bed.

Since silt #1 is not compacting during the observation period, only the solid content developments of silts #2 and #3 are further analysed. The average increase in solid content is approximately 0.020 and 0.015 for silt beds #2 and #3, respectively. The permeability is estimated following the volume balance as the total volume of particles replaced by water is directly related to the expelled volume of pore water. With the time needed for the water to flow out of the bed, pore water flow velocities are obtained, which are subsequently normalized with the height of the bed. This results in pore water flow velocities of 1.2×10^{-8} m/s and 1.0×10^{-8} m/s for silt #2 and silt #3, respectively, which are also much smaller than the Kozeny-Carman estimate.

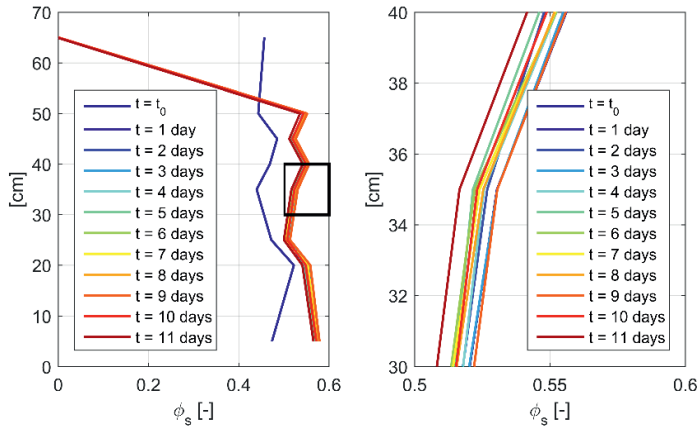

(a)

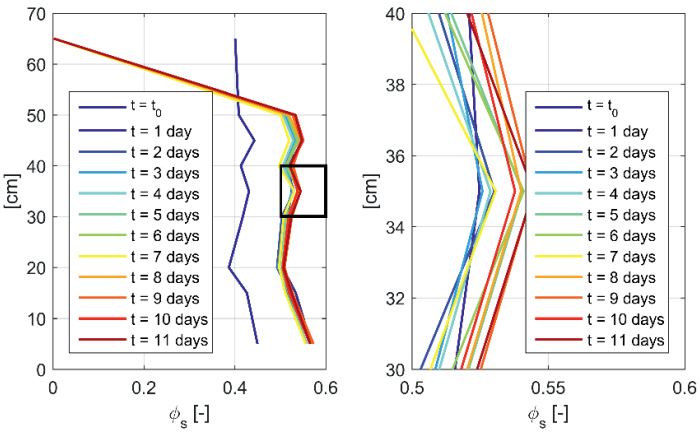

(b)

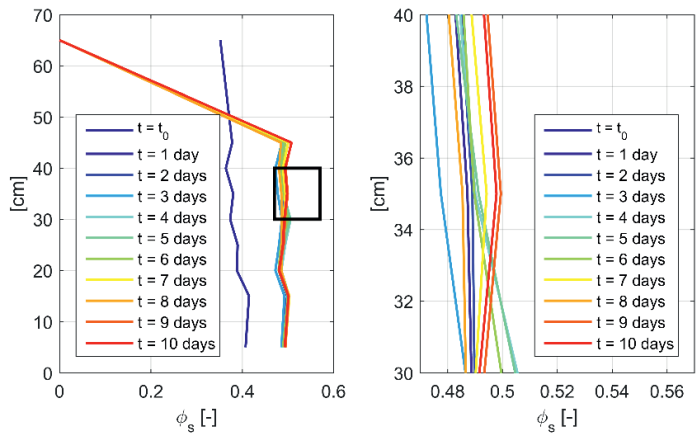

(c)

Figure 4-9 Solid content profiles and development in deposited beds of silt #1 (a), silt #2 (b) and silt #3 (c). Close ups of the delineated areas in the left panels is shown in right panels.

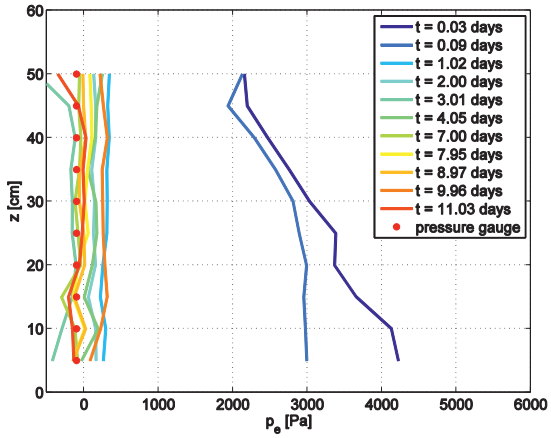

(a)

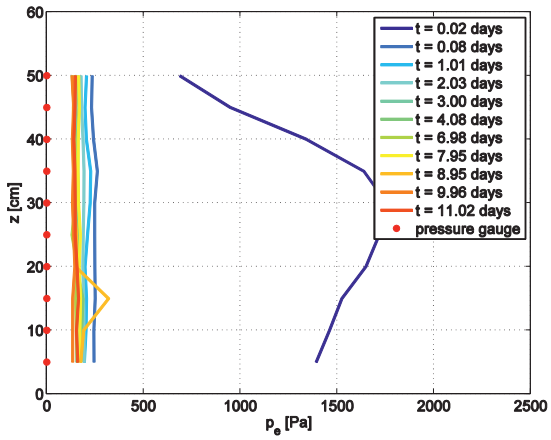

(b)

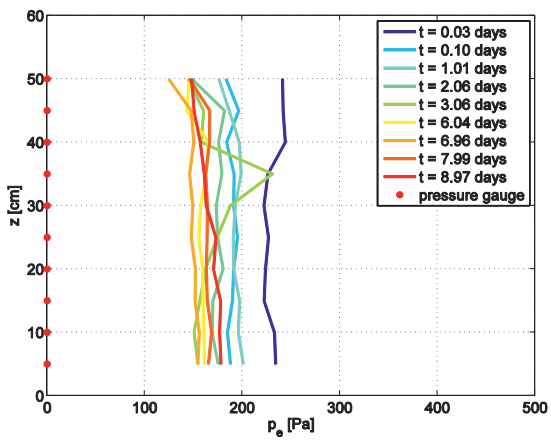

(c)

Figure 4-10 Development of p_e-profiles in deposited beds of silt #1 (a), silt #2 (b) and silt #3 (c).

Method 3: volume balance of pore water

The excess pore-water pressure (p_e) is defined as the difference between the total water pressure (p_{wat}) and the hydrostatic water pressure p_{hydr} ($p_e = p_{wat} - p_{hydr}$), where, p_{wat} is measured and p_{hydr} is computed. Excess pore-water pressures are characteristic for consolidating beds. Figure 4-1 shows a sketch of a hydrostatic, a total and an excess pore-water profile in partly settling and partly consolidating cohesive sediment-water mixture. The slope of the p_e-profile in the suspension is a function of the concentration (excess density of the overlying water). In the consolidation regime, the slope is a function of the consolidation time and the solid fraction of the overlying suspension. However, the p_e-profiles measured in present experiments are nearly all uniform over the depth (Figure 4-10). Exceptions are the profiles measured while the experiments were still in the hindered settling regime. For silt bed #1, the latter profiles can be found at t = 0.03 and t = 0.09 days and for silt bed #2 at t = 0.02 days.

In the bed of the finest sediment mixture (silt #1), the excess pore-water pressure profiles are all found close to 0 Pa after approximately 1 day. Hence, excess pore-water pressures are absent and no compaction is observed. The vertically uniform pore-water pressure profiles measured after deposition ($t > t_{contraction}$) in the beds of silt #2 and #3 are unexpected. The decreasing trend of measured p_e with time, however, suggests that these beds are in some state of compaction.

Low permeability crust

Figure 4-11 qualitatively shows the difference between the measured and expected excess pore-water pressure profiles. It is hypothesized that the measured vertically uniform p_e-profiles are the result of small permeability values in the upper layers of the deposited bed, which is likely to be formed by fine silt as a result of segregation. Apparently, the initial concentrations for the experiments with silt #2 and #3 was insufficiently high to prevent segregation. As a result, a low permeability crust was formed due to segregation during the hindered settling phase which was formed by the finer particles from the sediment mixture (see **Chapter 3**). Outflow of pore water from the lower layers through the crust is hampered due to the reduced permeability. Deeper in the bed, the permeability is sufficiently large to dissipate over- or under pressures which explains the locally uniform excess pore-water pressures. At the surface of the low permeability crust, the pore-water pressure equals the hydrostatic pressure. Therefore, it is assumed that a vertical p_e-gradient is only present over the low permeability crust.

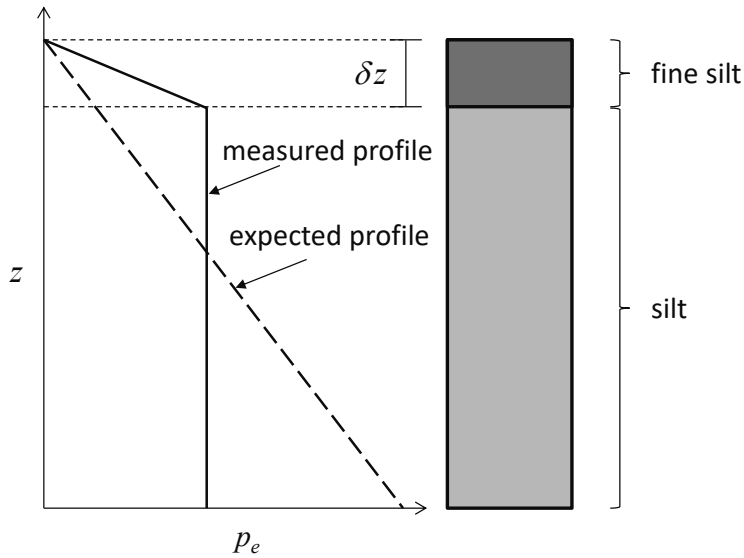

Figure 4-11 Layer of fine silt on top of the bed as a result of segregation in the stage on hindered settling.

To demonstrate the sensitivity of permeability to segregation, the permeability of silt #1 to #3 is shown for various solid contents as function of the percentage of largest particles in the particle size distribution (Figure 4-12). Here, 100% of largest particles on the x-axis implies that there is no segregation. A sharp decrease in permeability can be observed when less than 30% of the largest particles are still present in the PSD. With a lower percentage of largest particles present, the permeability decrease can be 3 to 4 orders of magnitude. For the smaller 10% of the silt particles, the permeability of silts #2 and #3 is in the order of 10^{-8} to 10^{-9} m/s, corresponding with the permeability values measured from the volume balances. The degree of segregation can be related to the permeability values. The above reasoning qualitatively supports the hypothesis that segregation results in the formation of a low permeability crust. The permeability of this crust will be analysed in more detail hereafter.

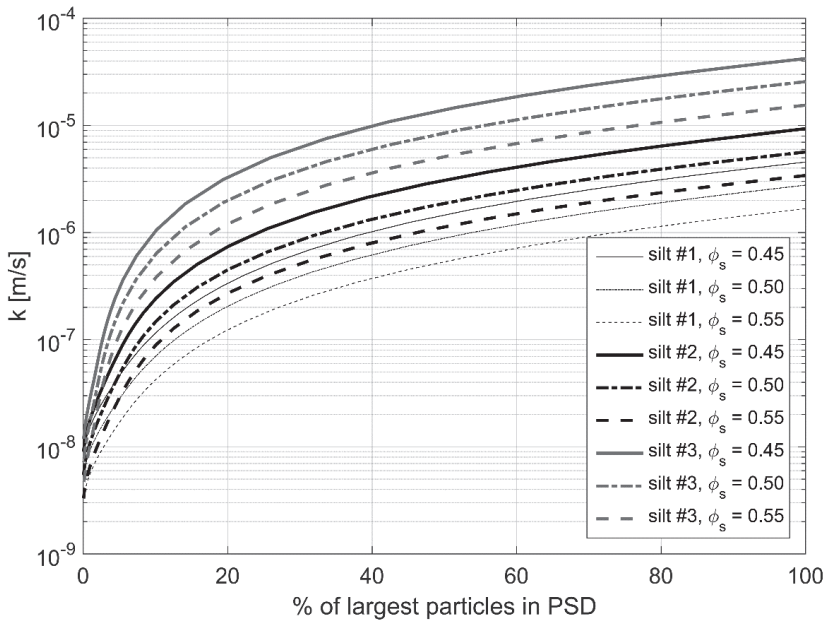

Figure 4-12 Permeability (KC-equation) as function of the percentage of largest particles of the particle size distribution present for different solid fractions.

The crust is too thin to directly measure its permeability. As an alternative, the fluid velocity resulting from the dissipation of excess pore-water pressure can be computed from the p_e-profiles over the top layer by means of a volume balance and the Darcy equation. Below, use is made of velocities of the fluid (v_f) and the particles (v_s). The volume balance reads:

$$\phi_s v_s + (1-\phi_s) v_f = 0 \tag{4.10}$$

Hence:

$$(v_f - v_s)(1-\phi_s) + v_s = 0 \tag{4.11}$$

And the Darcy equation reads:

$$(v_f - v_s)(1-\phi_s) = -k \frac{1}{g\rho_w} \frac{\partial p_e}{\partial z} \tag{4.12}$$

Substitution of equation 4.11 in equation 4.12 yields:

$$v_s = -k \frac{1}{g\rho_w} \frac{\partial p_e}{\partial z} \tag{4.13}$$

and substitution of $v_s = \frac{1-\phi_s}{\phi_s} v_f$ leads to:

$$\frac{1-\phi_s}{\phi_s} v_f = -k \frac{1}{g\rho_w} \frac{\partial p_e}{\partial z} \quad 4.14$$

Next, the relation between the excess pore-water pressure and the pore-water volume variation is given by:

$$p_e = g\rho_w h^* \quad 4.15$$

Of which the pore-water pressure flux is defined by:

$$\frac{\partial p_e}{\partial t} = g\rho_w \frac{\partial h^*}{\partial t} \quad 4.16$$

In which h^* is the change in height of the water column associated with the pore-water volume change due to the dissipation of overpressures. The temporal volume change of water is by definition equal to the fluid's velocity $\mathrm{d}h^*/\mathrm{d}t = v_f$ which leads to:

$$v_f = \frac{1}{g\rho_w} \frac{\partial p_e}{\partial t} \quad 4.17$$

Substitution of 4.14 into 4.17 results in:

$$\frac{1-\phi_s}{\phi_s} \frac{1}{g\rho_w} \frac{\partial p_e}{\partial t} = -k \frac{1}{g\rho_w} \frac{\partial p_e}{\partial z} \quad 4.18$$

Therefore, the values of $\mathrm{d}p_e/\mathrm{d}z$ are obtained from Figure 4-10 for silt #2 and #3. The non-zero values of $\mathrm{d}p_e/\mathrm{d}z$ are assumed to be located in the low permeability layer with thickness $\mathrm{d}z$. For silt #2, $\mathrm{d}p_e/\mathrm{d}t$ is approximately 10 Pa in 10 days ($1.2\text{x}10^{-4}$ Pa/s) while for silt #3, $\mathrm{d}p_e/\mathrm{d}t$ is approximately 20 Pa in 8 days ($2.9\text{x}10^{-5}$ Pa/s). By assuming zero excess pore-water pressures above the low permeability crust, values for $\mathrm{d}p_e$ are on average 210 Pa for silt #2 and 160 Pa for silt #3. Typical values of ϕ_s are 0.52 and 0.50 for silt #2 and silt #3, respectively.

The values of $\mathrm{d}z$ are estimated from the p_e-profiles and the location of the silt surface in the columns. The bed levels are in the order of cm's above the upper pressure gauge. In addition, the p_e-profiles are nearly all vertically uniformly distributed. Only near the surface some gradients occur over a 5 cm (measurement resolution) range in silt #3. Therefore, the maximum value of $\mathrm{d}z$ is assumed to be 5 cm, leading to pore-water flow velocities of $2.8\text{x}10^{-8}$ m/s and $9.0\text{x}10^{-9}$ m/s for silts #2 and #3, respectively.

Summary of permeability parameter analysis

The permeability of the deposited silt beds has been derived by three methods. The results are summarized in Table 4-4. It is concluded that the obtained permeability values fall within the range of (10^{-8} to 10^{-9} m/s). However, permeability values of silts #1, #2 and #3 computed with equation 4.5, are in the order of 10^{-3} to 10^{-4} m/s (Figure 4-8). This large difference is remarkable since the Kozeny Carman equation is well established in literature, and has been additionally verified for silt is in the previous section. The difference is attributed to the formation of a low permeability crust because of segregation during settling.

Table 4-4 Permeability values determined with varying methods.

Method	Silt #2 [m/s]	Silt #3 [m/s]
Method 1: Volume balance bed material	$3.2\text{x}10^{-9}$	$3.5\text{x}10^{-9}$
Method 2: Volume balance density development	$1.2\text{x}10^{-8}$	$1.0\text{x}10^{-8}$
Method 3: Volume balance pore water	$2.8\text{x}10^{-8}$	$9.0\text{x}10^{-9}$

4.4 Discussion

It is argued that crust formation is the physical mechanism behind the observed surprisingly low compaction rates of the silt beds. This also explains why the observed excess pore-water pressure profiles are vertically uniform, rather than increasing with depth as is common in consolidating cohesive sediment beds (Figure 4-1). Figure 4-13 illustrates the hydrostatic and total water pressure profile in the presence of a low permeability crust.

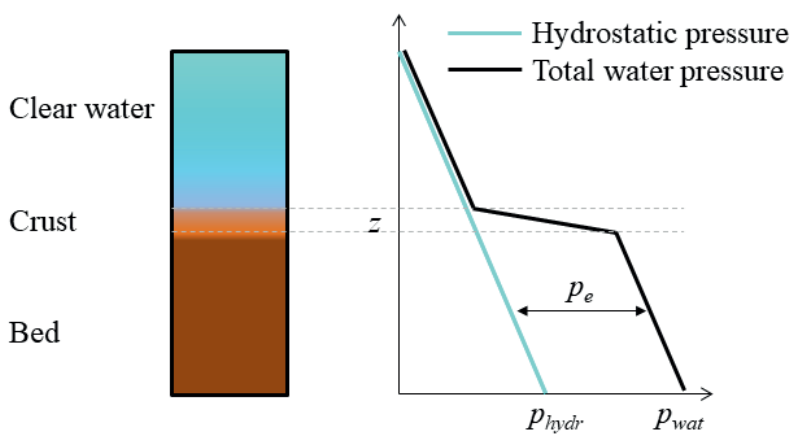

Figure 4-13 Hydrostatic pressure (p_{hydr}) and total water pressure (p_{wat}) in a segregated silt bed with crust formation. Arrows indicates the excess pore-water pressure (p_e).

Crust formation is likely heavily dependent on the way the bed is formed. Sleath (1999) points out that the solid content of the bed is also dependent on the way the bed is formed. The processes of crust and bed formation are illustrated in Figure 4-14 by initially homogeneously distributed graded sediment-water mixtures in panel A (low concentration) and in panel C (high concentration). During deposition segregation will occur. Effective settling velocities of different size fractions in the hindered settling regime are discussed in section 3.3. Lower initial concentrations lead to a larger spread of effective settling velocities and hence to a larger degree of segregation. Therefore, grains of identical size show a larger spatial distribution upon deposition at high initial concentrations (as illustrated in panel D). At low initial concentration, the smaller particles are more concentrated in the upper levels of the bed (as illustrated in panel B), thereby forming a crust.

The solid content of the less segregated bed is higher, since particles that fit within the pores of the larger particles are more dispersed. The bed's permeability therefore remains vertically uniform. In the situation where a crust is formed, the permeability value of the crust is governed by the small particles. Due to the lack of the larger particles in the layer, the specific surface area may increase significantly, which significantly lowers the permeability (see equation 4.6). Compaction can now occur if the bed is formed within the timescale of deposition, which allows for water to be captured within the bed.

To what extent the crust formation observed in the experiments resembles natural processes is unknown. However, crust formation in natural environments may impact morphological behaviour on larger scales. Crust formation may lead to armouring of the bed. Traditionally, armouring is referred to as the process where smaller particles are washed out of the bed, leaving the bed enriched with larger particles. The larger particles at the bed's surface have a higher movement threshold and therefore the total sediment transport decreases. Low permeability crusts are less susceptible to erosion, thereby also creating a more stable bed, although the particle size are now in the silt size range. This process can be referred to as "inverse armouring".

The lower layers are more susceptible to erosion. If under extreme conditions the crust is eroded, the lower layers will erode easier. Crust formation in natural environments can therefore result in morphological dynamic situations. However, the conditions under which a crust can form are scarce; the water column should be well mixed after which a low dynamic situation should be maintained during deposition. A possible location could be a sediment reservoir or an intertidal area after a storm.

The formation of a low permeability crust can be the results of inhomogeneity as well. A low permeability cohesive crust can also form on top of a sand layer, which segregates from a sand-mud mixture. The latter phenomena is discussed in **Chapter 6**.

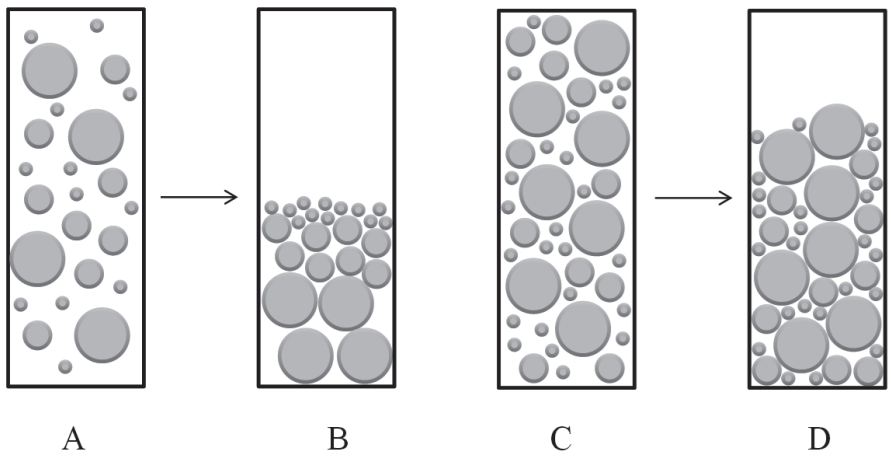

Figure 4-14 Conceptual processes illustrating the influence of initial concentration on segregation; a low initial concentration (A) results in more segregation than high initial concentrations (C).

4.5 Conclusions

In this chapter the physical processes controlling the compaction of silt beds are explored. Consolidation is traditionally referred to as a process that is characterized by flocculation and by low permeability values. The 'consolidation' of silt is referred to as compaction and is characterized by the permeability value only and its occurrence is a property of the deposition process in relation to the time scale of bed formation. The second term of the Gibson consolidation equation, which is largely determined by the beds permeability, is considered to govern the physical processes controlling the consolidation mechanisms of silt. Therefore, a simplified version of the Gibson consolidation equation, which neglects the third term, is considered suitable to study the compaction process of silt beds.

Deposition experiments have been carried out on fine-grained sediment-water mixtures with measurements of solid content timeseries and pore-water pressure timeseries. Compaction rates of the silt beds in present experiments are found to be reduced by segregation. Segregation drives the formation of a low permeability crust, hindering the dissipation of excess pore-water pressures. The degree of segregation depends on the boundary conditions for bed formation, for which the initial concentration is an important factor. Low concentrations lead to more segregation, resulting in the formation of low permeability top layers consisting of the smallest particles. The experiments confirm that the compaction rate of silt is determined by its permeability. The permeability range in which compaction of silt beds is observed is found at around 10^{-8} and 10^{-9} m/s, which relates to the finer fraction of the silty sediment.

Chapter 5

Erosion of silt

5 Erosion of silt[3]

5.1 Introduction

The erosion threshold and mobility of non-cohesive sand-sized grains depends on grain size only, and is reasonably well known from the empirical diagrams of Hjulstrom (1935) and Shield (1936), see for example Figure 2-7. These diagrams show a decreasing erosion threshold with decreasing grain size ($d_{50} > 50$ μm). More recent work reveals that, for fine-grained granular sediment in the silt-size range ($d_{50} < 50$ μm), the erosion threshold increases with decreasing grain size (see amongst others Dou (1960), Dou et al. (2001), Roberts et al. (1998) and Van Rijn (2007) for an overview). Latter increases in the erosion threshold is considered to be an effect of the changing hydraulic roughness since the bed irregularities (particles) do not longer exceed the thickness of the viscous sublayer. Typical erosion rates of fine sand and silt are presented in Briaud et al. (2001). It is noted that most formulations for erosion thresholds and erosion rates for fine-grained sediment are highly empirical. Existing erosion formulations dedicated to the erosion rates of silt beds follow mechanistic approaches or find their origin in quantification of intermolecular forces. Mechanistic approaches are applied amongst others by Lick et al. (2004), Zanke (1997, 2003) and partly by Miedema (2011). An explanation of the additional cohesive effect caused by intermolecular (Van-der-Waals) forces or surface tensions within the silt-water matrix is presented in Ternat et al. (2008). The effects of varying pH and salinity, which are likely to be of influence on these electro-chemical forces, are not fully incorporated in these mechanistic and electro-chemical approaches.

Roberts et al. (1998) and Jin et al. (2002) concluded from erosion experiments with pure silt beds that bulk properties largely influence the erosion behaviour. In Roberts et al. (1998), notion is made of mass erosion. Such history effects and mass erosion suggest cohesive behaviour. The indications that the erosion of silt depends on bulk parameters of the soil may justify a soil mechanics approach for describing its erosion behaviour. Winterwerp and Van Kesteren (2004) present a classification scheme for the erosion of cohesive sediment, thereby distinguishing three erosion modes: floc erosion, surface erosion and mass erosion. To each mode, a different type of soil mechanical behaviour is attributed. Depending on *i*) the type and magnitude of the hydrodynamic forcing, *ii*) the relation between the time scales of the pore-water pressure dissipation and their driving forces, and *iii*) the actual stress state of the sediment bed in relation to its stress history, different erosion behaviour occurs (Jacobs, 2011). As indicated by Van Rhee (2011), the beds permeability is probably an important parameter to take into account.

The phenomena of surface and mass erosion have been described in section 2.3.4. This chapter focusses on particle erosion and surface erosion of silt beds. In analogy to the methodology applied by Winterwerp et al. (2012), a surface erosion formulation for silt-sized sediments is derived by following a soil mechanics approach. Erosion experiments have been performed to generate data for validation of the derived erosion formulation. It is envisaged that apparent cohesion plays a dominant role in surface erosion of silt beds. The term apparent cohesion is

[3] *Parts of this chapter are based on Te Slaa, S., van Maren, D. S., He, Q., & Winterwerp, J. C. (in preparation). Erosion of silt.*

introduced to distinguish from physico-chemical cohesion and is described in more detail in section 5.2. The existence of mass erosion in silt beds, as observed in the experiments by Roberts et al. (1998), is acknowledged but not further discussed.

5.2 Apparent cohesion

This section discusses the physical mechanisms underlying apparent cohesion, in particular with respect to the erosion of silt. For interactive processes between the bed and the water column, apparent cohesion originates from pore-water underpressures. The latter is emphasized by Mastbergen and Van Den Berg (2003), who argue that shear dilatancy of a sediment bed generates pore-water underpressures. The extent to which a silt bed can exhibit apparent cohesion depends on the solid content of the bed, the bed's permeability and the rate of shearing. During shearing of granular soils, the bed deforms which can manifest in three types of behaviour:

- Contraction in loosely packed soils: the total volume of a soil decreases during yielding;
- Dilation in densely packed soils: the total volume of a soil increases;
- No volume variation at yielding: the soil is in a critical state.

During dilatant deformation of densely packed soils, the intergranular spaces increase and locally underpressures are generated. These underpressures stiffen the granular skeleton and reflect an apparent strength. Underpressures dissipate by the inflow of water. For granular sediment, the dissipation rate depends on the permeability of the soil. In relatively low permeability (slow responding) soils, such as silt, pore-water overpressure and underpressures are more important than in high permeable soils (sand). When water can flow into the deforming soil within the time scale of shearing (direct response), the behaviour is drained and no apparent cohesion will occur. If the time-scale of the soil's response exceeds the time-scale of the loading, the behaviour is undrained and apparent cohesion can occur. Apparent cohesion is thus a form of undrained behaviour and is related to the driving forces.

The contribution of apparent cohesion to the strength of a bed can implicitly be accounted for in the undrained shear strength s_u. The yielding (failure) behaviour of the bed is qualitatively explained by means of typical shear vane test results as shown in Figure 5-1. Three examples of soil response with varying loading conditions during a shear vane test are discussed. The following basic assumptions are applicable: *i*) initial soil conditions are similar, *ii*) silt is frictional, *iii*) interlocking between the particles is neglected, *iv*) the particles do not deform, crush or break during shearing.

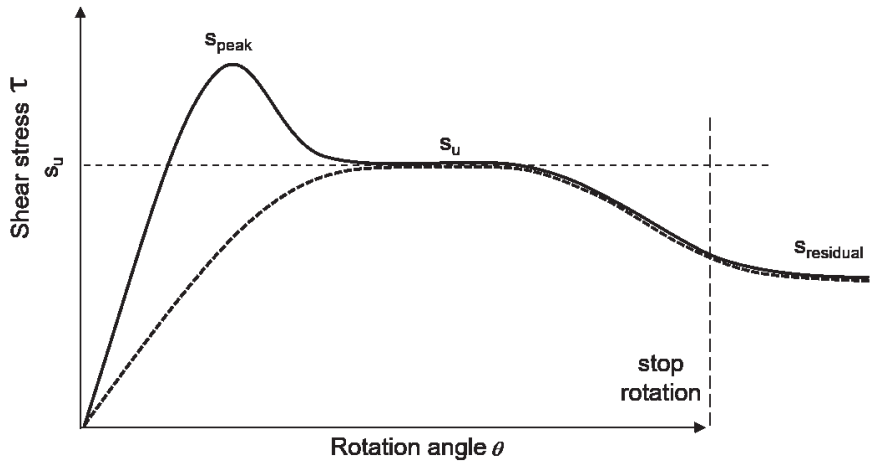

Figure 5-1 Qualitative soil response to different loading conditions during shear vane test.

In the first example (black solid curve) the rotation speed of the vane is relatively large compared to the deformation rate of the soil. As a result, large pore-water gradients and pore-water underpressures are generated. Pore-water cannot flow fast enough to compensate these gradients. The granular skeleton stiffens and reflects an apparent bonding strength: apparent cohesion. The soil response is referred to as undrained and the shear strength shows a stress peak s_{peak} in the curve. The value of s_{peak} depends on the rotation speed of the vane.

The second example (dashed black curve) shows the soil's response where the rotation speed of the vane is relatively slow compared to the dissipation rate of the soil. Pore-water gradients may develop but these are dissipated within the timescale of the loading. The response is drained behaviour and the shear strength develops towards the undrained shear strength s_u.

Upon stopping the rotation of the vane, the residual strength remains representing the internal resistance (friction between particles) of the soil at zero stress conditions. The drained shear strength s_d occurs only at the surface of the sediment bed. It is noted that the value of s_d can become very small.

The examples above illustrates that the granular skeleton in silt beds can stiffen during shearing, which reflects as apparent cohesion. The strength is referred to as the undrained strength $s_u(t)$, which decreases in time, due to inflow of water, from s_u towards s_d as shown in the sketch in Figure 5-2:

$$s_u(t) = s_d + \Delta s(t) \tag{5.1}$$

Where Δs is the apparent cohesion strength. Figure 5-2 shows that for larger void ratios e, s_u decreases to s_d, implying that low permeability soils with small void ratios are more receptive to manifest apparently cohesive behaviour. Because s_d can be very small, the most significant contribution to the soil's strength can be, depending on the shear rate, the apparent cohesion σ_{app}. The maximum value that σ_{app} can reach is Δs.

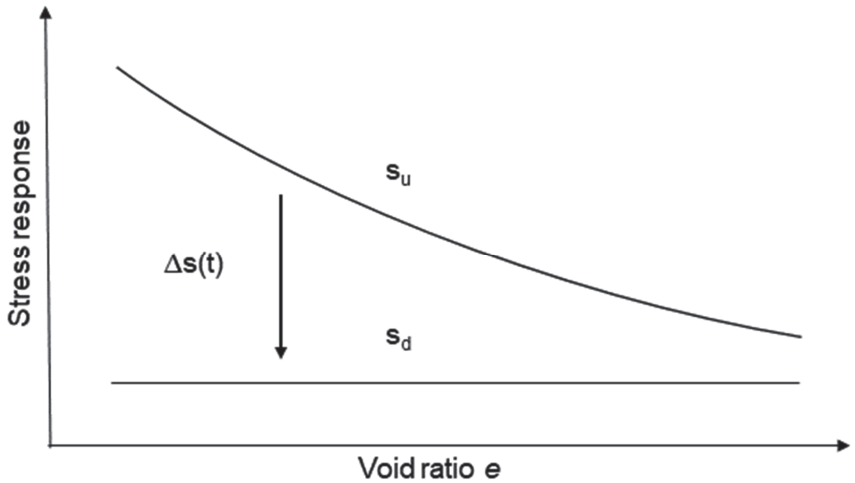

Figure 5-2 The drained strength s_d and the undrained strength s_u with decreasing apparent cohesion capacity with increasing void ratio.

5.3 Derivation of an erosion formulation for silt

5.3.1 Bed surface processes

Winterwerp et al. (2012) extended the work of Winterwerp and Van Kesteren (2004) and Jacobs (2011), to derive a formulation for the erosion of mud and sand-mud mixtures as a function of bulk material properties. In the following section, the Winterwerp (2012) formulation is adapted to make it suitable for the erosion of silt. For both erosion formulations, the Gibson (1967) consolidation equation (see section 4.1.2 for detailed description) is used as starting point and is presented below in terms of the void ratio *e*:

$$\underbrace{\frac{\partial e}{\partial t}}_{\text{term 1}} + \underbrace{(1+e)^2 \Delta \frac{\partial}{\partial z}\left(\frac{k}{(1+e)^2}\right)}_{\text{term 2}} + \underbrace{\frac{(1+e)^2}{g\rho_w}\frac{\partial}{\partial z}\left(\frac{k}{1+e}\frac{\partial \sigma_{zz}^{sk}}{\partial z}\right)}_{\text{term 3}} = 0 \qquad 5.2$$

where, k is the permeability, ρ_w is the water density, $\delta\sigma_{zz}^{sk} / \delta z$ is the vertical effective stress gradient and $\Delta = (\rho_s - \rho_w)\rho_w$ is the specific density. Winterwerp et al. (2012) argue that the response of a cohesive sediment bed to a hydrodynamic load by shear flow is governed by soil mechanical failure and hence relates the erosion of cohesive sediment to the bed's strength. The erosion formulation for cohesive sediment beds as presented by Winterwerp et al. (2012) is thereby related to Terzaghi's (1943) consolidation formula, and follows from term 3 in the consolidation equation (5.2). As such, the erosion formulation accounts for the effective stress.

The primary assumption underlying the erosion of silt beds is that at zero isotropic stresses at the bed's surface, the erosion behaviour is dominated by the dissipation of pore-water underpressures, as for cohesive beds. However, here it is assumed that for silty beds the

dissipation rate of pore-water underpressures is related to the permeability parameters and follows from term 2 in equation 5.2. By following the latter assumption, the Gibson consolidation equation can be simplified by neglecting term 3 because of the dominant term 2 in equation 4.1 (as discussed in section 4.1.2) and subsequently reduces to:

$$\frac{\partial e}{\partial t} + (1+e)^2 \Delta \frac{\partial}{\partial z} \frac{k}{\left(1+e\right)^2} = 0 \qquad 5.3$$

Note that equation 5.3 basically describes the classical Kynch simple wave equation. Rewriting and simplifying equation 5.3 (see text box 1 at the end of this section) under the assumption of negligible spatial variations in permeability leads to:

$$\frac{\partial e}{\partial t} + \underbrace{\frac{2\Delta k}{1+e}}_{V_s} \frac{\partial e}{\partial z} = 0 \qquad 5.4$$

Surface erosion can occur when a bed is at or below its critical state. Below the critical state, inflow of water has to take place before failure (erosion) can occur. The rate of volume increase relates to the velocity of the inflow front V_s and follows from equation 5.4:

$$V_s = \frac{2\Delta k}{1+e} = \frac{\mathrm{d}\delta_s}{\mathrm{d}t} \qquad 5.5$$

Where δ_s is the location of the inflow front below the bed's surface (see Figure 5-3). With ongoing inflow of water into the bed, the location of the inflow front δ_s propagates into the bed with velocity $\mathrm{d}\delta_s / \mathrm{d}t$. All sediment above the inflow front is at its critical state and can be eroded if the hydrodynamic stresses are sufficiently large. This implies that the maximum erosion velocity V_e is given by the propagation velocity of the inflow front; $V_e = V_s$.

At the bed's surface, the strength equals the drained shear strength, which reflects more or less the value of critical shear stress for erosion τ_{cr}. Surface erosion occurs when $\tau_b > \tau_{cr}$, for which τ_{cr} is considered as the onset for erosion. Deeper in the bed the strength increases to the undrained shear strength s_u. The erodible depth δ_e (note that the erodible depth is not the thickness of the layer of the sediment removed from the bed) and the length scale reflecting the dissipation process (the location of the inflow front measured from the bed surface, δ_s) are important during inflow. The location of the inflow front $\delta_s(t)$ depends on the hydraulic forcing in terms of the bed shear stress τ_b and the erosion velocity V_s, which largely depends on the permeability k. For $z < \delta_e(t)$, the strength $s^* = \tau_{cr}$, and the layer becomes mobile when flow-induced stresses exceed the critical shear stress for erosion $\left(\tau_b > \tau_{cr}\right)$. Pore-water underpressures have dissipated. For $\delta_e(t) < z < \delta_s(t)$, pore water underpressures are dissipating but the bed shear stress is not sufficiently large to mobilise the bed. For $z > \delta_s(t)$, the strength of the bed has not significantly decreased and still equals s_u^*.

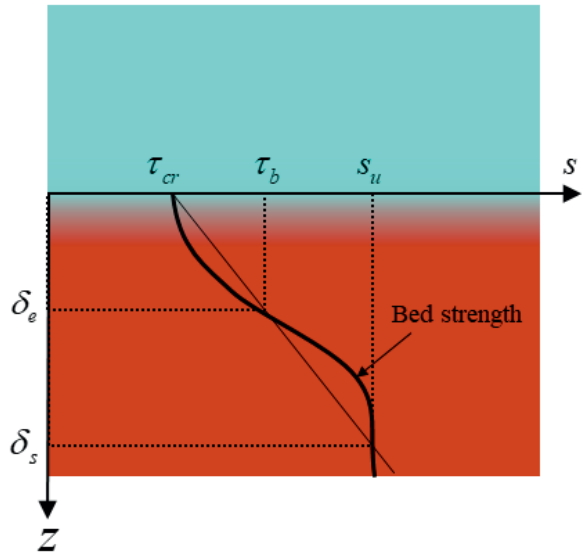

Figure 5-3 Sketch of strength distribution within the bed, and location of inflow front δ_s, the erodible depth δ_e and characteristics values for the various shear stress parameters are indicated. (Diagram is not to scale, redrawn after Winterwerp et al. (2012)).

The erosion rate E (which corresponds to V_e) is obtained from geometrical considerations (Figure 5-3) of *i*) the location of the inflow front δ_s, *ii*) the erodible depth δ_e, and *iii*) the distribution of the bed's strength over the depth. The relation between the erodible depth and the location of the inflow front follows from a linear approximation of the strength distribution within the bed:

$$\delta_e = (\tau_b - \tau_{cr}) \frac{\delta_s}{s_u - \tau_{cr}} = \delta_s \frac{\tau_b - \tau_{cr}}{s_u - \tau_{cr}} \tag{5.6}$$

And since $s_u >> \tau_{cr}$, equation 5.6 reduces to:

$$\delta_e = \delta_s \frac{\tau_b - \tau_{cr}}{s_u} \tag{5.7}$$

The erosion velocity V_e follows from differentiation in time:

$$V_e = \frac{\mathrm{d}\delta_e}{\mathrm{d}t} = \frac{\mathrm{d}\delta_s}{\mathrm{d}t} \frac{\tau_b - \tau_{cr}}{s_u} \tag{5.8}$$

Substitution of 5.5 in 5.8 leads to:

$$V_e = \frac{2\Delta k}{1+e}\frac{\tau_b - \tau_{cr}}{s_u} \qquad 5.9$$

The erosion rate is defined as the product of the erosion velocity and the bed dry density or concentration ($E = V_e \rho_{dry}$), resulting in a surface erosion formulation for silt:

$$E = \alpha \frac{2\Delta k}{1+e}\rho_{dry}\frac{\tau_b - \tau_{cr}}{s_u} \quad \text{for} \quad \tau_b > \tau_{cr} \qquad 5.10$$

In which α is introduced as a calibration parameter. The two dependent soil mechanical parameters are the permeability k and the void ratio e. The permeability of the bed can be computed using the Kozeny-Carman equation (equation 4.3), provided that the particle size distribution and void ratio are known. The critical shear strength for the initiation of motion τ_{cr} can be computed using the Van Rijn (2007) equation for the initiation of motion for fine sediment beds. The remaining unknown parameter in equation 5.10 is the undrained shear strength s_u.

The erosion formula (equation 5.10) predicts that the erosion rates is proportional to the sediments dry density, which seems contradictory. However, the role of the dry density cannot be analysed in isolation, as the dry density is related to the other sediment parameters k, e, τ_{cr} and s_u. Equation 4.5 implies that the permeability reduces, while e and s_u increase with increasing dry density. In addition, the erosion threshold (equation 5.14 in the next section) increases with increasing dry density. The nett effect is that the erosion rate is inversely proportional to the sediments dry density (and related parameters). It is envisaged that equation 5.10 is valid for the range of densities corresponding to the densities of deposited beds.

5.3.2 Erosion threshold

In this thesis, the critical shear stress for erosion is considered to consists of the erosion threshold of cohesionless particles $\tau_{cr,0}$ (further elaborated on later in this section) and a shear rate dependant apparent cohesion σ_{app}, hence $\tau_{cr} = \tau_{cr,0} + \sigma_{app}$. The erosion threshold thus implicitly reflects the apparently cohesive strength generated by pore water underpressures in the eroding layers of the bed.

Initiation of motion takes places under steady flow conditions when the dimensionless bed-shear stress θ is larger than a threshold value θ_{cr} (Van Rijn (2007). The dimensionless bed shear stress is defined as:

$$\theta = \tau_b / \left[\left(\rho_s - \rho_w \right) g d_{50} \right] \qquad 5.11$$

Here, τ_b is the bed shear stress. The θ_{cr} factor depends on the hydraulic conditions near the bed, the particle shape, and the particle position relative to the other particles. The hydraulic conditions near the bed can be expressed by the Reynolds number $R_* = u_* d / \nu$. The viscous effects (ν is the kinematic viscosity) can also be presented by a dimensionless particles parameter $D_* = d_{50}[(s-1)g/\nu^2]^{1/3}$ (Van Rijn, 1993, 2007). According to Van Rijn (1993), the critical bed shear stress for non-cohesive sediment can be best presented by:

$$\theta_{cr} = 0.115(D_*)^{-0.5} \text{ for } D_* < 4$$
$$\theta_{cr} = 0.14(D_*)^{-0.64} \text{ for } 4 \le D_* < 10 \quad 5.12$$

For silt, D_* is typically in the range of $0.07 < D_* < 1.2$. Next, Van Rijn accounts for cohesive influences of the fine particles through an empirical correction factor to compensate for the increasing critical bed shear stress with decreasing d_{50}, for which the following formulation has been suggested:

$$\tau_{cr} = \tau_{cr,0}\left(\frac{\phi_s}{\phi_{s,\max,\text{sand}}}\right)\left(\frac{d_{\text{sand}}}{d_{50}}\right)^{\gamma} \quad 5.13$$

Where $d_{50} < d_{\text{sand}}$, and $d_{\text{sand}} = 63$ μm, $\phi_{s,\max,\text{sand}}$ is the maximum solid fraction for sand (0.65), and γ is an exponent between 1 and 2.

5.3.3 Erosion parameter

Equation 5.9 can also be expressed as:

$$E = M_s(\tau_b - \tau_{cr}) \quad \text{for} \quad \tau_b > \tau_{cr} \quad 5.14$$

In which:

$$M_s = \alpha \frac{2\Delta k}{1+e}\rho_{dry}\frac{1}{s_u} \quad 5.15$$

Here, M_s is an erosion rate parameter for silt beds which will be derived experimentally in the remainder of this chapter. α can be used as a calibration parameter which accounts for uncertainties in *i*) the thickness of the eroding layer, *ii*) quantification of the apparent cohesion, and *iii*) the empirical Kozeny-Carman parameter C_{KC} in the Kozeny-Carman equation.

$$\frac{\partial e}{\partial t}+(1+e)^2\Delta\frac{\partial}{\partial z}\frac{k}{(1+e)^2}=0$$

$$\frac{\partial e}{\partial t}+(1+e)^2\Delta\left(\frac{\partial}{\partial z}\frac{k}{(1+e)^2}+\frac{\partial e}{\partial z}\frac{\partial}{\partial e}\frac{k}{(1+e)^2}\right)=0$$

$$\frac{\partial e}{\partial t}+(1+e)^2\Delta\left(\left[\frac{\partial}{\partial z}\frac{k}{(1+e)^2}+\frac{\partial e}{\partial z}\frac{2k}{(1+e)^3}\right]+\frac{\partial e}{\partial z}\left[\frac{\partial}{\partial e}\frac{k}{(1+e)^2}+\frac{\partial}{\partial e}\frac{2k}{(1+e)^3}\right]\right)=0$$

Assuming (1) constant vertical uniform permeabilty ($\partial k/\partial z=0$) and (2) neglible permeability differences ($\partial k/\partial e=0$) leads to:

$$\frac{\partial e}{\partial t}+(1+e)^2\Delta\left(\left[\cancel{\frac{\partial}{\partial z}\frac{k}{(1+e)^2}}+\frac{\partial e}{\partial z}\frac{2k}{(1+e)^3}\right]+\cancel{\frac{\partial e}{\partial z}\left[\frac{\partial}{\partial e}\frac{k}{(1+e)^2}+\frac{\partial}{\partial e}\frac{2k}{(1+e)^3}\right]}\right)=0$$

$$\frac{\partial e}{\partial t}+(1+e)^2\Delta\frac{\partial e}{\partial z}\frac{2k}{(1+e)^{-3}}=0$$

$$\frac{\partial e}{\partial t}+\frac{\partial e}{\partial z}\frac{2k(1+e)^2\Delta}{(1+e)^3}=\frac{\partial e}{\partial t}+\frac{2\Delta k}{1+e}\frac{\partial e}{\partial z}=0$$

Text box 1 Rewriting of equation 5.3

5.4 Erosion experiments

5.4.1 Experimental methods

Bed preparation method

A series of erosion experiments was performed on two fine grained-sediment mixtures (referred to as silt #8 and #9) at three bed densities (six combinations). Sediment beds were prepared in cylindrical containers (Ø=8.0 cm) that are compatible with the erosion apparatus. Saturation of the samples is obtained by mixing dried sediment with de-aired and demineralized water. Mixing rates are as high as possible to prevent segregation. Next, the sediment-water mixtures were allowed to deposit, whereby the density is controlled by varying the compaction time. Compaction times varied between 10 (immediately after deposition) and 36 hours after deposition. Even denser beds were obtained through mechanically densifying the deposited bed. For each bed prepared prior to an erosion test, a replicate bed was prepared following the same procedures. The replicate bed was used for reference measurements of solid content profiles by using a Conductivity Concentration Meter probe (CCM-probe).

Erosion experiment

A UMCES-Gust Erosion Microcosm System (Microcosm) was used to measure erosion rates at different bed shear stresses. Detailed information and theoretical background regarding the erosion apparatus is presented in Thomsen and Gust (2000). The principle of the Microcosm is to measure the amount of erosion as function of a varying (spatially homogenous) bed shear stress, which can then be converted into a critical shear stress for erosion τ_{cr} and the erosion rate parameter M_s. The set-up consists of the above mentioned cylindrical container containing a water column and a top lid (Figure 5-4). The top lid contains a rotating disk. The axis of the rotating disk is provided with a suction outlet and the top lid of the cylinder is provided with an inlet. The rotating disk generates a flow of water. The disk itself does not generate a fully uniform bed shear stress: the bed shear stress increases with distance from the centre of the container. To improve the spatial homogeneity of the bed shear stress, a flow of water is pumped through the cylinder (flow from the inlet to the outlet via the bed). The flow of water through the cylinder also affects the bed shear stress in the axis of the cylinder. To minimize latter effect, a small PVC disk is placed in the axis on the bed to block out the sediment that could be eroded due to the pumping.

The bed shear stress can be controlled by altering the rotation speed of the disk and the flow at predefined ratios. The calibration parameters for operating the Microcosm were obtained from De Lucas et al. (2013), who calibrated the apparatus by using sand sized sediment of various diameters for which the critical bed shear stress for the initiation of motion τ_{cr} is obtained from the Shield - Van Rijn diagram (Van Rijn, 1984).

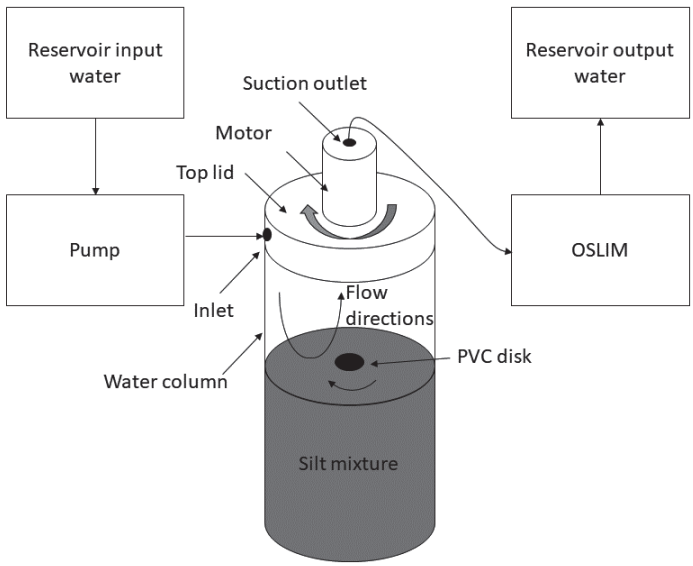

Figure 5-4 Schematic overview of setup Microcosm

Concentration measurements are carried out using a calibrated optical silt measuring system based on the attenuation intensity of light passing through a measurement volume (OSLIM). During an erosion experiment, the bed shear stress was increased in steps of 0.05 Pa every 30 seconds interval. From the measured concentration time series and the know flow Q, the eroded mass m can be computed per time interval Δt:

$$m = c \cdot Q \cdot \Delta t \qquad 5.16$$

Index density tests

The solid content at loosest and densest packing of both silt #8 and silt #9 was measured by following standard test procedures for measuring the maximum index density and unit weight of the soil (ASTM-D4253, 2006). Minimum and maximum solid contents were obtained by measuring the mass and volume of dried sediment in metal cylinders at the loosest and densest packing. The loosest packing was obtained by gently pouring the sediment in the cylinder and the densest packing was obtained through vibration (according standard) of the filled cylinder. Six packing measurements were carried out per sediment mixture; three for the loosest packing and three for the densest packing. Results of the density test are shown in Table 5-2. The results represent the average density of the sediment in the cylinder.

5.4.2 Sediment properties

The sediment used in the experiments was pure quartz. PSD's and characteristic parameters are shown in Table 5-1 and Figure 5-5. It is noted that despite the difference in particle size distribution, the specific surface areas are comparable. Results of the index density test are shown in Table 5-2. The permeability corresponding to the average minimum and maximum packing is computed with the Kozeny-Carmen equation (equation 4.3). Density measurements show that the influence of the gradation is large; the solid content of silt #8 is larger at both the minimum and maximum packing than for silt #9. This reflects as well in the corresponding permeability; despite the nearly similar specific surface areas and d_{50}, the computed permeability of silt #8 is one order of magnitude smaller than the permeability of silt #9.

Table 5-1 Properties of particle size distribution of used silts

ID	d_{10} [µm]	d_{50} [µm]	d_{90} [µm]	S [m²/kg]	d_{90}/d_{10} [-]
Silt #8	1.8	17.6	65.2	318	36.2
Silt #9	2.8	12.8	26.2	297	9.4

Table 5-2 Measured (ASTM-D4253) minimum and maximum packing density of silt #8 and #9.

Silt #8	$\phi_{s,\min}$ [-]	$\phi_{s,\max}$ [-]	$\rho_{dry,\min}$ [kg/m³]	$\rho_{dry,\max}$ [kg/m³]
Measurement 1	0.48	0.69	1272	1829
Measurement 2	0.48	0.68	1272	1802
Measurement 3	0.47	0.69	1245	1829
Average	0.48	0.69	1272	1829
***k* [m/s] eq. 5.11**	$4.3\text{x}10^{-6}$	$4.5\text{x}10^{-7}$	-	-

Silt #9	$\phi_{s,\min}$ [-]	$\phi_{s,\max}$ [-]	$\rho_{dry,\min}$ [kg/m³]	$\rho_{dry,\max}$ [kg/m³]
Measurement 1	0.40	0.59	1060	1564
Measurement 2	0.39	0.60	1034	1590
Measurement 3	0.38	0.61	1007	1617
Average	0.38	0.60	1007	1590
***k* [m/s] eq. 5.11**	$1.4\text{x}10^{-5}$	$1.5\text{x}10^{-6}$	-	-

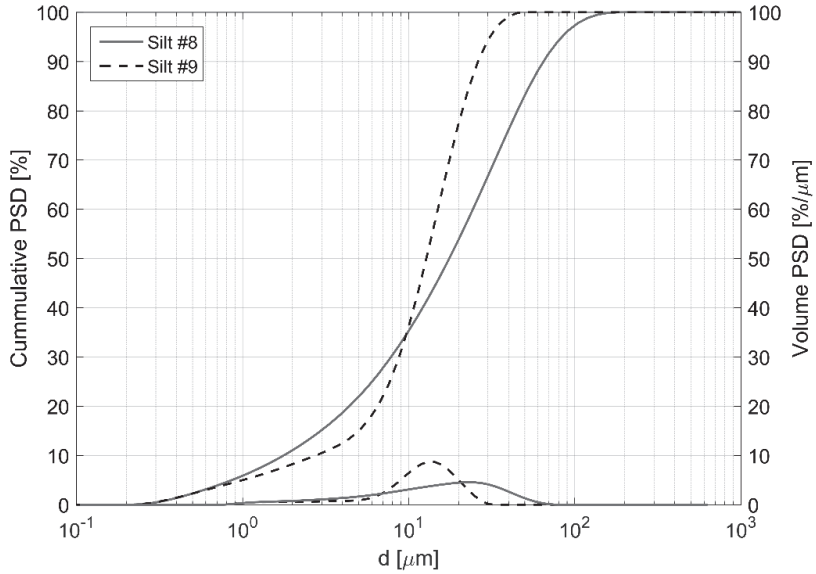

Figure 5-5 Volume and cumulative volume particle size distributions of silt #8 and #9.

5.4.3 Results erosion experiments

Solid fractions

Solid fraction profiles of the beds were measured in the reference containers by means of a conductivity concentration meter (CCM). The solid fractions at the three packing densities (ϕ_{s1}, ϕ_{s2} and ϕ_{s3}) as well as the solid contents at the loosest and densest packing obtained from the index density tests are shown in Figure 5-6 for each sediment mixture. It is assumed that no segregation has occurred. In addition, an uncertainty in the solid content measurement of 0.011 is assumed (section 3.4.2). The solid content at the beds surface is obtained by linear extrapolation of the solid content profile, see Table 5-3. For silt #8, packing ϕ_{s3}, insufficient data points are obtained for extrapolation and therefore the average value of the measurements is used as the solid fraction at the bed surface.

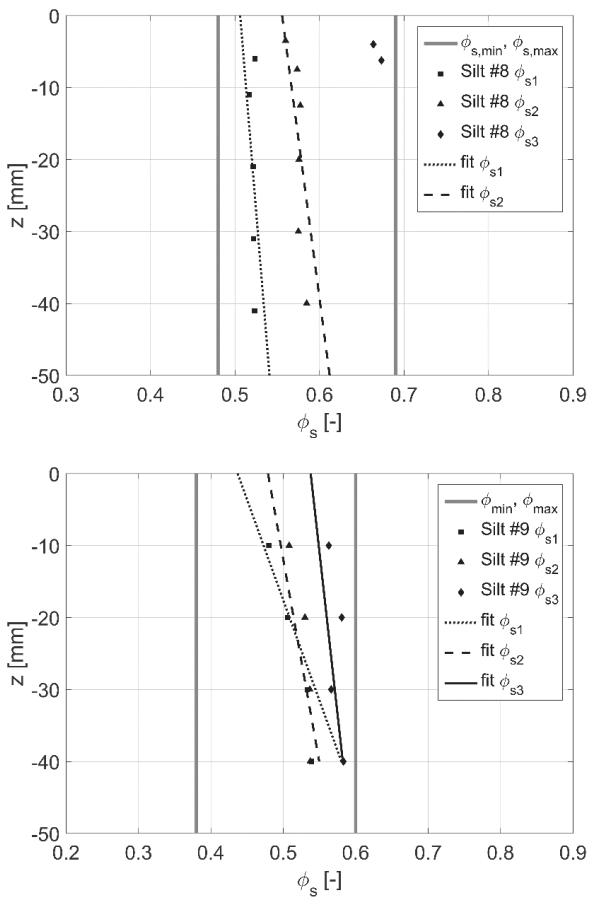

Figure 5-6 Measured solid content profiles in reference containers for silt #8 (top) and #9 (bottom) with boundaries of loosest and densest packing indicated.

Table 5-3 Surface solid contents of sediment mixtures used in the erosion experiments.

Packing ID	Silt #8	Silt #9
ϕ_{s1}	0.51 ± 0.011	0.44 ± 0.011
ϕ_{s2}	0.56 ± 0.011	0.48 ± 0.011
ϕ_{s3}	0.66 ± 0.011	0.54 ± 0.011

Results erosion experiments

The cumulative eroded mass and the exerted bed shear stress as function of time are shown for all erosion tests in Figure 5-7. Note the difference in the scale of the *y*-axis in the figures. The erosion behaviour in all experiments is comparable: at the smallest exerted shear stress no erosion is measured. Next, at higher shear stress erosion slowly starts. At even higher stresses the $(t,\Sigma m)$-curve steepens. In line with expectations, largest erosion rates are observed in beds with the lowest solid content. Erosion rates are higher for silt #9 than for silt #8 at equal solid contents of the bed.

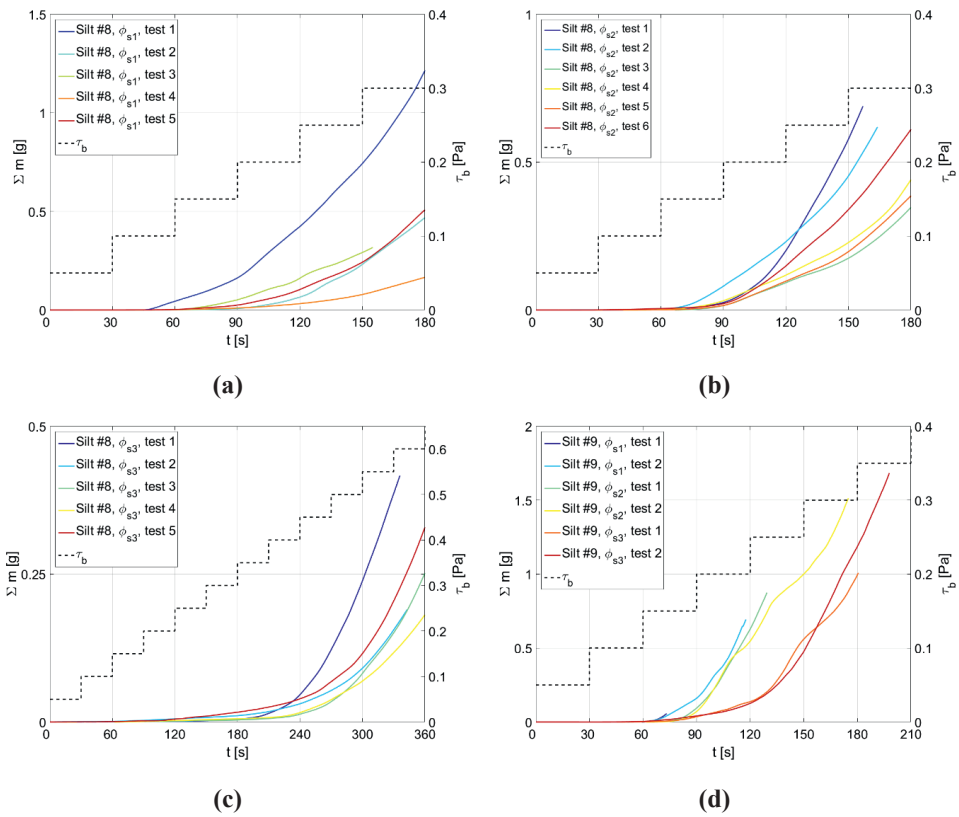

Figure 5-7 Cumulative concentration time series for varying packing of silt #8 in (a), (b) and (c) and for silt #9 in (d). Note the different vertical scales.

5.4.4 Analysis

Erosion behaviour

For every increment in τ_b, the erosion rate E [kg/m^2/s] is obtained from the slope of the $(t,\Sigma m)$-curves. The tangent along the $(t,\Sigma m)$-curve is nearly constant over the 30 second intervals, although irregularities are observed. During most intervals with constant τ_b, the measured (non-cumulative) concentrations tended towards an equilibrium, implying that erosion rates became constant. The observed behaviour in the cumulative erosion curves reflects in the erosion rates; at low τ_b erosion rates no erosion occurs, while at higher τ_b erosion rates increase linearly.

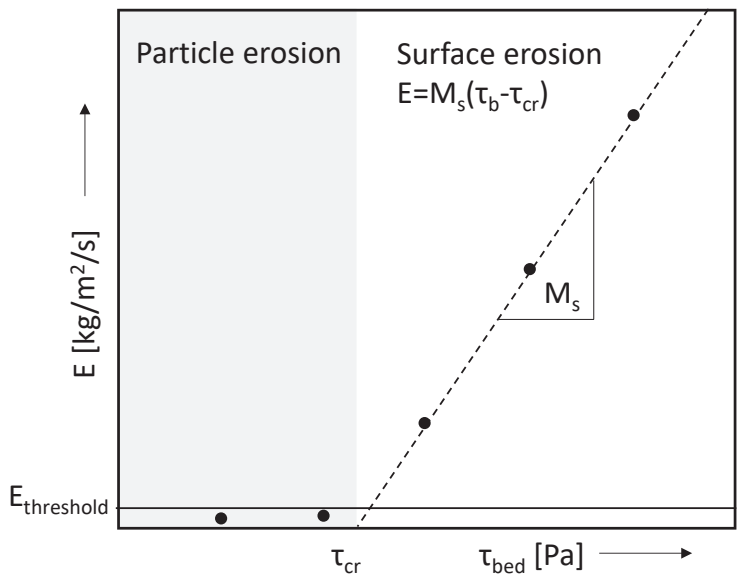

Figure 5-8 Sketch of typical observed erosion behaviour. Dots represent data points. Solid line represents a threshold (0.002 kg/m^2/s) above which data points are included in the linear fit (dotted line) to establish the erosion threshold τ_{cr} .

Two types of erosion behaviour can thus be distinguished, which are qualitatively indicated in the sketch in Figure 5-8 in terms of the erosion rate E (in kg/m^2/s) as a function of the bed shear stress. The first type is referred to as particle erosion and explains the non-zero erosion rates at the smallest τ_b. Particle erosion is attributed to irregularities in the bed and (turbulent) fluctuations in bed (shear) stress. Particles on top of the bed are not sheltered and erode easier. The second type of erosion behaviour refers to the shear stresses at which the erosion rate E shows a (linear) increase with τ_b. Here, it is referred to as surface erosion. The measured erosion rates are show in Figure 5-9 for silt #8 and silt #9 as function of τ_b. The erosion rates varies with about a factor 2 for beds with equal packing densities and PSD. The variation in erosion rates becomes less with increasing packing density.

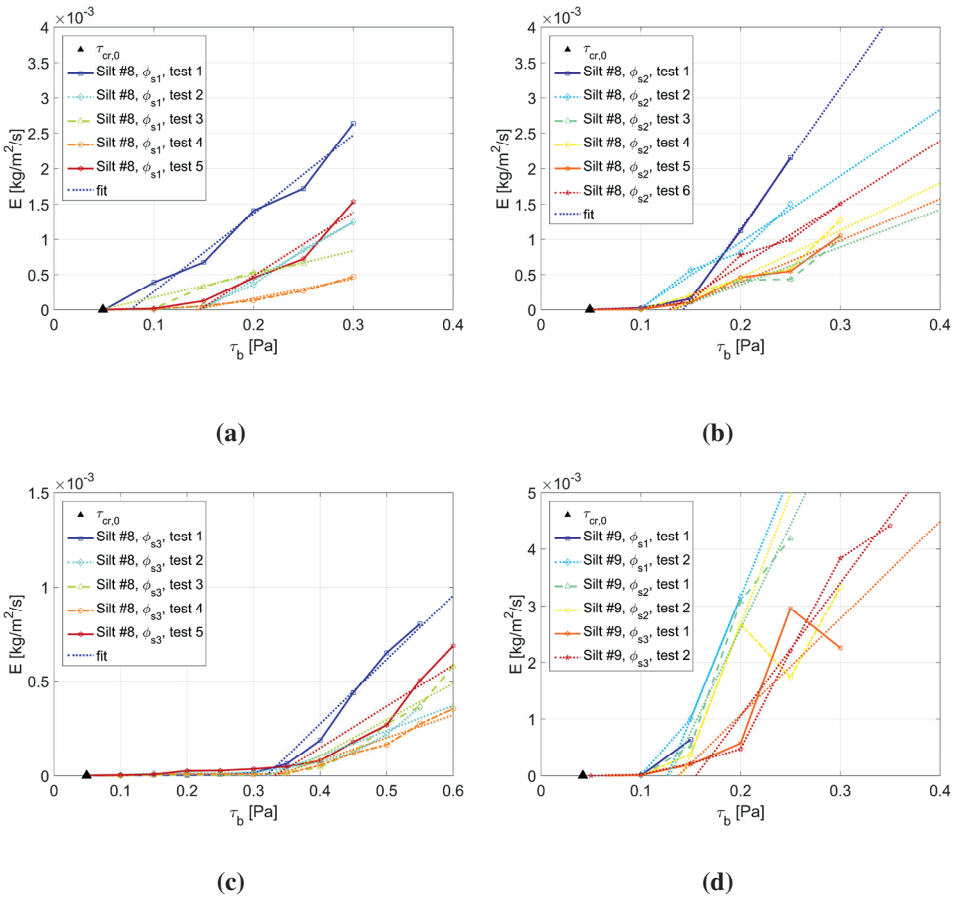

Figure 5-9 Erosion rates for varying packing of silt #8 in (a), (b) and (c) and for silt #9 in (d). The erosion threshold is indicated on the x-axis. Note different scaling between figures.

Erosion threshold

The experiments provide a dataset which can be tested against existing formula, for which the Van Rijn (2007) equation for the initiation of motion (equations 5.12 and 5.14) is considered most relevant. The erosion threshold τ_{cr} is defined by the onset of surface erosion and is obtained from a linear fit through all points for which $E > 0.002$ kg/m^2/s in the (τ_b, E) curve. The intersection with the *x*-axis defines the critical bed shear stress for erosion (τ_{cr}). The experimentally derived erosion thresholds are shown in Table 5-4 for silt #8 and in Table 5-5 for silt #9. For both silt beds, the erosion threshold is generally found to be between 0.1 and 0.2 Pa. The computed $\tau_{cr,0}$ for silt #8 and silt #9 is 0.049 Pa and 0.042 Pa, respectively, and is indicated in the x-axis in Figure 5-9.

Table 5-4 Measured erosion threshold τ_{cr} in [Pa] for silt #8, d_{50} = 18 µm

Packing ID	ϕ_s surface	Test 1	Test 2	Test 3	Test 4	Test 5	Test 6	Average
ϕ_{s1}	0.51 ± 0.011	0.077	0.149	0.047	0.142	0.146	-	0.112
ϕ_{s2}	0.56 ± 0.011	0.143	0.098	0.133	0.131	0.133	0.129	0.128
ϕ_{s3}	0.66 ± 0.011	0.319	0.320	0.344	0.332	0.332	-	0.329

Table 5-5 Measured erosion threshold τ_{cr} in [Pa] for silt #9, d_{50} = 13 µm

Packing ID	ϕ_s surface	Test 1	Test 2
ϕ_{s1}	0.44 ± 0.011	0.127	-
ϕ_{s2}	0.48 ± 0.011	0.129	0.142
ϕ_{s3}	0.54 ± 0.011	0.138	0.155

In section 5.3.1 it is explained that at the beds surface, the strength equals the critical shear stress for erosion. The difference between the measured and computed erosion threshold found here is attributed to the erosion apparatus used and the unambiguous definition of the initiation of motion. The initiation of motion criteria applied by Van Rijn (1993) is based on visual observations of particle movement close to the bed. However, in the Microcosm, initiation of motion is "observed" by the OSLIM beyond the suction outlet (Figure 5-4). Hence, more energy is required to "observe" the initiation of motion in the Microcosm than in the straight flume experiments as it requires transport of particles from the bed up to the OSLIM. The latter explains why erosion thresholds measured here are higher than the computed erosion threshold. As more energy is required to mix and transport larger particles, the erosion threshold of silt #8 is higher than that of silt #9.

The physical mechanism that explains the difference in measured and observed erosion threshold above are not accounted for in equation 5.13. Nonetheless, measured and computed (equation 5.14) τ_{cr} are shown in Figure 5-10 for silt #8 and silt #9 as function of the solid content. For both beds the range of measured τ_{cr} is small and compares well with computed τ_{cr} for γ -values in the range between 1.0 and 1.6 for $\phi_s < 0.6$. The results for the mechanically compacted sediment bed fall outside this range. The comparison shows that equation 5.13 can be used as a practical approach.

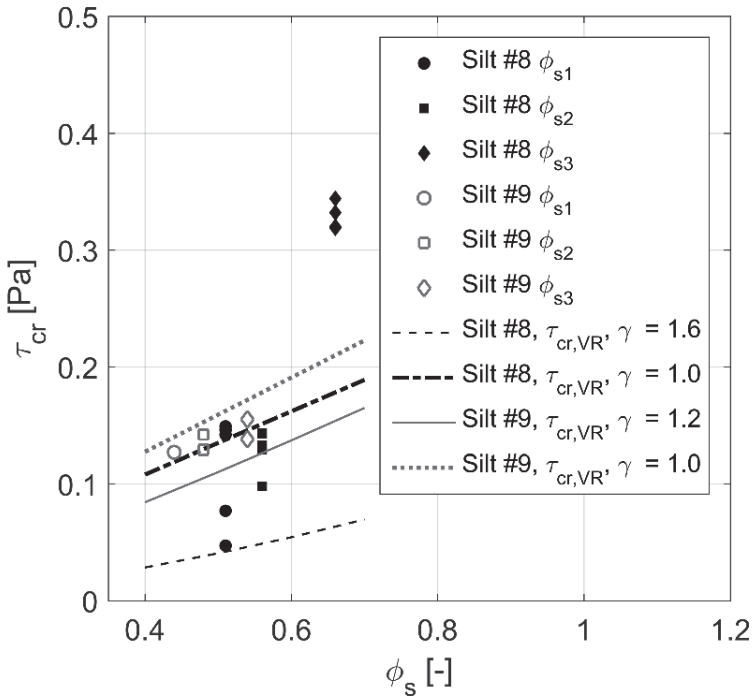

Figure 5-10 Comparison of measured (markers) and computed (lines following equation 2.15) τ_{cr} for varying γ-values.

5.5 Comparison erosion formulation with measurements

The derived surface erosion formulation has been compared to the measured erosion rates. The permeability is calculated with the Kozeny Carman equation using specific surface areas as in table 5.1, and by using interrelated density parameters ϕ_s, ρ_s and e (ϕ_s is measured directly). Typical values for the drained shear strength s_d yield 0 Pa for sand, 2 to 10 Pa for loosely – densely packed silt, and from 0 to 25 Pa for freshly deposited to heavily consolidated clays (Schofield and Wroth (1968b) and Terzaghi and Peck (1967)). Here, the undrained shear strength s_u is estimated from the vertical effective stress, assuming the thickness of the eroding layer equals $5d_{50}$, and a simple relation with the vertical effective stress $s_u = 0.5\sigma_{zz}^{sk}$. The uncertainties in *i*) the thickness of the eroding layer and *ii*) the relation between the shear strength and the effective stress can be included in the calibration parameter α, which was here set to 1.0.

The measured erosion rates are shown in Figure 5-11, where the computed range of erosion rates is indicated by shading. The upper limit of the computed erosion rates is defined by the minimum measured τ_{cr} and a maximum calculated M_s value, and vice versa for the lower limit. Subsequently, for the maximum M_s value, the solid content corresponding to the measured loosest packing is used, and vice versa. The computed erosion rates are in the range of the measured data although the spread is large. However, for the mechanically compacted beds

most values fall outside the lower limit. It is postulated that the densities of these beds are unnaturally high, and their mechanical behaviour is possibly affected by interparticle locking. The dotted line in Figure 5-11a shows the result for $\alpha = 0.3$. With this setting, all measured data falls within the range of the erosion model.

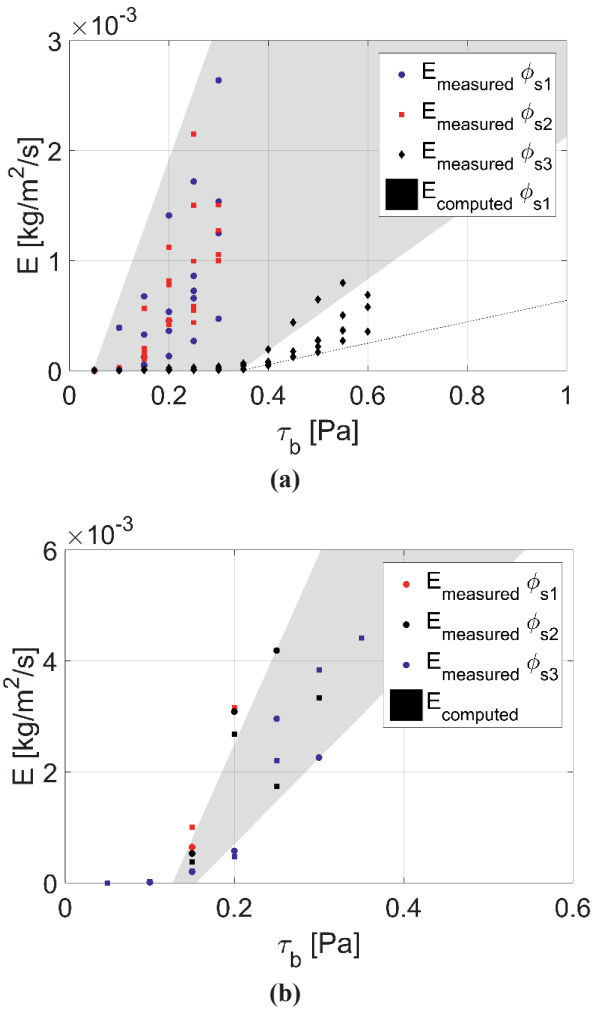

Figure 5-11 Computed (shaded) versus measured (marking) erosion rates for silt #8 (a) and silt #9 (b). The dotted line in figure (a) shows the result for $\alpha = 0.3$.

In addition to the evaluation above, Equation 5.10 was tested on the comprehensive dataset of erosion rates as measured by Roberts et al. (1998), which was obtained with Sedflume experiments. Results of latter comparison are not shown but will be briefly summarized. Amongst others, a fine granular sediment mixture with a d_{50} of 15 µm and a fine sand mixtures with a d_{50} of 75 µm were tested by Roberts et al. (1998). The solid fractions and the particle size distributions of the compared samples were known. The accuracy of the measured erosion

rates is unknown. Another unknown parameter of the silts used in the Sedflume experiments is the critical bed shear stress and shear strength. Nonetheless, the comparison of measured and computed (equation 5.10 using $\alpha = 1.0$) erosion rates have led to the following conclusions:

- The computed erosion rate is generally one order of magnitude lower than the measured erosion rates;
- The erosion formula gives better results with increasing solid content and for smaller bed shear stresses.

Overall, the proposed surface erosion formulation for silt (equation 5.10) appears to compare reasonably well with experimental data. An additional comparison with data from literature (Roberts et al., 1998) shows that the performance becomes worse with decreasing bed densities. This may suggest that apparent cohesion, which are more profound in low permeability soils (Randolph and House, 2001), is not fully accounted for. The experimental results provide too little detailed data for a further analysis. Nonetheless, it appears to be justified to apply the soil mechanical approach for erosion behaviour to silt beds.

5.6 Discussion and Conclusions

A new surface erosion formulation for silt (equation 5.10) has been proposed, based on the assumption that the permeability governs the pore-water flow. The formulation is based on the Gibson consolidation equation and has been derived in analogy to the erosion formulation for cohesive sediment, as proposed by Winterwerp et al. (2012). Therefore, the Gibson equation is simplified by neglecting term 3. It is thereby assumed that silt particles are non-swelling. The silt bed however may increase in volume due to shear-dilatancy as a response to hydrodynamic load conditions. Underpressures that then occur in the soil result in undrained conditions. These are dissipated by the inflow of pore-water.

The formula expresses the erosion rate as a function of bed's permeability, solid content, erosion threshold and undrained shear strength. The permeability of the bed can be computed using the Kozeny Carman equation, provided that the grain size distribution and bed density are known. As a practical approach, the erosion threshold can be obtained using the Van Rijn (2007) formulation.

The erosion formulation is tested against erosion rates measured with a Gust Microcosm. In most of the experiments, computed and measured erosion rates agree reasonably well. An additional comparison with the erosion data obtained by Roberts et al. (1998) shows less agreement, although trends are correctly reproduced. Therefore, it is recommended to test the formulation to a larger range of undrained conditions. In addition, the undrained shear strength over a range of densities of the tested beds is required for further validation. Valuable data and information can be obtained by extending the timescale and range of the loading in the erosion experiments, preferably in combination with pore-water measurements in the bed, which should aim at measuring the build-up and dissipation of underpressures.

Chapter 6

Sediment behaviour in silt-rich systems

6 Sediment behaviour in silt-rich systems[4]

Chapters 3-5 have examined the settling, deposition, compaction, and erosion behaviour of silty sediment mixtures under laboratory conditions. This chapter investigates the behaviour of silt-rich sediment mixtures in the real world, exemplified by the Yangtze River and Yellow River in China. The aim of this chapter is therefore to obtain more knowledge on the settling, deposition, compaction and erosion behaviour of sediment in silt-rich systems. For this purpose sediment samples were collected in both systems and analysed in laboratories in a similar way as the silty sediment mixtures described in earlier chapters.

6.1 Introduction to study area and fieldwork

6.1.1 General

Silt is the most abundant sediment type in China's main rivers; the Yangtze River and the Yellow River. Knowledge on the settling, deposition, compaction and erosion of silt is therefore essential for understanding and quantifying the morphodynamic behaviour of these rivers. Most of the silt in the Yellow River originates from the central China loess plateau (Figure 6-1), which contributes the most to the sediment transported by the Yellow River. The distributions of various clay minerals in both rivers show strong resemblance, which can be attributed to the source of the rivers; the Tibetan plateau in Western China.

Fieldwork was carried out in two silt-rich environments; the Yangtze River Estuary and in the Lower Yellow River (Figure 6-1). In both systems, 30-cm-long sediment cores were taken to determine *in-situ* solid contents and particle size distributions (PSD). In the Yangtze Estuary, additional surface sediment samples (upper 3 cm) were taken and one bulk sample was taken from the navigation channel (sample O). Bulk samples were taken to study hindered settling, deposition, compaction and erosion behaviour under laboratory conditions. In addition, water is collected from the bulk sample locations to perform the experiments under natural conditions. Laboratory sedimentation experiments have been carried out at the State Key Laboratory of Estuarine and Coastal Research (SKLEC), East China Normal University (ECNU) in Shanghai. Erosion experiments have been carried out at the Department of Ocean Engineering of the Zhejiang University in Hangzhou.

6.1.2 Study area

Yangtze River Estuary

The Yangtze Estuary is shaped by fluvial deposits from the 6418 km long Yangtze River and by tides, resulting in a typical funnel-shaped estuary. The most important morphological features of the Yangtze Estuary are extensive intertidal flats separated by large channels. Upon entering its estuary, the Yangtze River is divided by Chongming Island into the North Branch and the South Branch. Chongming Island is the largest island in this estuary covering approximately 1,600 km^2. On the East of this island, ecologically important wetlands can be found with an area of about 326 km^2. These wetlands consist of an unvegetated tidal flat and a

[4] Parts of this chapter are based on Te Slaa, S., He, Q., van Maren, D. S., & Winterwerp, J. C. (2013). Sedimentation processes in silt-rich sediment systems. *Ocean Dynamics*, *63*(4), 399-421.

salt marsh and are the origin of all Yangtze Estuary sediment samples (Figure 6-1). For simplicity, reference is made to the sediment from this location as Yangtze Estuary sediment.

Lower Yellow River

The Yellow River is characterized by extremely high sediment loads and deposition rates, and rapid channel migration (Wu et al., 2005). This rapid morphological development is attributed to the high loads of dominantly silty sediment. Samples were taken in the braided reach of the Yellow River and its main tributary (the Weihe River, just upstream of its confluence with the Yellow River, see panel 1 in Figure 6-1).

6.1.3 Fieldwork and processing

Fieldwork is carried out in late September 2009, early November 2010, late April 2011 and late September 2011 in the Yangtze Estuary, and in April 2011 in the Lower Yellow River. In the Lower Yellow River, mini-cores and bulk samples are sampled near Huayuankou (unvegetated floodplain; samples J and K) and from the Weihe River (unvegetated river bank; sample H), close to its confluence with the Yellow River, see panel 1 in Figure 6-1. On overview of sampling methods and times of sampling is shown in Table 6-1. Sampling locations are shown in panels 2, 3 and 4 of Figure 6-1.

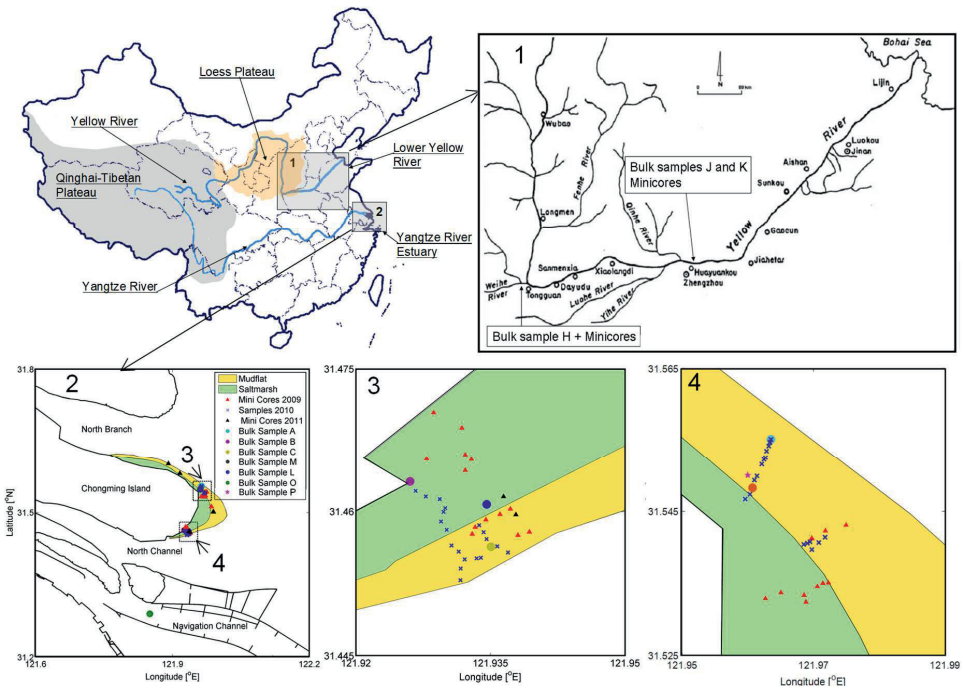

Figure 6-1 The Yangtze River and the Yellow River in China. The Lower Yellow River (1) and the Yangtze River Estuary (2) are sites for fieldwork and sediment sampling in present study. Sampling locations of minicores, surface and bulk sediment on Chongming Island are indicated in (2, 3 and 4). Yellow River sampling locations for minicores and bulk samples H, J and K are indicated in (1).

Table 6-1 Timetable of fieldwork activities in the Yangtze River Estuary and the Lower Yellow River.

Location	Sept 2009	Nov 2010	April 2011	Sept 2011
Yangtze Estuary	Minicores	Surface samples Bulk samples A, B and C	Minicores Bulk samples L, M and O	Bulk Sample P
Yellow River	-	-	Minicores Bulk samples H, J and K	-

Mini-cores are taken by using 30-cm-long PVC pipes with an inner diameter of 36 mm and sharpened edges at the intruding side. A plunger (from a 100 ml syringe) of equal diameter fits inside the PVC pipe. To reduce compaction of the sediment during extraction, the plunger was held at the sediment surface while the PVC pipe was pushed into the sediment. This method has been applied previously by Montserrat et al. (2009). After sampling, the cores were frozen. The time between sampling and freezing varied between 5 to 48 hours. Next, the cores were sliced into intervals ranging from 2 to 7 cm. These intervals were analysed on solid content and PSD. Surface sediment samples (upper 3 cm) are only analysed on PSD. Bulk sediment samples are taken in combination with water samples, to be used in the laboratory experiments; bulk samples remained constantly saturated.

PSD analysis of surface samples and mini-cores is done by making use of laser diffraction (LS-100 particle size analyser). All samples are dispersed chemically by treatment with a sodium-hexametaphosphate solution, in combination with ultrasonic dispersion.

6.1.4 In-situ conditions and spatial segregation

Yangtze Estuary sediment shows a variety of sediment compositions as a result of spatial segregation (Figure 6-2). According to the classification by Van Ledden et al. (2004), these sediments can be classified as cohesive silt, non-cohesive silt and non-cohesive mixed sand-silt (areas V, VI and III in Figure 2.1 respectively). Chongming Island tidal flat sediment is found to be mainly silt dominated, with the south-eastern tidal flat governed by non-cohesive silt and non-cohesive mixed sand-silt, whereas the north-eastern tidal flat is silt-dominated. The solid content isolines in Figure 6-2 indicate the boundaries of sand or silt dominated network structures for different solid contents. The minimum solid contents of sand for a sand-dominated network structure appears to be 0.5 to 0.6 and is set at 0.5. Similarly, the minimum solid content of silt for a silt-dominated network structure appears to be 0.5 to 0.6 and is set at 0.5 (Van Ledden et al., 2004).

The *in-situ* solid contents of the upper 30 cm of Yangtze Estuary sediment generally varies between 0.2 and 0.6 and is especially low for $\psi_{cl} > 10\%$. Below this threshold, *in-situ* solid contents are approximately 10% smaller than the solid content isolines in the silt-dominated area, whereas above this threshold *in-situ* solid contents are up 50 – 60% smaller. Clay/silt ratios of approximately 0.125 are observed for $\psi_{sa} > 5\%$, whereas for $\psi_{sa} < 5\%$ clay/silt ratios vary between 0.38 and 0.1.

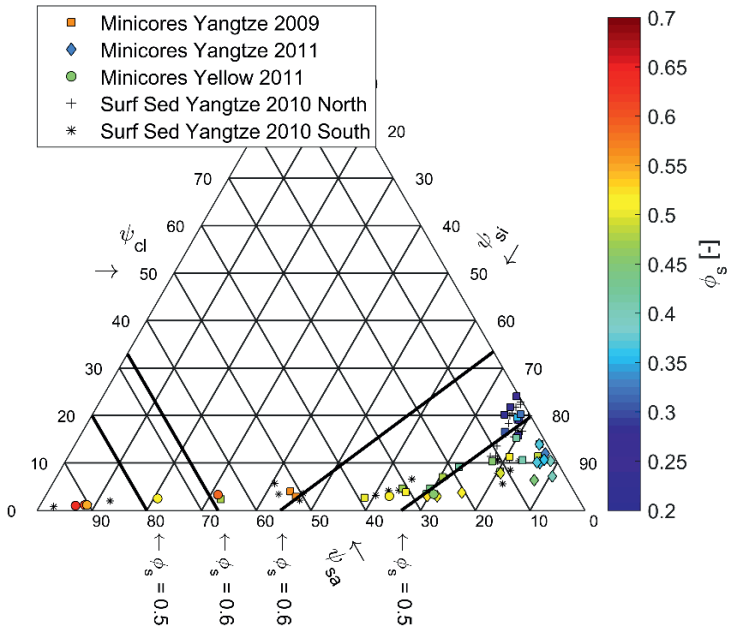

Figure 6-2 Ternary diagram of sand-silt-clay distributions in Yangtze Estuary and Yellow River 2009 and 2011 minicores in combination with measured in-situ solid content and Yangtze Estuary surface sediment samples ternary diagram. Solid content value indicated in colorbar.

Sediment from the Yellow River floodplains is found to be non-cohesive, varying between sand-dominated, silt-dominated and a mixture of these types (areas I, III and VI in Figure 2.1). Clay contents do not exceed 6%. *In-situ* solid contents deviate only 5% from the theoretical solid content (black solid lines in Figure 6-2) in the sand dominated area. Solid contents do not exceed 0.5. In general, a trend of increasing *in-situ* solid content is observed with increasing sand content, following the theoretical solid content. Solid contents above 0.55 are only rarely observed, which is expected as the maximum possible solid content is approximately 0.6.

6.2 Experimental procedures

6.2.1 Sedimentation experiments

Measurement principles

Consolidation processes are usually studied using settling columns, primarily focusing on density development and excess pore-water pressure dissipation within the consolidating bed itself. For a detailed description of the used columns, the reader is referred to **Chapter 3**. In this chapter, 9 series of sedimentation experiments are carried out in columns labelled A, B, C,

L, M, O, H, J and K. Only during the last experiment per series, pore-water pressure was measured using pressure transducers. The measurement procedure of the pore-water pressures is explained in section 3.4.1. In previous studies (Been and Sills, 1981; Merckelbach, 2000) density profiles were measured by making use of X- or γ-radiation. A great advantage of these methods is that it is non-intrusive and measures a continuous vertical profile with a high accuracy (± 2 kg/m^3). However, the extensive safety measures required with respect to radiation hazards make this method increasingly difficult to apply. Therefore, the solid fractions are measured using electrical conductivity. The greatest advantage of this method is that it allows for continuous density measurements in time. Other advantages are the non-intrusiveness without the disadvantage of radiation hazards. A disadvantage is the large influence of temperature fluctuations, which needs to be compensated using continuous temperature measurements.

Accuracy density measurements

Densities are expressed in terms of the solid content ϕ_s. In the settling columns, the solid content is continuously measured with 9 sets of conductivity probes, placed equidistantly over the vertical of the column. For all probes, the root mean square error (RMSE) is computed during the calibration, of which the procedure is exemplified for column L (Figure 6-3). Calibration is carried out for combinations of solid content and temperature. In a specially designed calibration beaker samples are prepared of which the output voltage of the CCM is measured for different temperatures, the latter one is increased by using an immersion heater. The measurement error of each probe system (temperature, probe distance, wiring) is defined as the root mean square error (RMSE, σ_ϵ^2) of measured (M) and observed solid content (O) for each temperature-solid content combination (i). In addition, the RMSE was determined for each individual solid content, for which a characteristic (for all columns) result of column L is shown in Figure 6-3. The RMSE (σ_ϵ^2) is defined as:

$$\sigma_\varepsilon^2 = \sqrt{\frac{\sum (M_i - O_i)^2}{n}} \qquad 6.1$$

Since the RMSE varies only little over the range of observed ϕ_s, the accuracy of each probe is defined as the overall RMSE of the calibration. For all probes in each column, the accuracy in ϕ_s is found to be below 0.01, corresponding with a mean error in concentration smaller than ±26.5 kg/m^3. Note that the accuracy is in line with the accuracy found for the solid content measurements in **Chapters 3, 4 and 5**.

Due to an anticipated different conductivity per sediment composition, calibrations were carried out with the sandiest and the most clayey composites. Surprisingly, no measurable difference in electrical conductivity between these extreme sediment composites is found. The variation in clay content of approximately 8% is apparently not influential enough to result in significant changes in conductivity in present experiments. The calibration and the experiments are both carried out with water from the sediment sampling location.

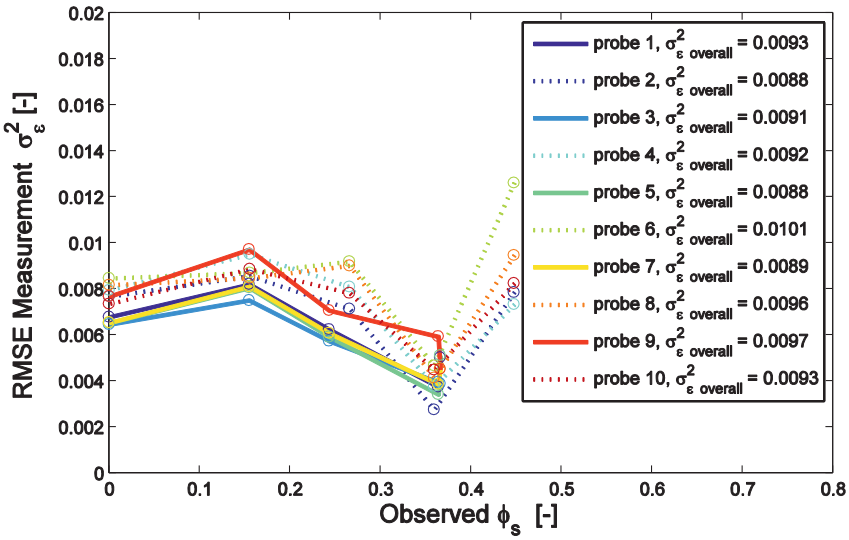

Figure 6-3 Calibration errors for all probes in column L. Overall RMSE's for each probe are depicted in the legend.

Method and program sedimentation experiments

A total of nine bulk samples are collected in the field; six from the Yangtze River Estuary and three from the Yellow River floodplains (Figure 6-1). The Yangtze River bulk samples are labelled A, B, C, L, M and O and the Yellow River bulk samples are labelled H, J and K (corresponding to the label of the settling column). With each of these bulk samples a series of sedimentation experiments is carried out in different settling columns, one column for each sample, labelled with a letter referring to the bulk sample. All columns are equally equipped with measurement devices. In all experimental series, the initial concentration varies per experiment. During sedimentation, vertical density and vertical pore-water pressure profiles are measured. In addition, visible interfaces are recorded manually. As water from the sediment sampling location is used, the experiments with Yellow River sedimentation are carried out with fresh water and the Yangtze River sedimentation experiments are carried out with brackish / saline water. Salinity values are not recorded.

All nine series of sedimentation experiments are carried out following the same protocol. For each experimental series a container was prepared with sufficient sediment and water to fill a column with initial concentrations of up to 800 kg/m^3. Clear water from a corresponding container was introduced into the columns first. With this clear water, a reference concentration measurement was carried out, and the tubes leading to the pressure transducer were filled with water to prevent air-entrapment. Next, the sediment within the container was homogenously mixed for 5 minutes after which a volume of the sediment-water mixtures from the container was added to the column. Now, the sediment-water mixture within the column was mixed gently with a porous pounder for 5 minutes after which the mixture was left to settle. For each

following test with higher initial concentration in the same series, the container was mixed up again and a new volume from the container was added to the column. The initial concentrations were obtained by averaging the measured concentration during the first 10 seconds of each test. During the experimental series the container and the columns are sealed to prevent evaporation of the pore water. Calibration of the conductivity probes is carried out after each experimental series. This allows verification whether any drift of the probes had occurred with respect to the initial clear water concentration measurement.

Table 6-2 shows the initial concentrations used in all series. It can be seen that (for most columns) the smallest initial concentrations are in the same order of magnitude as the accuracy of the conductivity probes. Since settling velocities are relatively large at these concentrations, both the clear water conductivity and the conductivity during settling are only measured during a short time. The offset between the measured clear water conductivity and the calibrated clear water conductivity was used to improve the measurements at the low concentrations. Only during the last experiment per series, pore-water pressures are measured. After the last experiment, sediment samples are taken along the columns. This is done at the locations of the conductivity probes.

Due to blurring of the conductivity signal during measurements in columns M and O, only visual observations of the sediment-water interface are available. The reasons for the failure of these conductivity measurements can be multiple, but could not be further investigated.

Table 6-2 Initial concentration in experimental series in kg/m^3. T1 – T12 represents the number of experiments per series. Results of bold marked initial concentrations are shown in Figures 6-7 to 6-9.

Settling	Test number in series											
Column	1	2	3	4	5	6	7	8	9	10	11	12
A Yangtze	-	-	82	175	155	224	281	314	252	382	426	**396**
B Yangtze	41	44	144	154	209	218	213	**401**	-	-	-	-
C Yangtze	66	160	241	290	**367**	-	-	-	-	-	-	-
L Yangtze	545	717	705	701	720	**707**	-	-	-	-	-	-
M Yangtze	40	56	75	104	**343**	-	-	-	-	-	-	-
O Yangtze	24	44	62	78	**211**	-	-	-	-	-	-	-
H Yellow	76	278	205	298	334	414	**667**	-	-	-	-	-
J Yellow	11	74	131	249	310	**488**	-	-	-	-	-	-
K Yellow	42	143	119	135	**364**	-	-	-	-	-	-	-

6.2.2 Erosion experiments

Experimental setup

For the erosion experiment the annular flume of the Department of Ocean Engineering of Zhejiang University (Hangzhou) has been used. An annular flume is a ring shaped flume with two rotating elements that move independently; these are the top-lid and the combined bottom-side walls of the flume. When rotating these elements in opposite direction a tangential flow, which exerts a quasi-uniform bed shear stress, is generated. Secondary currents in annular flumes are kept to a minimum by moving the elements at optimum rotation velocities (Booij, 1994). The top-lid, the bottom of the flume and the side-walls are made of transparent plastic, which typically has a low roughness, and therefore these elements are considered as hydraulically smooth. The flume (Figure 6-4) has a rectangular cross-section with a width of 13.7 cm. The mean diameter of the flume is 73.7 cm. The angular velocity can be controlled over a range of 2 to 35 rpm for the top-lid, and of 3 to 20 rpm for the flume.

Figure 6-4 Annular flume of the Department of Ocean Engineering of the Zhejiang University in Hangzhou.

Flume calibration

The calibration of the annular flume of the Department of Ocean Engineer of Zhejiang University in Hangzhou, hereafter referred to as the Hangzhou flume, has been reported in Delft University of Technology (2012) . The calibration procedure and results are briefly addressed next. Booij (1994) provides a rotation velocity ratio between the top-lid and the flume for optimum flow conditions. In addition, operational relations which provide an estimation of the bottom shear stresses in annular flumes with varying geometry are provided.

Based on the work of Booij (1994) the following relation for the applied bed shear stress has been derived for a water depth of 14.0 cm for the Hangzhou flume:

$$\tau_b = 0.1\left(\frac{1.64\omega_f + 3.89}{c_t}\right)^2 \qquad 6.2$$

Where τ_b [Pa] is the bottom shear stress, ω_f [rad/s] is the rotational speed of the top lid and c_t [unit $c_t^2 = \text{rad}^2\text{m/kg}$] is a constant value (for the annular flume of Delft University of Technology, Booij found $c_t \approx 25$). Note that the bed shear stress following equation 6.2 is nonzero at zero rotation velocity. To check whether the estimation for the bottom shear stress in equation 6.2 holds for the Hangzhou flume, experiments with beds made of a number of specific sand mixtures were carried out. These sand mixtures were obtained from sieved river sand (source unknown). For each of the sand mixtures a layer of sand of known particle size was placed in the flume and the bed shear stress was increased in steps until the onset of particle movement. The following procedure was repeated for each sand mixture: after placing a 0.5 cm thick sand bed and filling the flume with water up to a level of 14.0 cm above the bed, ω_f increased in steps until onset of movement occurred. The observation of the formation of ripples was applied as the criteria for determining the onset of movement. The critical shear stress for every sand mixture was computed following Shields - Van Rijn (1984) and is shown in Table 6-3. Equation 6.2 has been fitted against the observed critical shear stresses and the rotational velocities of the flume corresponding to initiation of motion (Figure 6-5) by calibrating the c_t parameter. A small correction has been applied by fixing the function to the origin (zero bed shear stress at zero rotation velocity). As a result, the bed shear stress τ_b as function of the rotation velocity of the bottom of the flume ω_f can be written as:

$$\tau_b = 0.1\left(\frac{1.64\omega_f + 3.87}{8.43}\right)^2 - 0.018 \qquad 6.3$$

Table 6-3 Computed shear stresses, corresponding with the observation of the onset of movement.

Sand mixture	d_{50} [μm]	ω_f [rad/s]	τ_{cr} Shields-Van Rijn [Pa]
#1	290	4.91	0.15
#2	447	6.38	0.21
#3	646	7.36	0.32
#4	938	9.82	0.55
#5	1321	12.76	0.89

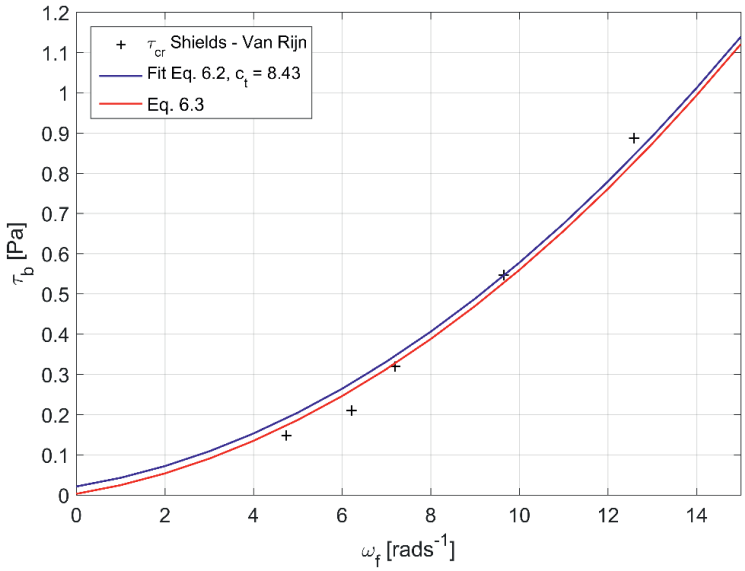

Figure 6-5 Fit of equation 6.2 to the results of the calibration tests (blue line) and correction for zero bed shear stress at zero rotation velocity (red line).

Bed preparation

The sediment used for the erosion experiments originates from the North Eastern mudflat of Chongming Island (sample P, Figure 6-1) and is sampled in late September 2011. Organic material (mainly shells) was removed from the sample by sieving. Next, the sediment was mixed twice for 30 minutes to obtain a homogeneous sample. After that it was poured in the flume preparing a so-called placed bed and the first erosion test started after one hour. Once the first test was finished, the sediment was removed from the flume, mixed twice again, placed back in the flume and left at rest to consolidate for the next 4 days. After that, a second erosion test was performed.

Prior to both experiments a bed density profile is measured by means of a CCM-conductivity probe. Since a probe measurement is destructive, the density measurements are performed in separate cylinders. The beds in the cylinders are prepared in the exact same way as the beds in the flume. Two density profiles are measured per cylinder.

Concentration measurements and test program

The concentration in the flume was measured continuously by an OSLIM (optical measuring instrument that measures the concentration of suspended particles based on attenuation intensity of light passing through a measurement volume). For that, water was pumped from the flume through the OSLIM, and recirculated to the flume again. The OSLIM was calibrated with samples at different concentrations of the sediment in the flume. A single point concentration measurement is considered to be representative for the average concentration in

the entire water column. The outflows to the OSLIM in tests 1 and 2 are located at 6.00 cm and 5.65 cm above the bed, respectively. The difference in the level of the OSLIM outflow is caused by a variation in bed thickness. In addition to the OSLIM measurement, manual concentration measurements (using a conventional filtration set up) are performed every 30 to 60 minutes. For that purpose, samples of 50 ml are extracted from the same outflow as the OSLIM measurements without pausing the test. The concentration is obtained by filtering the extracted flume water with a 10 μm filter paper which is left to dry for 24 hours in an oven at 80 ^{o}C after which the dry mass is measured.

After bed preparation, the water level in the flume is increased to 14.0 cm above the bed. Bed disruption during the filling process was prevented by temporary placing a plastic foil over the bed. During the erosion experiments the bed shear stress is increased in steps, starting at 0.023 Pa and going up to 1.19 Pa in 10 (unequal) steps. The duration of each step is 60 minutes but was shortened to 30 minutes when the measured concentration remained 0 during the first minutes of the intervals. Table 6-4 shows the programs for the two tests.

Table 6-4 Test program test 1 and test 2

	Test 1		Test 2	
Step	**Duration [min]**	**Bed shear stress Equation 6.3 [Pa]**	**Duration [min]**	**Bed shear stress Equation 6.3 [Pa]**
1	60	0.01	30	0.02
2	60	0.02	30	0.05
3	60	0.05	30	0.09
4	60	0.09	30	0.18
5	30	0.18	30	0.27
6	30	0.41	60	0.41
7	60	0.58	60	0.58
8	60	0.72	60	0.72
9	60	0.91	60	0.91
10	60	1.19	60	1.19

6.3 Results and analysis

Sediment composition sedimentation experiments

Before analysing the results, the measurements and analysis of one settling column experiment are described in detail (Figure 6-6: experiment A10). In the majority of the experiments (including A10, Figure 6-6) segregation is observed visually, resulting in two interfaces. The upper interface represents the top of a settling mud layer. A clear transition between the mud and the overlying clear water indicates that all particles at the interface settle at a single velocity. Sediment in this layer is composed out of clay and silt as revealed by particle size analysis, and the observation of drainage channels (resulting from non-homogeneously distributed fluid flow in the horizontal plane, characteristic for clay dominated mixtures (Winterwerp and Van Kesteren, 2004)).

Table 6-5 Sand, silt and clay contents, and d_{50}'s of material used in sedimentation columns.

Column, River	Clay [%]	Silt [%]	Sand [%]	d_{50} [µm]
A **Yangtze**	11	77	12	25
B **Yangtze**	9	86	5	28
C **Yangtze**	8	62	30	33
L **Yangtze**	3	63	34	49
M **Yangtze**	10	85	5	14
O **Yangtze**	12	86	2	10
H **Yellow**	6	20	74	114
J **Yellow**	7	53	40	53
K **Yellow**	15	78	7	14

Initially, the upper interface settles with a constant velocity until time t_3. Here, an contraction point in the settling curve is observed. From this point forward, the settling rate is reduced significantly indicating the transition from a hindered settling regime into consolidation or compaction (depending on the sediment composition) beyond time t_3. The second, internal interface marks the transition between the settling and/or consolidating mud layer and the underlying granular layer. This granular layer builds up between t_0 and t_2, indicating that the majority of the granular material settles within this timeframe and hence segregates from the clay-water mixture.

Solid content isolines (isolutes) are derived from the solid content timeseries. Initially the isolutes in the lower 27 cm are straight and are directed upwards (until in-between t_1 and t_2) and those in the overlying mixture are straight and directed downwards (until t_1). After t_2 the isolutes in the lower 27 cm are horizontal. The gradient of the isolutes provides a settling velocity within the settling sediment-water mixture (internal settling interface) – see **Chapter 3**. Between t_1 and t_2, the isolutes converge, indicating an increasing vertical solid content gradient, and hence a reduction in settling velocity. After t_2 the isolutes in the lower 27 cm are horizontal, marking complete sediment deposition.

In addition to interface observations and solid content measurements, a pressure transducer measured pore-water pressures to determine excess pore-water pressure dissipation. At the end of each experiment (t_{end}), sediment was collected from the settling column at the locations of conductivity probes (which are removable) for particle size analysis.

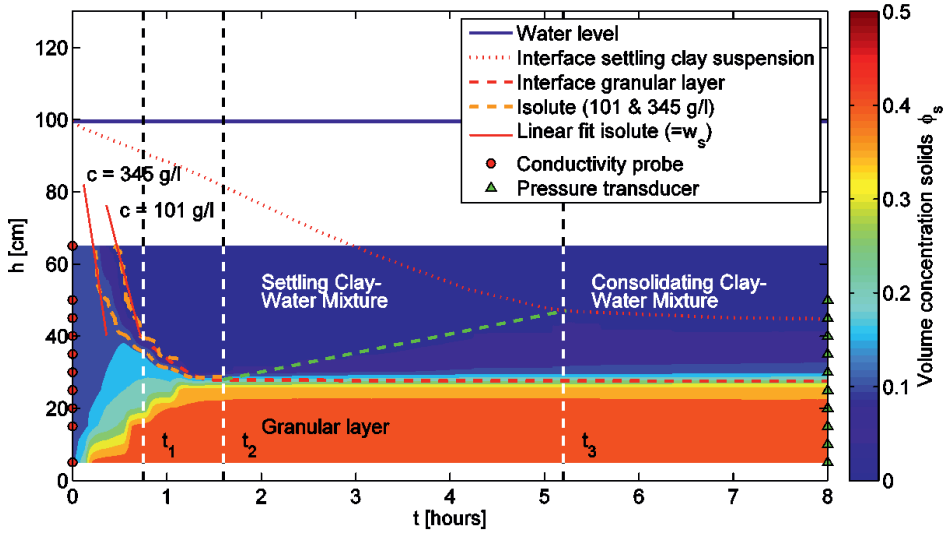

Figure 6-6 Measurement results for the vertical volume concentration profile over time in experiment A10. Visual interface observations are indicated by red dotted lines. Derived isolutes between t_0 and t_1 are given for c = 101 and 345 g/l. t_2 represents the moment where all granular material is settled. t_3 represents the inflection point. Locations of conductivity probes and pressure transducers are indicated by red dots and green triangles, respectively. The green dashed line indicates the ascending internal interface of deposited flocculated material.

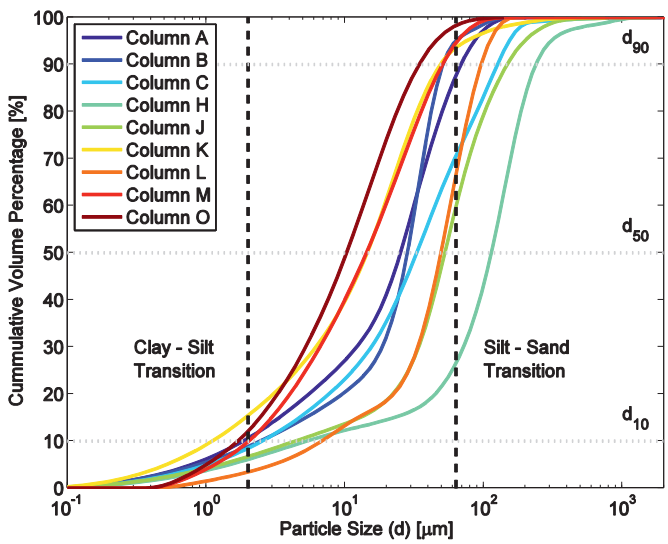

Figure 6-7 Grain size distribution of sediment used in settling column experiments. Black dotted lines indicate clay-silt (2 µm) and silt-sand (63 µm) transitions.

Summarizing, the experiments consist of a phase with rapid settling of granular material, allowing computation of settling velocities ($t_0 - t_1$), a phase with settling clays and hindered settling of granular material ($t_1 - t_2$), a phase with settling clays overlying a granular bed ($t_2 - t_3$), whereas the final stage is with a consolidating clay-water mixture ($t_3 - t_{end}$). These measurements allow quantitative analyses of segregation mechanisms, hindered settling velocities and solid fractions of multiple sediment fractions, of which results are presented in the next subsections.

6.3.1 Segregation

Vertical profiles of sediment composition (percentages of sand, silt and clay fractions), d_{50} and solid content at t_2, t_3 and t_{end}, of the tests with the highest initial concentration per column, are shown in Figures 6-8 to 6-10. The grain size properties result from direct sampling. In tests K5, M5 and O5 no granular layer is observed. Solid contents at t_2, t_3 and t_{end} are indicated with brownish colours. The top panel in Figure 6-8 is representative for Figure 6-6, but with different initial concentration (338 vs 396 kg/m^3 – see Table 6-2). Note the deviating x-axis in Figures C5 and H7. Next, the results for Yangtze Estuary and Yellow River sediment are discussed separately. It is assumed that Yangtze Estuary experiments are carried out in brackish / saline water and Yellow River experiments are carried in fresh water.

Yangtze River Estuary Sediment (Columns A, B, C, L, M and O)

The strongest segregation is observed in column C, which together with column L, contains the coarsest sediment of all Yangtze Estuary samples. In column L, segregation does not occur, which is attributed to the narrow PSD and high initial concentration. In columns A and B, the silt fraction settles from the overlying layer in which clay percentages are higher. In contrast to column C, columns A, B and L show less segregation within the granular layer. The granular layer in column A shows a more or less constant sand content, only slightly increasing toward the bottom. Hence the segregation in column A is limited, which can be attributed to the high clay content.

Sand is absent in all top layers of columns A, B, C and L indicating that sand and/or silt particles are not supported by a network structure in the settling phase. The clay/silt ratio in the overlying settling mixture is approximately 0.25 in all these columns whereas the average clay/silt ratio of the bulk sample is 0.14. A constant clay/silt ratio is not observed in the bed. Clay percentages generally decrease with depth, whereas sand and/or silt contents increase.

The density profiles in columns K (at t_3) and L have a sawtooth-like character which is probably caused by local accumulation of pore fluid pockets rather than by a lack of accuracy. This suggestion is supported by the measurements in column K, where the sawtooth-like character develops over time.

In columns M and O limited segregation occurred even though initial concentrations are quite low (343 and 211 kg/m^3) in comparison to columns A, B, C and L (367 to 707 kg/m^3). This is attributed to the relatively high clay percentages. Apparently, the initial concentrations are sufficiently high to reduce the settling velocity of silt and sand particles within the mixture.

Yellow River Sediment (Columns H, J and K)

Segregation behaviour in the columns containing Yellow River sediments is qualitatively comparable to that of the Yangtze Estuary sediments; larger particles settle faster, leaving a clay-dominated mixture to settle and consolidate on top of the deposited sand and/or silt dominated bed. Very low clay percentages in the lower 40 cm of Column H, in contrast to the upper 5 cm, show that segregation has occurred during the first phase of the test. The clay-dominated mixture overlying the granular layer is relatively thin due to the low clay content (6%; see Table 6-5). In column J, the clay content is also low, and vertically uniform in the granular layer. The sand content increases with depth and ϕ_s increases slightly with the sand content. Column K shows larger clay contents in the upper layers which results in a more pronounced vertical gradient in solid content. In the lower 20 cm of column K, segregation is the strongest.

The sedimentation experiments show that no segregation occurred in the columns with clay contents exceeding 10%. For the columns with clay contents below 10%, segregation occurred in columns B, C and J with initial concentrations of 367 kg/m^3, 401 kg/m^3 and 488 kg/m^3, respectively. Segregation did not occur in columns H and L with initial concentrations of 677 kg/m^3 and 707 kg/m^3, respectively. Based on these observations it is concluded that no segregation occurs at clay percentages exceeding 10 and that segregation is prevented at the higher (approximately > 600 kg/m^3) initial concentrations.

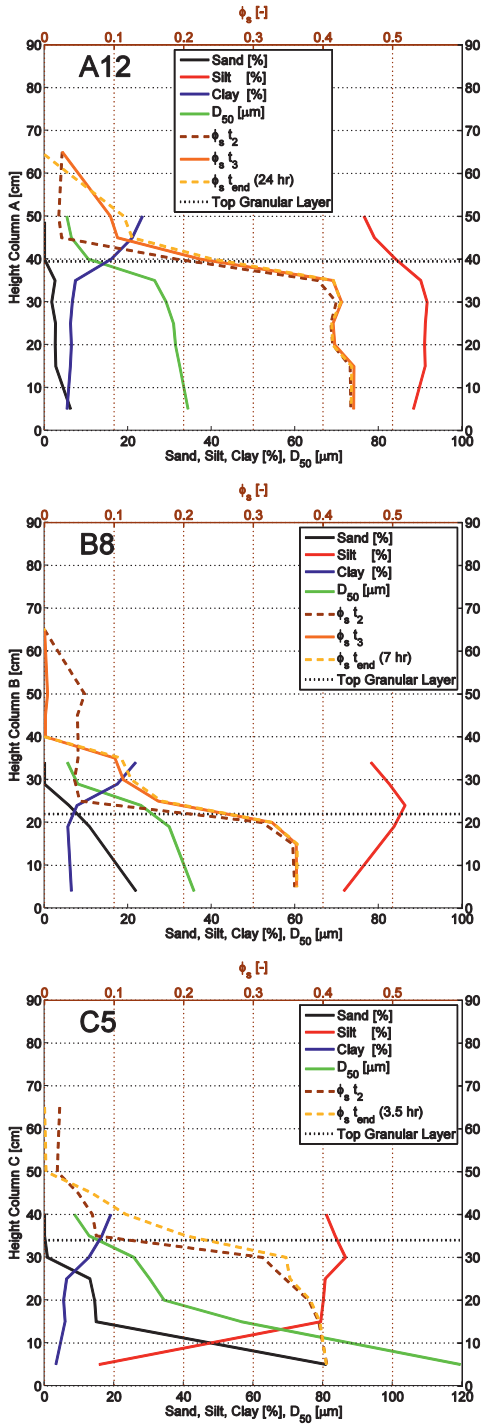

Figure 6-8 Results of Yangtze River experiments A12, B8 and C5 at end of test.

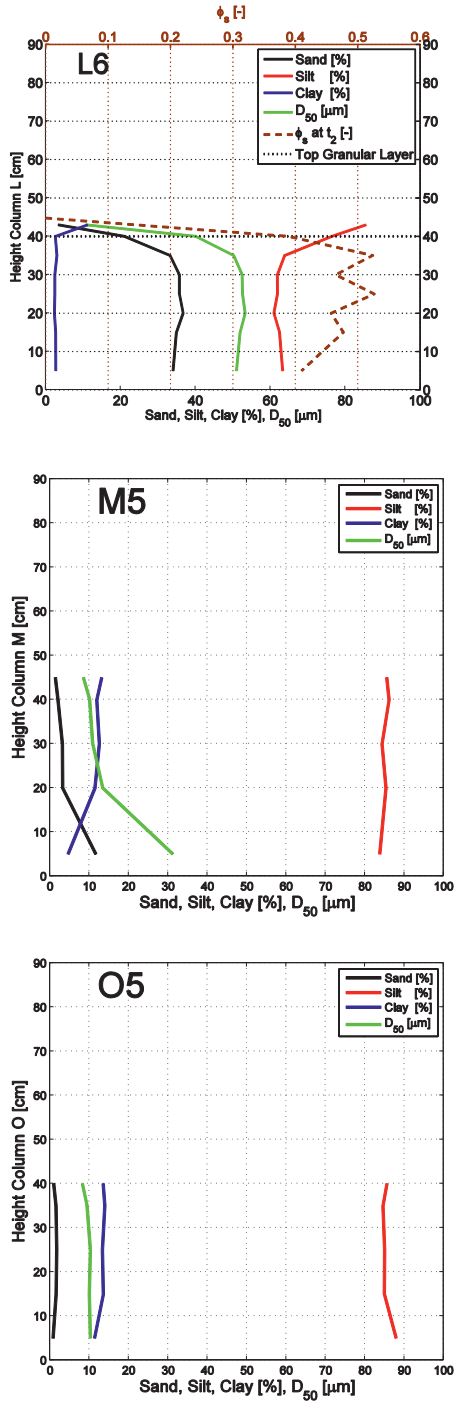

Figure 6-9 Results of Yangtze River experiments L6, M5 and O5 at end of test.

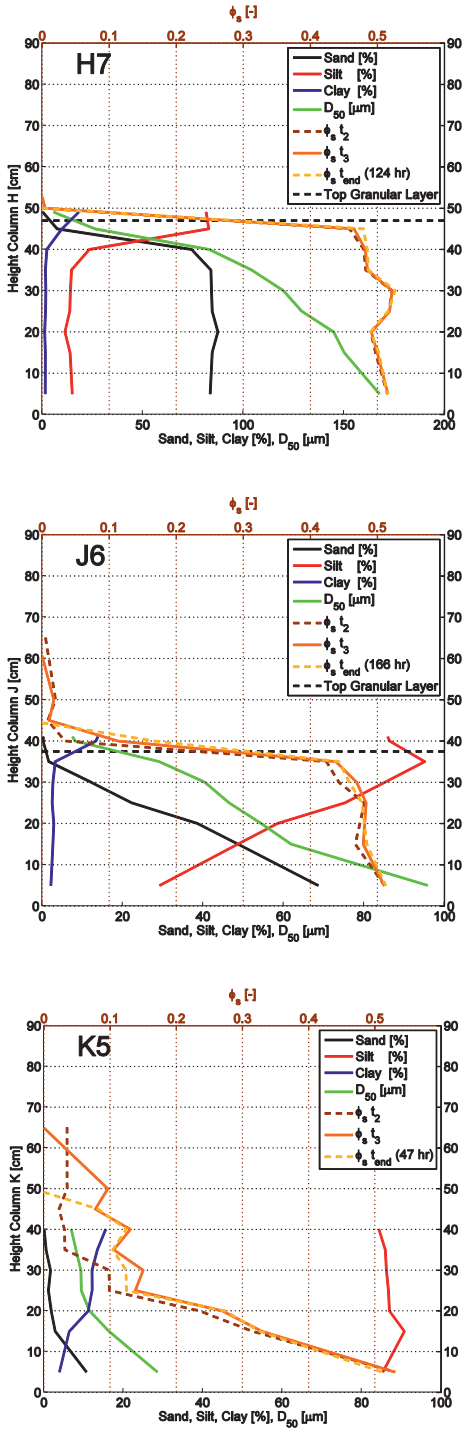

Figure 6-10 Results of Yellow River experiments H7, J6 and K5 at end of test.

6.3.2 Gelling concentration

The minimum solid content $\phi_{s,\min}$ of granular material corresponds to the loosest packing where a space-filling network has developed at which particles support each other. For cohesive material the minimum solid content is defined as the concentration at which a space filling network of flocs has developed, which is referred to as the gelling concentration c_{gel}. Generally, minimum solid contents for granular material are around 0.4, whereas gelling concentrations may be as low as 50 – 100 kg/m^3. In present experiments, both conditions are observed, often simultaneously. Between t_0 and t_2, granular material forms a network structure, whereas the overlying clay mixture forms a network structure between times t_0 and t_3.

Minimum solid content

The sediment composition and corresponding solid content of the beds, developed in all columns at the end of the sedimentation experiments, is shown in a ternary diagram (Figure 6-11). Sediment samples are taken at the levels of the conductivity probes. The solid content is now related to the sediment composition. Most of the sediment samples in the vertical profile of the columns are silt-dominated. The samples without sand (upper layers) have a relatively low solid content. The solid content increases with increasing sand content (up to $\Psi_{sa} \approx 40\%$); for higher sand contents, the solid content is 0.5 and independent of Ψ_{sa}. Such a clear correlation cannot be observed for the silt fraction. In the silt-dominated area ($\Psi_{si} > 67\%$), the solid content may be both high and low, depending on the fractions of the other two constituents. Sediment mixtures with the lowest solid content ($\phi_s < 0.3$) do not contain sand and are all located in the overlying consolidating sediment layer. These low solid contents appear to occur when the clay content exceeds 10%.

Gelling concentration

The gelling concentration of the overlying clay-water mixture can be determined by three methods:

1. By direct measurement of the gelling concentration in the settling column by a conductivity probe (results in Table 6-6);
2. On the basis of the mass balance of the clay-water mixture by taking the average concentration above and below the internal rising interface of the clay-dominated mixture. This interface is represented by the green dotted line in Figure 6-6 (results in Table 6-8) and;
3. Using settling velocity and concentration measurements.

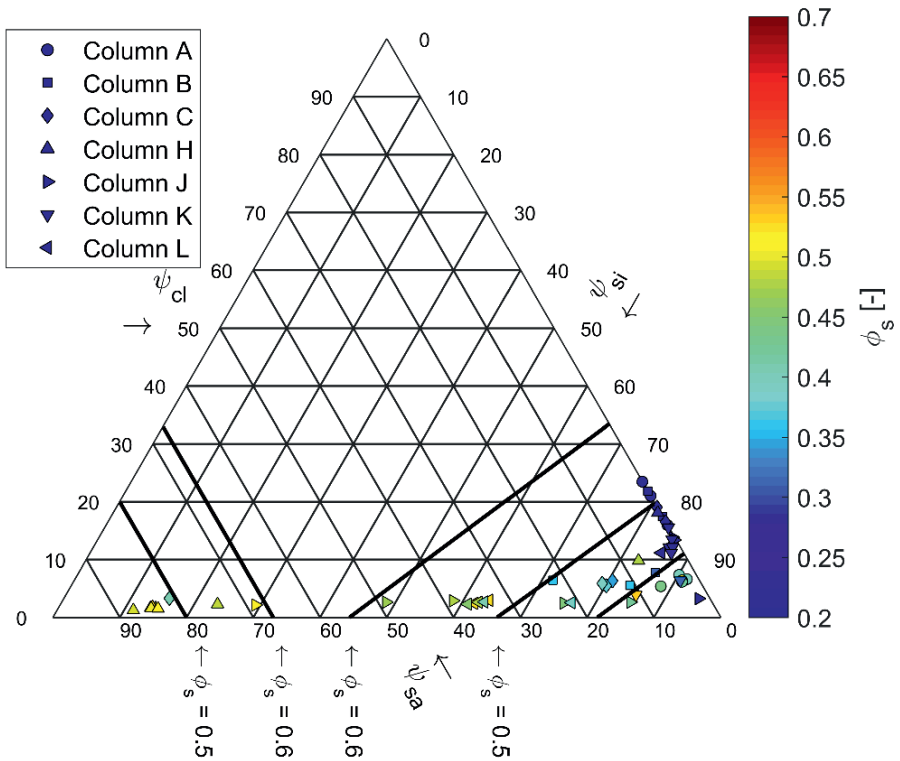

Figure 6-11 Ternary diagram of sand-silt and clay content combined with measured solid fraction at t_{end} in consolidation/compaction experiments A12, B8, C5, H7, J6, K5 and L6 at location of conductivity probes.

Above methods are described extensively by Dankers (2006), who argues that the second method overestimates the calculated gelling concentration in comparison with the first method. The second method can only be applied for non-granular sediment, which makes it suitable for columns M and O (Yangtze Estuary sediment only). The third method is discussed in section 6.3.3.

The concentration timeseries (method 1) during the sedimentation process allow for direct measurements of the gelling concentration of the overlying clay water-mixture. These timeseries are shown in Figure 6-12 for experiment A10. Initially, concentrations decrease along the upper 3 probes (1 to 3) and concentrations increase along the lower 4 probes (7 to 10) in the column as the granular material settles from the mixture first. The 3 probes (4 to 6) within the settling clay-water mixture measure a concentration increase first, after which the concentration reduces once the granular material has deposited below these probes. Zero concentration is measured when the sediment-water interface has lowered beyond the upper

probes and constant concentrations are measured upon bed formation. Next, the concentration within the settling clay-water mixture increases again, indicating the passing of the ascending internal interface of deposited flocculated material (green dashed line in Figure 6-6) along the probes. The inflection point in Figure 6-12 (blue dot) represents the point of contraction in Figure 4-2, and hence is an indication for the gelling concentration. The gelling concentration is thus directly measured when the ascending isolute passes a conductivity probe during the build-up process of the bed. After 5 hours, the concentration at probe 3 reduces again, indicating that the bed level of the consolidating clay-water mixture has lowered beyond the probe.

The gelling concentrations obtained by following method 1 are shown in Table 6-6 for the experiments in columns A, B, C, H, J and K. Since the thickness of the clay-dominated layers in the consolidation phase of the columns containing Yellow River sediments is small, only a few direct measurements of the gelling concentration are available.

Table 6-6 Gellingconcentrations in kg/m^3 resulting from direct concentration measurement.

Series	Ψ_{cl}	Test number in series									
		2	**3**	**4**	**5**	**6**	**7**	**8**	**10**	**11**	**12**
A Yangtze	11%	-	-	-	-	95	85	115	136	120	140
B Yangtze	9%	-	-	-	94	122	93*	-	-	-	-
C Yangtze	8%	71	80	127*	119	-	-	-	-	-	-
H Yellow	6%	-	-	-	74	45*	78	-	-	-	-
J Yellow	7%	-	-	-	90	101	-	-	-	-	-
K Yellow	15%	-	95	84	80#	-	-	-	-	-	-

***Clay suspension settled along interface during deposition of clay-water mixture. # Concentration in which segregation is prevented, measured in the settling phase (= minimal *cgel*). *Cgel* Yangtze River clay = 107 ± 22 kg/m^3. *Cgel* Yellow River clay = 81 ± 17 kg/m^3.**

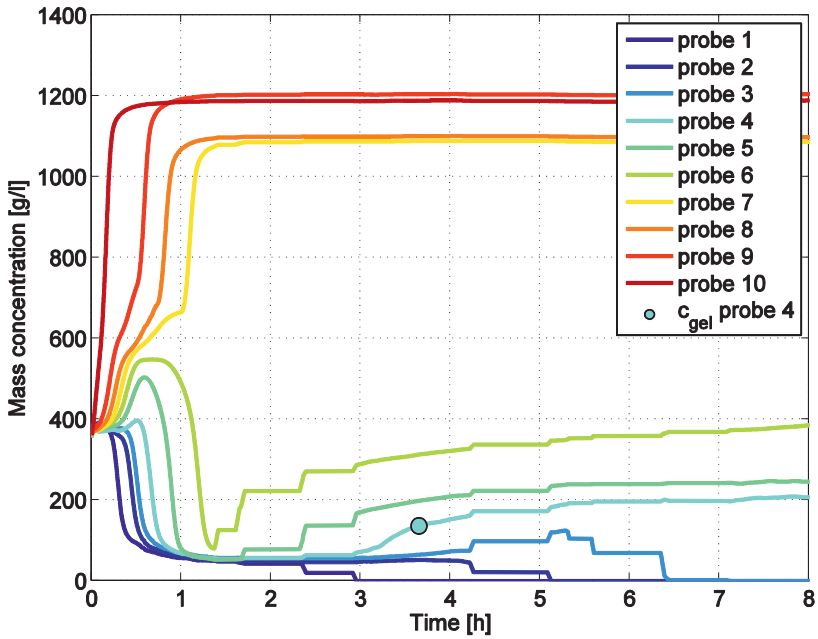

Figure 6-12 Concentration time series for all probes in experiment A10. Probe 1 is at 65 cm from the base of the settling column. Probe 4 is located within the settling and consolidating clay-water mixture and measures a c_{gel} of 136 g/l at t = 3.65 h. Discontinuities are the result of non-continuous measurement.

From the experiments, mean gelling concentrations of 107 ± 22 kg/m^3 and 136 ± 22 kg/m^3 are observed for Yangtze Estuary clay-water mixtures using the first and second method, respectively. For Yellow River clay, a gelling concentration of 81 ± 17 kg/m^3 is observed. These values are further discussed in section 6.4.

6.3.3 Settling velocity

Settling velocities of the granular and clay fractions are derived separately. The first time-derivative of the observed settling interface between t_0 and t_3 gives the effective settling velocity of the clay mixture, whereas the first time-derivatives of the isolutes between t_0 and t_1 (example in Figure 6-6), gives the settling velocities of the granular fractions.

Hindered settling of clay-water mixtures

Figure 6-13 shows the effective settling velocities w_s of the visually observed interface of the overlying clay-water mixture, as function of the measured mass concentration, for Yangtze Estuary sediment (upper panel) and Yellow River sediment (lower). The settling velocity decreases with increasing concentration, indicating hindered settling effects. The overlying sediment-water mixture is a clay-dominated mixture for which Dankers (2006) relates the settling velocities to sediment concentration through:

$$w_s = w_{s,0} \frac{\left(1-\phi_f\right)^m (1-\phi)}{1+2.5\phi_f} \tag{6.4}$$

Here, $w_{s,0}$ is the settling velocity of individual aggregates, $\phi_f = c / c_{gel}$ is the volumetric solid content relative to the minimum solid content of the bed, in which c is the mass concentration of a mud and c_{gel} is the gelling concentration. Equation 6.4 is valid in the hindered settling regime of mono-dispersed particles, and can therefore be applied when sand and silt particles have settled (i.e. after t_2). In the present experiments, this always holds for the upper interface. Fitting of $w_{s,0}$ and c_{gel} in equation 6.4 (Figure 6-13) with measured w_s and ϕ, using m = 2, result in gelling concentrations of 240 and 133 kg/m^3 for the Yangtze Estuary and Yellow River clay-water mixture with corresponding values for $w_{s,0}$ of 0.26 and 0.40 mm/s, respectively.

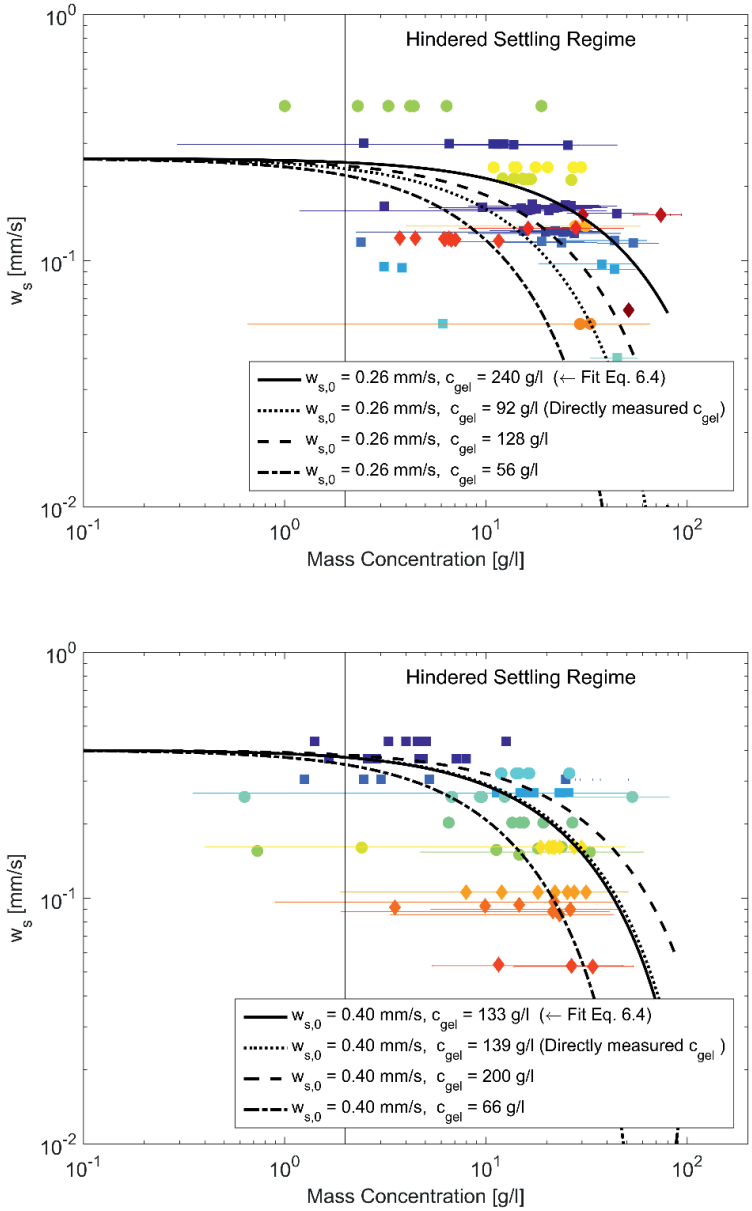

Figure 6-13 Observed still water settling velocities of flocculated material as function of the measured sediment concentration in Yangtze Estuary columns (upper) and Yellow River columns (lower). Varying colours represent different test series, whereas shape variations represent different columns. Horizontal lines represent error bars.

Hindered settling of granular material

Effective settling velocities are derived from the slopes of the isolutes (following the method shown in Figure 6-6) for Yangtze Estuary and Yellow River sediment, see upper and lower panels in Figure 6-14, respectively. Connected points that form a line show the effective settling velocities within a single experiment, thereby representing a range of settling interfaces for various particle sizes (explanation in Figure 3-3). The initial concentrations are indicated per experiment. The far right point of each line represents the effective settling velocity measured first in a single experiment. Later, effective settling velocities either reduce significantly ($c_0 < 200$ to 250 kg/m^3) or increase moderately ($c_0 > 250$ kg/m^3). A transition from positive to negative slope between lines of connected points in the w_s-c plane is observed at concentrations between 200 to 250 kg/m^3 in columns A, B, J and K. In columns C and H, no clear transition is observed.

The settling regime can be derived from the slope of the connected points. A positive slope indicates descending diverging isolutes in the h-t plane of the corresponding experiment (the example in Figure 6-6 shows diverging isolutes). The effective settling velocities are governed by particle size (segregation). The lower initial concentrations show the largest settling velocities, as well as the largest range in settling velocities. The highest settling velocities occur early in the sedimentation experiment (Figure 6-6), which is attributed to segregation; the largest particles settle with the highest velocities. Within each of these experiments, segregation results in a decreasing settling velocity with decreasing sediment concentration as the smallest particles within the PSD settle last. Zero (constant w_s) or negative slopes indicate parallel descending isolutes or descending converging isolutes in the h-t plane, respectively. With increasing initial concentration the settling velocities reduce; the slope of the w_s-c line approaches 0 or even becomes negative. The settling velocities are compared with the Richardson and Zaki (1954) HSF (Equation 3.2). For ϕ in equation 3.2, the ratio between the concentration of the suspended sediment and the bed concentration is used (c / c_{bed}). For c_{bed}, the volume concentration $\phi_{s,\min}$ is used, corresponding to a concentration of 1600 kg/m^3, based on the volume concentrations of the deposited beds in Figures 6-8 to 6-10. The decrease in w_s with c (using three arbitrary values of $w_{s,0}$ within the here measured range and $n = 4$; see Figure 6-14) corresponds with observations above $c \approx 200 - 250$ kg/m^3, indicating hindered settling effects. From the d_{50} profiles in Figures 6-8 to 6-10 segregation is observed in all granular layers, confirming that within the hindered settling regime, segregation occurs but is less than for lower initial concentrations. The observed decrease in settling velocity with increasing concentration is hence the result of hindered settling effects.

6.3.4 Density development

Conductivity measurements in columns M and O failed (explained in section 6.2.3). However, particle size analysis shows a network structure of flocs is formed capturing silt and sand particles. In such fully cohesive conditions, material functions for permeability and effective stress can be derived by applying existing consolidation theories by following Merckelbach (2000), as is elaborated on below.

Due to their cohesive character, clay particles in suspension tend to form aggregates. Krone (1963) noted that clay particles (primary particles) form flocs, which can join to form floc aggregates. These floc aggregates (or flocculi) can join to form larger aggregates, and so on (Merckelbach et al., 2002). This process can be mathematically described using fractal dimensions. When a bed is built up from fractal structures, it can be assumed that the bed also exhibits fractal properties. Figure 6-8 shows little vertical segregation in columns M and O and a homogeneous clay fraction exceeding 10%. Therefore, the mixture deposits as a composite mixture of which the sediment behaviour is considered to be homogeneous. Merckelbach (2000) studied the behaviour of consolidating mud layers. From different stages of (hindered) settling and consolidation, physically founded equations for permeability and effective stress are derived (material functions), which solve the Gibson (Gibson et al., 1967) equation. These equations are applicable when the behaviour of soft sediment is dominated by clay, but the sediment may also contain small fractions of silt and sand.

From plots of the location of the sediment-water interface versus time on double logarithmic scales (Figure 6-15), the permeability parameter (K_k) and the fractal dimension (n_f) can be determined (Merckelbach, 2000). In columns M and O, the largest initial density was higher than the gelling concentration, and hence the bed is in a consolidating state from t_0. For these curves, consolidation characteristics for the initial phase of consolidation (small effective stresses) can be determined by fitting equation 6.5:

$$h(t)-\zeta_s=\left(\frac{2-n}{1-n}\varsigma_m\right)^{\frac{1-n}{2-n}}\left((n-2)K_k\frac{\rho_s-\rho_w}{\rho_w}\right)^{\frac{1}{2-n}}t^{\frac{1}{2-n}} \qquad 6.5$$

For the experiment in columns M and O with initial concentration below the gelling concentration, hence material functions can be determined from the hindered settling phase by fitting equation 6.6, after Merckelbach (2000):

$$h(t)=\frac{\varsigma_m}{\phi_{s,0}}-\phi_{s,0}^{\,1-n}K_k\frac{\rho_s-\rho_w}{\rho_w}t \qquad 6.6$$

In these two equations ζ_m is the material height for mud, ζ_s is the material height for sand, $\phi_{s,0}$ is the solid volume fraction at t_0, h is the height of the sediment-water interface, and $n=2/(3-n_f)$, in which n_f is the fractal dimension (quantitative description for self-similarity). Since the sand contents are very low, they are not accounted for. The effective settling velocity of the mixture is determined by taking the first derivative from the initial settling curves in Figure 6-15. All experimentally derived parameters are shown in Table 6-8.

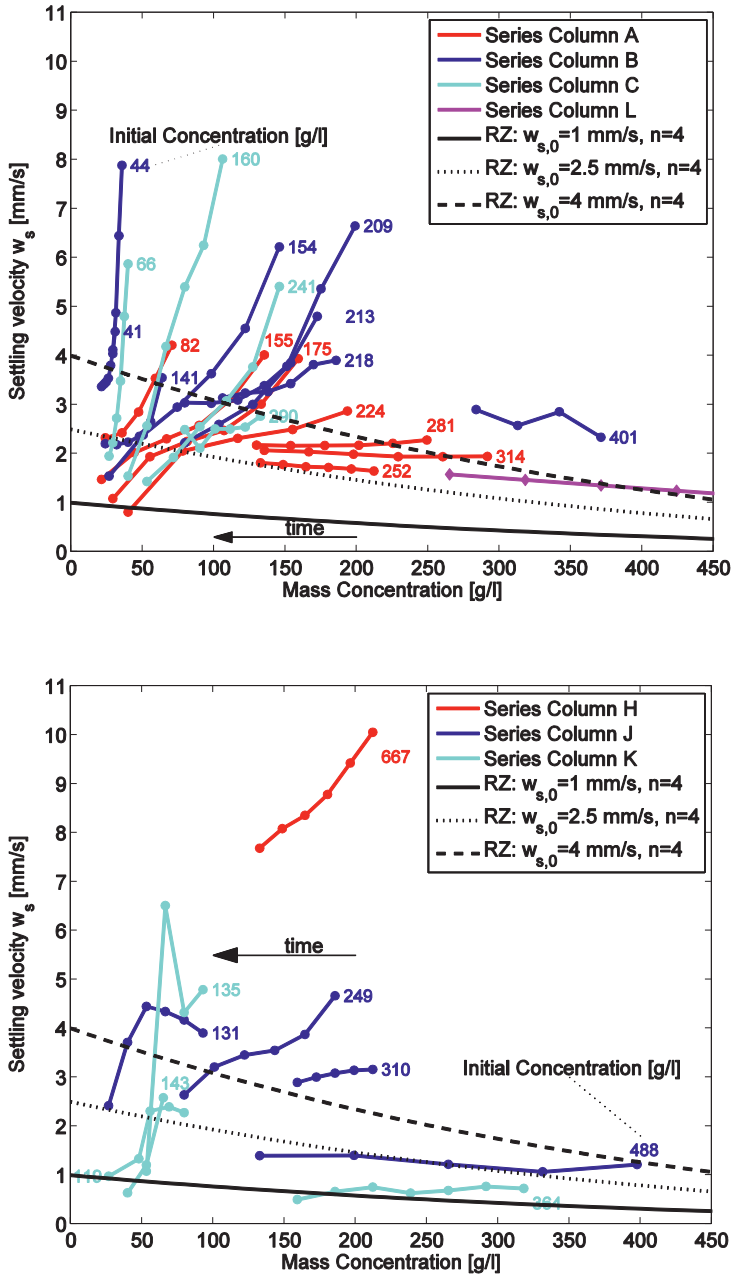

Figure 6-14 Effective settling velocities of granular material derived from measured concentration timeseries in Yangtze River columns (upper) and Yellow River Columns (lower). Numbers along lines represent the initial concentration. All settling velocities from column H increase with concentration and are mainly observed above 10 mm/s which. To improve the resolution of the lower figure, settling velocities above 10 mm/s are not shown.

The consolidation characteristics obtained from fully cohesive sediment in columns M and O allow a comparison with cohesive sediment from other sources. Consolidation experiments are described and analysed by e.g., Been (1980); Merckelbach et al. (2002). These studies focus on the consolidation behaviour of mud without sand. Merckelbach found K_k values in the range 10^{-14} to 10^{-16} m/s with fractal dimensions between 2.72 and 2.75. In suspension, the fractal dimension of mud flocs in the water column is generally around $n_f \approx 2$. The fractal dimension in a consolidating bed is generally more close to 3. Results of present fractal dimension computations (Table 6-8) show an increase in fractal dimension with increasing initial concentration, in agreement with the finding of Merckelbach et al. (2002). Here, values found for n_f are in the same order of magnitude as found by Merckelbach whereas the values for K_k are one order of magnitude larger (10^{-13} to 10^{-15} m/s). This implies that for Yangtze Estuary fresh clay deposits consolidate faster than the Ems-Dollard sediment tested by Merckelbach et al. (2002).

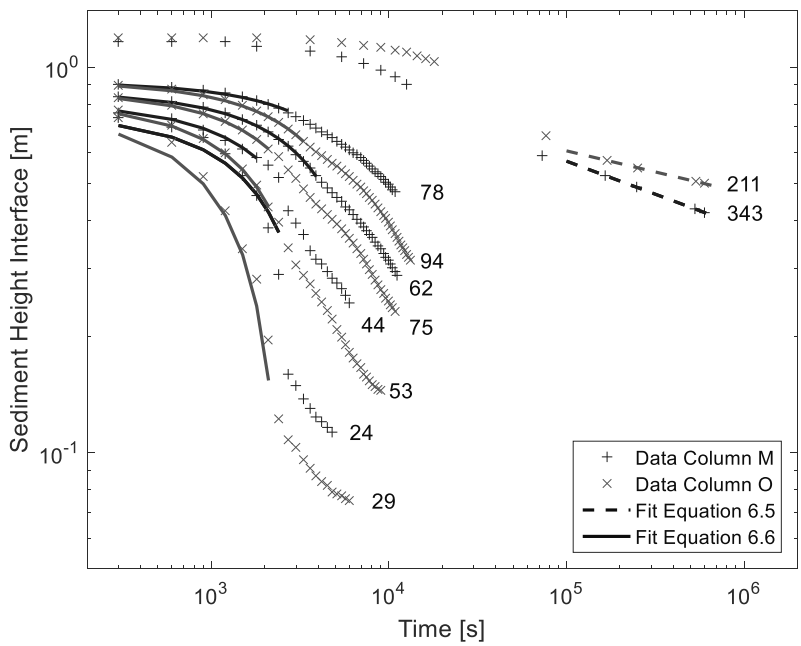

Figure 6-15 Settling and consolidation curves for columns M and O. Values indicate the initial concentration (g/l). Fitting of Equations 6.5 and 6.6 to these curves result in the values of K_k and n_f.

Column	Sand dominated $\Psi_{sa} > 70\%$		Silt dominated $\Psi_{cl} < 10\%$ $\Psi_{si} > 50\%$		Clay dominated $\Psi_{cl} > 10\%$	
	$\Delta\phi_s$	Δt (hr)	$\Delta\phi_s$	Δt (hr)	$\Delta\phi_s$	Δt (hr)
A	-	-	0.005	24	0.01	24
B	-	-	0.005	0.5	0.01	7
C	0	3.5	0.005	2.5	0.03	3.5
H	0	124	0.005	124	-	-
J	0.002	166	0.01	166	0.06	166
K	0	47	0.01	1	0.02	47

Table 6-7 Solid fraction increase in sand, silt and clay dominated layers with corresponding timeframe. Measurements for clay are done in overlying clay-water mixture.

Compaction

Also in the settling columns A, B, C, H, J and K, the density development was measured in layers with varying sediment composition. The various layers are classified according to the dominant sediment fraction. Sand-dominated implies $\psi_{sa} > 67\%$ (shaded area A in Figure 2.1) and clay-dominated implies $\psi_{cl} > 10\%$ (areas II, IV and V in Figure 2.1), following the classification by Van Ledden et al. (2004). For silt dominated sediment two conditions apply: $\psi_{cl} < 10$ % and $\psi_{si} > 50$ - 60%, indicated by area VI in Figure 2.1. Results of density developments within these layers are shown in Table 6-7.

The solid content of sand-dominated sediment remains fairly constant, whereas the solid content of the clay-dominated sediment showed continuous increase. The silt-dominated sediment showed small solid content increments, which already occur during the first 2-3 hours of the experiments, corresponding with the timeframe in which the largest excess pore-water pressures dissipation was measured. In columns H and J only small solid fraction increments ($\Delta\phi_s \approx 0.005 – 0.01$) are observed over the first 5 days.

6.3.5 Pore-water pressure dissipation

To meet the one-dimensional volume balance equation of a settling sediment-water mixture, pore fluid has to move in opposite direction as the sediment. When the permeability of a soil is sufficiently large, the excess pore-water pressure gradients are dissipated within the timescale of deposition. In columns A, C, H and J the pore-water pressures are measured. It is observed that in the granular layer, excess pore-water pressure gradients ($dp_e/dz=0$) are negligible in contrast to the overlying clay-dominated mixture. The permeability of a soil is a measure for the rate at which pore-water pressure gradients can be dissipated. The permeability of sand (order 10^{-5} to 10^{-4} m/s) is generally much larger than that of clayey soils (order 10^{-18} to 10^{-14} m/s), whereas the permeability of silts are found in-between. A lower limit for the permeability of the granular layer can be estimated from the excess pore-water pressure dissipation in the initial stage after deposition. The fluid velocity resulting from the dissipation of excess pore-water pressure can be computed from the p_e-profiles by means of a volume balance and the Darcy equation over the top layer (using Equation 4.16 in section 4.3.2). The largest fluid velocities v_f are observed at the beginning of the test between times t_0 and t_2 and

are found to be in the range of $10^{-9} < v_f < 10^{-7}$ m/s. The dissipation of excess pore-water pressure in the granular layer is limited by the lower permeability of the overlying clay-water mixture which thus forms a low permeability crust. It is noted that the material forming the crust is significantly different from the material forming the crust in the experiments with pure silt (**Chapter 4**).

From the material functions (permeability parameter K_k and the fractal dimension in the bed n_f) obtained by the fits on the settling and consolidation curves (Figure 6-15) the permeability of Yangtze Estuary clay can be determined as function of the solids contents Merckelbach (2000):

$$k_{mud} = K_k \left(\frac{\phi_s^m}{1-\phi_s^{sa}} \right)^{-\frac{2}{3-n_f}} \qquad 6.7$$

Here ϕ_s^m is the combined solid content of silt and clay particles and $1-\phi_s^{sa}$ is a correction for the sand fraction. In addition, the permeability of the deposited silt layer is determined by making use of the Kozeny-Carman equation (4.4). In order to compute the specific surface area of the granular layer in columns A, C, H and J, the average grain size distribution of the granular layer is applied. The permeability of the granular material varies only one order of magnitude between a loose and a dense packing, whereas the permeability of clayey soils can vary up to 6 – 7 orders of magnitude within the same ϕ_s range.

Table 6-8 Characteristics of experiment in columns M and O; initial concentration, effective settling velocity, gelling concentration, fractal dimension and permeability parameter.

Column + Test #	c_o [kg/m^3]	w_s [mm/s]	c_{gel} [kg/m^3]	n_f [-]	K_k [m/s]
O1	24	0.18	173	2.69	1.05×10^{-15}
O2	44	0.12	159	2.72	1.04×10^{-15}
O3	62	0.09	132	2.74	1.11×10^{-15}
O4	78	0.06	128	2.75	1.08×10^{-15}
O5	211	0.004	$c_o > c_{gel}$	2.82	1.34×10^{-13}
M1	40	0.30	107	2.71	1.05×10^{-15}
M2	56	0.18	126	2.73	1.07×10^{-15}
M3	75	0.12	144	2.75	1.11×10^{-15}
M4	104	0.09	118	2.76	1.11×10^{-15}
M5	343	0.003	$c_o > c_{gel}$	2.74	8.32×10^{-13}

6.3.6 Erosion

Pre-test bed measurements

Prior to the erosion tests, surface (sample thickness 2 mm) and subsurface (> 2 cm) sediment samples were taken from the separate cylinders for particle size analyses. Results (Table 6-9) show that the sediment is homogeneously distributed over the vertical with clay contents all exceeding 10%.

Table 6-9 Sediment fractions and median particle size of sediment used in flume (bulk sample P).

Sample	d_{50} [µm]	Sa [%]	Si [%]	Cl [%]
1 Surface	11.9	2.3	85.5	12.3
1 Subsurface	11.0	1.6	87.0	11.4
2 Surface	12.2	1.8	87.5	10.7
2 Subsurface	11.3	1.4	87.2	11.4

In addition, density profiles are measured before and after consolidation. Two density profiles are measured per cylinder (two cylinders have been prepared per test), from which an average profile is constructed (Figure 6-16). These profiles are considered to be representative for the density of the bed in the flume at the onset of each erosion experiments. Computed surface densities and vertical density gradients are shown.

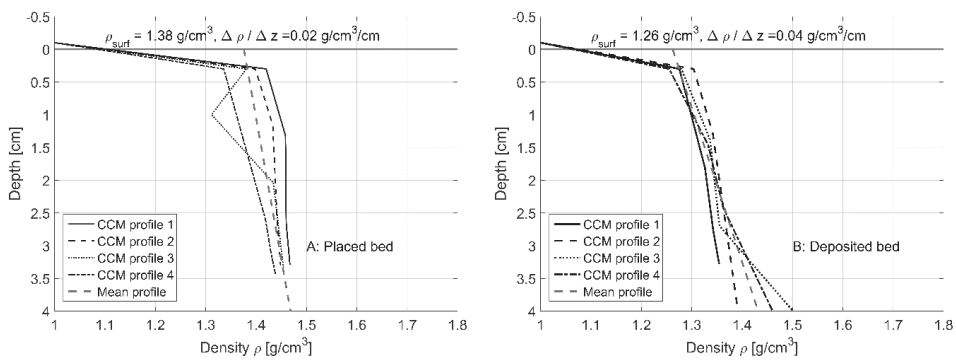

Figure 6-16 Measured (black) and mean (red) vertical density profiles in parallel prepared cylinders prior to each erosion experiment. Profiles 1 and 2 are measured in cylinder 1, profiles 3 and 4 are measured in cylinder 2.

Results

The erosion behaviour can be determined from the concentration time series. Figure 6-17 shows the measured (OSLIM and manual) concentration timeseries and imposed bed shear stresses per time interval. The manual concentration measurements are generally in good agreement with the OSLIM measurements. Generally, two types of erosion can be distinguished for cohesive sediment (Mehta and Partheniades, 1982). These are depth limited erosion and unlimited erosion, which are characteristic for stratified and homogenous beds, respectively. Concentration profiles that appear to approach a constant value are characteristic for stratified beds. In stratified beds the shear strength increases with depth, resulting in an

erosion-stop at a certain depth, where the bed shear stress approaches the shear strength of the bed. Concentration profiles that increase monotonically are characteristic for homogeneous beds and their erosion behaviour is referred to as unlimited erosion. The bed shear strength is constant over the depth, resulting in a constant erosion rate. Such concentration timeseries are characteristic for artificially placed beds which are generally not stratified.

The erosion type can be determined from the concentration timeseries during intervals with constant τ_b (Figure 6-17). During the first 5 intervals (intervals with τ_b < 0.18 Pa), very small erosion rates are measured. The concentration time series at intermediate bed shear stresses (0.41 Pa < τ_b < 0.72 Pa) tend to approach a constant value, which may be considered as depth limited erosion. For bed shear stresses exceeding τ_b = 0.72 Pa, the concentration increases nearly continuous in time. However, it seems that the duration of the intervals is too short to conclude whether an equilibrium concentration will be reached. Since the concentration time series at the intermediate bed shear stresses show a tendency to approach a constant value, it is assumed that at higher bed shear stresses an equilibrium situation will eventually be reached. Based on the above, it is concluded that depth limited erosion occurs. The density measurements (Figure 6-16) show that the beds are stratified, supporting this conclusions.

Analysis

The erosion rate E of cohesive sediment is a function of the exerted bed shear stress and has been the subject of many studies as explained in section 5.3. In present experiments, the measured concentrations (Figure 6-17) reach values of between 0 to 2 kg/m^3. For experiment #1 and #2, a concentration of 1 kg/m^3 corresponds with an eroded depth of approximately 0.10 and 0.11 mm, respectively (assuming that the whole surface area of the bed is equally eroded). With d_{50}'s of around 11 μm, approximately 10 layers of the sediment particles are thus eroded. The erosion rates are obtained by applying a linear fit to the concentration timeseries, per interval of constant bed shear stress (Figure 6-17). The linear fit thus provides the mean erosion rate per interval of constant bed shear stress. $E(\tau_b)$-plots are constructed (Figure 6-18), from which the erosion parameter M_E (first derivative) and τ_{cr} (intersection x-axis) are obtained. Typical erosion rates observed in the present study are in the range between 5x10^{-3} kg/m^2/s and 3x10^{-2} kg/m^2/s. Although the differences are small, the erosion rates are larger in test 2, which is explained from the lower surface density of the bed.

Winterwerp et al. (2012) summarized the findings of many historical erosion experiments. The critical bed shear stresses observed in the present tests are around 0.1 – 0.3 Pa which are in a lower range than values found by Winterwerp et al. (2012) (0.1 Pa < τ_{cr} < 5 Pa). The ratio between τ_{cr} and $\tau_{cr,0}$ varies between 2 to 10. The critical bed shear stress is computed using the Van Rijn (2007) equation (equation 5.13), using γ-values between 1 and 2. Depending on the γ-value, critical bed shear stresses between 0.07 Pa (γ=1) and 0.39 (γ=2) Pa are found (d_{50} obtained from Table 6-9 and solid fraction derived from Figure 6-16). From the observed critical bed shear stresses it can hence be concluded that for the used sediment, γ-values closer to 2 are applicable.

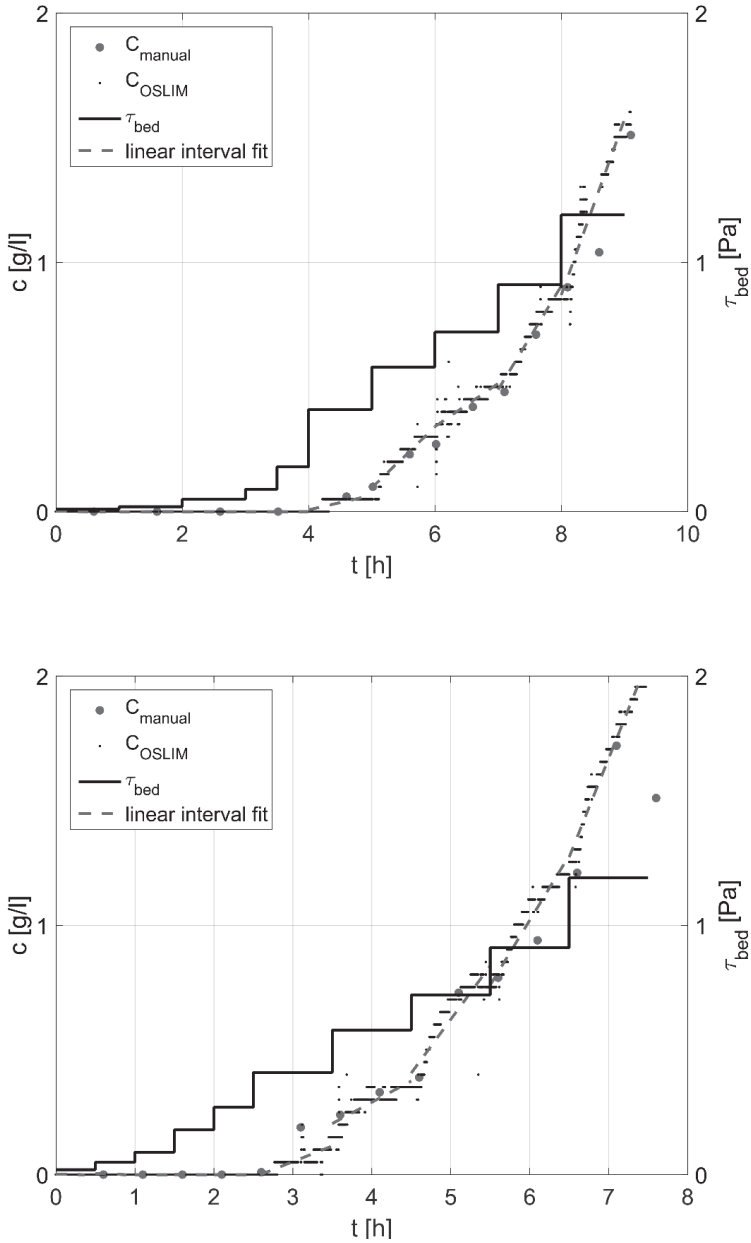

Figure 6-17 Concentration time series of experiment 1 (upper figure) and 2 (lower figure) with linear fit per interval of constant τ_{bed} indicated.

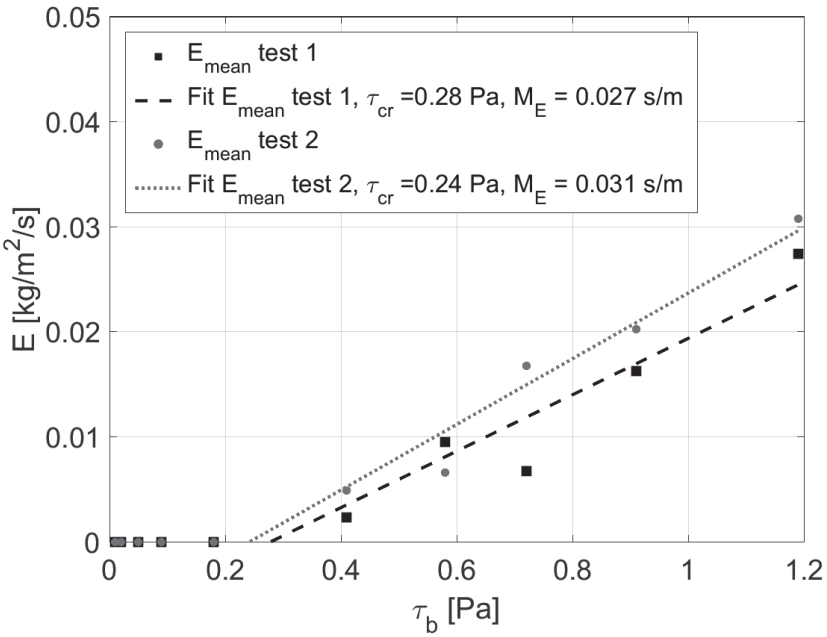

Figure 6-18 Fit on erosion rates (for E>0), with result of erosion threshold and erosion parameter.

6.4 Discussion and Conclusions

6.4.1 Discussion

Consolidation

Density development in sediment deposits is a result of consolidation and/or compaction. Consolidation is the process after deposition where pore water is driven out of flocs and out of the spaces between flocs. Strictly following this definition, silt deposits cannot consolidate since silt does not flocculate, and silt particles do not contain water. However, the permeability of fine silt is significantly lower than the permeability of sand. Therefore, pore water is expelled more slowly from fine silt deposits than from sand (see **Chapter 4**). The term compaction is then used to differentiate from the physical consolidation process in fully cohesive sediment as observed in columns M and O. Differentiating these mechanisms is difficult in non-homogeneous sediment mixtures. Nonetheless, the experimental results show various types of density development behaviour which can be attributed to a variation in sediment compositions.

According to Van Ledden et al. (2004), the transition between non-cohesive and cohesive erosion behaviour occurs at a clay content of 5 to 10%. An important observation is that for ψ_{si} > 70%, the solid fraction (both in the field and in the settling columns) is mostly smaller than 0.4. Such low solid fractions indicate that the network structure is dominated by a clay-water matrix, whereas the particle size distribution would suggest a silt-dominated skeleton to occur.

Below the 10% clay content, the solid content shows a large increase and is found to be in the range of the solid contents to be expected for silt-sand mixtures (Van Kesteren, 1996a). Hence, the high (70>%) silt percentage does not exclude cohesive behaviour. Following the above, it is concluded that cohesive consolidation can occur in sediment mixtures classified as silt dominated. Moreover, the transition between non-cohesive and cohesive consolidation is found to occur at a clay content of 10%.

Compaction

The largest dissipation rates of excess pore-water pressure in the granular sub-layer are measured during the first 2-3 hours of the sedimentation process. During these hours, computed permeabilities of the granular layer correspond to the range of the measured pore-water velocities. After the first hours, the fluid velocity decreases but excess pore-water pressures remain present in the granular layer. Further dissipation of these excess pressures at similar rates as during the first hours is prevented by the overlying consolidating clay-mixture, which thus forms a crust. From this point onward, the permeability of the overlying clay-water mixture is lower than the permeability of the granular layer. This is supported by the observed excess pore-water pressure profiles. In the clay-water mixture the excess pore-water profiles increase linear with depth, whereas in the granular layer, these are vertically constant, indicating an absence of pore-water pressure gradients (similar to the occurrence of the low permeability silt crust as found in **Chapter 4**). At the granular interface the excess pore water equals the maximum pressure in the bottom of the clay-water mixture.

It is argued that compaction occurs in natural silt-dominated sediment in the form of pore-water pressure dissipation in the first hours after deposition. After that, compaction rates rapidly slow down. The formation of a low permeability crust (whether formed from fine grains or an overlaying clay-water matrix) further delays the compaction process.

Overall, the difference between the *in-situ* and measured laboratory solid fractions in the silt-dominated sediment is approximately 5%, indicating that after the first 2-3 hours consolidation only slowly continues. During the later phases of densification of the silt-dominated sediment, either pore water is being expelled from the remaining interstitial clay flocs, or further compaction of the silt bed occurs. Hence a combination of consolidation and compaction is likely to occur. Verifying the exact physical mechanism goes beyond present experimental procedure.

Gelling concentration

Three methods are applied to obtain the gelling concentration (Table 6-10). Dankers (2006) concluded that direct measurement of c_{gel} is the most reliable and that the mass balance method overestimates c_{gel}. The fit of Equation 6.4 on the measured $w_s - c$ data shows good agreement with the measured gelling concentration of Yellow River clay. A similar fit on Yangtze River data is in less good agreement with the direct measurements, probably caused by a variation in salinity in the Yangtze River columns (A, B and C). A variation in salinity influences $w_{s,0}$ in the settling stage of the experiment through flocculation processes: it is anticipated that the floc sizes increase with salinity and the settling velocity of a single floc increases with floc size.

The gelling concentrations obtained from the laboratory experiments with the Yellow River and Yangtze River Estuary sediment are in the same order of magnitude, although gelling concentrations observed in the Yellow River are slightly lower (Table 6-10). Despite the different trajectories of the Yellow and Yangtze River, the mineralogy of the clay minerals in the two rivers is comparable (Table 6-11, based on (Li et al., 1984, Ren and Shi, 1986, Yang et al., 2004, Shiming et al., 2008, Xu et al., 2009a), although the smectite content in the Yellow River is larger. Smectite minerals have a relatively high swelling capacity. The Yellow River samples were taken in a fresh water environment, whereas the Yangtze River sediment was sampled in saline / brackish water. Therefore, it is assumed that the measured differences reflect chemical and physical variation between the Yangtze Estuary and the Yellow River water. The largest factor influencing the gelling concentration in the experiments appears to be the initial sediment concentration (Table 6-6). It is assumed that at higher initial concentrations flocs are larger, which may influence the gelling concentration.

Table 6-10 Gelling concentrations of Yangtze and Yellow River clay determined with various methods.

Method	Yangtze Estuary Clay	Yellow River Clay
Direct Measurement	107 ± 22	81 ± 17
Mass Balance	136 ± 22	-
Fit Eq. 6 (Dankers, 2006)	240, r = 0.42	133, r = 0.37

Table 6-11 Mineral composition of Yangtze and Yellow River clay.

Mineral	Yangtze River	Yellow River
Illite	66 %	64 %
Smectite	8 %	15 %
Kaolinite	12 %	9 %
Chlorite	14 %	12 %

Hindered settling

Two different settling regimes can be distinguished for the granular material. At low concentrations (c <150 – 200 kg/m^3) the settling velocities increase with particle size and sediment concentration, and the sediment segregates. For c > 150 – 200 kg/m^3, particles settle in a hindered settling regime, where w_s decreases with increasing c and segregation occurs. The value of the measured settling velocities indicates that the material is not flocculated, which is supported by the value of the gelling concentration; for concentrations exceeding c_{gel} settling velocities are still larger than 1 mm/s indicating that the material is not consolidating.

Erosion

The erosion behaviour of pure silt (**Chapter 5**) is compared with the behaviour of silt-rich sediment. It is noted that the setup of the erosion experiments differs. For the experiment with pure silt a Gust Erosion Microcosm was used, whereas the experiments with silt-rich natural

sediments have been carried out with an annular flume. The influence of erosion apparatus on the results is unknown.

Typical erosion rates of freshly deposited beds with silt sized sediment was observed in the order of $5x10^{-4}$ to $5x10^{-3}$ kg/m^2/s for bed shear stresses up to 0.3 Pa (Figure 5.9). From the experiments with silt-rich natural sediments, erosion rates are in the order of $5x10^{-3}$ to $3x10^{-2}$ kg/m^2/s (Figure 6-18) for bed shear stresses of up to 1.2 Pa. The erosion threshold of freshly deposited pure silt beds (tables 5.4 and 5.5) were found to be around 0.1 to 0.15 Pa. The erosion thresholds observed in present experiments with silt-rich natural sediment are higher (around 0.25 to 0.30 Pa). The higher value for the natural sediment is attributed to the presence of the clay fraction, which (slightly) exceeds 10%. From the observed critical bed shear stresses it is concluded that γ - values in equation 5.13 are most likely to be closer to 2 for silt-rich sediment, whereas for pure silt γ - values were found to be in the range of 1.0 to 1.6. Van Rijn (2007) compared equation 5.13 with measurements of critical shear stress of weakly consolidated mud (Thorn, 1981 and Dou, 2000) and found a best agreement for γ=1.5.

6.4.2 Conclusions

Sedimentation and erosion experiments with silt-rich sediment from the Yellow River and Yangtze Estuary have been carried out by using settling columns. The setup allows for studying the physical processes of sedimentation and for measuring material properties. Concentrations and pore-water pressure can be measured directly. Settling velocities, consolidation and compaction rates, fractal dimensions, gelling concentrations and permeability parameters can be derived by applying existing sedimentation theory from literature. This setup is flexible and sufficiently accurate to investigate sedimentation mechanisms. The most important findings from the experimental study are summarized as follows:

- Segregation in silt-rich sediment-water mixtures strongly depends on the clay percentage and the sediment concentration. In order to form a space filling clay-water mixture, the initial concentration of the clay fraction has to be close to the gelling concentration. For clay percentages above 10% and small sand percentages (<5%) the clay-water mixture is strong enough to capture interstitial material. Only 1-2% smaller clay percentages leads to segregation of silt and sand from the clay-water matrix. For ψ_{cl} > 10% the material consolidates. For ψ_{cl} < 10% and ψ_{si} > 50% sediment shows a combination of consolidation due to the presence of clay and compaction due to the low permeability of the silt fraction. For ψ_{sa} > 70 % no consolidation or compaction occurs. Therefore, it is concluded that the transition between compaction and consolidation in silt-rich sediment occurs at a threshold in the clay content of about 10%, which is in analogy with the threshold for cohesive and non-cohesive erosion behaviour.

- Silt-rich sediment settles in an analogous manner as sandy material for concentrations below 150 kg/m^3; differential settling velocities lead to segregation. Between 150 – 200 kg/m^3 the

settling regime alters into hindered settling. Now, segregation is less. The settling velocities can be modelled with the Richardson-Zaki equation using $n = 4$. Grain sizes of this material are in the range between 30 μm and 70 μm.

- The presence of a clay fraction significantly changes the erosion behaviour. The erosion threshold for a silt dominated sediment mixture with a 10% clay fraction is larger than the erosion threshold of pure silt beds. The transition between non-cohesive and cohesive erosion behaviour at a clay contents of 5 to 10%, as found by Van Ledden et al. (2004), also holds for silt-rich sediment mixtures.

Chapter 7

Synthesis and conclusions

7 Synthesis and conclusions

7.1 Introduction

Compared to sand and mud, little specific scientific attention has been given to silt because it often occurs as part of mud of which the properties are strongly influenced by the clay fraction. However, sediment mixtures consisting of nearly only silt do occur in natural systems, e.g., the Yellow River and the Yangtze River. Silt has no electrochemical bonding (such as clay) and therefore its settling, deposition, compaction and erosion behaviours differ from those of coarser sand and cohesive mud. In this thesis the properties and behaviour of silt-water mixtures have been investigated and quantified through a series of laboratory experiments. It is concluded that the timescales for settling, deposition, compaction and resuspension of silt can be large with respect to the driving forces, which significantly influences its behaviour. This chapter synthesises the hindered settling and deposition (section 7.2), compaction (section 7.3), and erosion (section 7.4) behaviour of silt-water mixtures and discuss the implications for silt-rich systems (section 7.5).

7.2 Hindered settling and deposition

A common characteristic of sediment-water mixtures is the reduction of the single-grain settling velocity with increasing concentration (hindered settling). An important difference between the settling of sand sized particles and silt sized particles is the regime in which these particles settle. Generally, the fluid movement around particles with $d < 100\ \mu m$ is laminar, causing silt particles to settle in the Stokes regime. As a result, the particle shape is of minor influence on the settling velocity. Also, the settling velocity of silt particles is very small, resulting in a long duration over which particles can stay in suspension, which may lead to the occurrence of high concentrations. Implications of high sediment concentration in rivers are addressed in section 7.5.

The hindered settling behaviour of mud (Winterwerp and Van Kesteren, 2004, Dankers and Winterwerp, 2007) and silt (present research) is found to be governed by *i*) return flow and wake formation, *ii*) increased viscosity, and *iii*) buoyancy effects. However, the increased viscosity for silt-water mixtures is found to be different from that for mud due to the difference in the number of particle collisions. For silt-water mixtures, the viscosity increases exponentially with the solid content. A hindered settling formulation (HSF) for silt-water mixtures that accounts for above mentioned processes is proposed in **Chapter 3**. Fundamental differences with the commonly used Richardson Zaki-HSF for granular mixtures are related to scaling parameters. It is found that the individual processes for silt do not all scale with the same parameter. Therefore, the proposed HSF for silt accounts for physical processes for which the solid content ϕ_s is scaled with $\phi_{s,\min}$ (solid content at the most loose packing of the bed) and $\phi_{s,\max}$ (solid content at the most dense packing of the bed). From a comparison with data obtained from laboratory experiments with fine-grained sediment, it is concluded that the derived HSF (equation 3.6) describes the hindered settling behaviour of silt-sized particles properly. In the hindered settling formulation for silt, no physical processes characteristic for cohesive sediment are included, indicating that the hindered settling of silt can be described by non-cohesive processes.

A 1D-wave equation describing the volume balance of settling particles is commonly used in sedimentation studies. The equation follows from the pioneering work by Kynch (1952). A modification of the solution to the 1D-wave equation (Equation 3.9) is found to be required to describe the hindered settling of graded sediment-water mixtures. A comparison between the solution of settling of uniform sized sediment and graded sediment is shown in Figure 7-1. Here, isolutes of uniform sized (left) and graded (right) sediment-water mixtures are drawn for the hindered settling phase (represented by the interface between clear water and the suspension) and the consolidation phase (the interface between clear water and the bed). For uniform sediments, lines of constant ϕ_s (characteristics) below the suspension interface are parallel as a result of the uniform settling velocity. In contrast, the lines of constant ϕ_s for graded sediment-water mixtures diverge from the point of origin (the water level h at t_0) up to the point of contraction. Each diverging isolute represents an effective settling velocity.

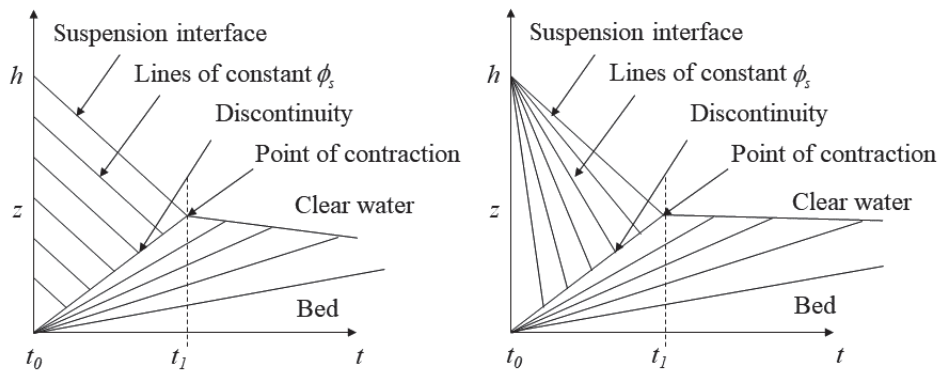

Figure 7-1 Schematic Kynch plots of settling sediment water mixture of uniform particles or flocs (left) and graded particles (right).

The diverging isolutes are characteristics for silt (and graded sediment in general) and indicates segregation during the hindered settling phase. The more the characteristics divert, the more segregation occurs. During deposition, the segregation mechanism determines how the silt bed is formed and the degree of segregation is determined by the particle size distribution (PSD) and solid content. On the other hand, hindered settling leads to a more uniform settling velocity. Experiments with fine-grained sediment mixtures (**Chapter 3**) have shown that even at very high concentrations (several hundred kg's/m^3) segregation occurs. Hence there is no critical concentration below $\phi_{s,\min}$ at which segregation of granular material is prevented.

For mud, a sufficiently high clay content results in the formation of a space filling network of mud-flocs which catches the interstitial settling particles, and thus prevents segregation. From experiments with Yangtze and Yellow River sediment it was found that segregation is prevented at clay contents of approximately 10% with corresponding mass concentration of approximately 200 to 250 kg/m^3 (see **Chapter 6**).

7.3 Compaction

The occurrence of compaction of silt beds is found to be determined by beds permeability only, and is found to be a function of the timescale of deposition. Due to segregation, the properties of a silt-bed can change significantly in time and space. These properties are *i*) the particle size distribution, *ii*) the permeability, and *iii*) the minimum and maximum solid content. Large particles settle faster than small particles, resulting in an upward decreasing permeability in the deposited bed. This leads to the formation of a low-permeable crust, which retards pore water from being expelled from the bed and hence leads to the development of pore-water overpressures. If the crust is formed within the timescale of deposition, the outflow of pore-water is retarded due to the low permeability and the silt bed is prone to compaction. On the other hand, if the bed is formed beyond the timescale of deposition, a rigid bed is formed similar to sand. Typical permeability values observed in experiments with compacting silt beds are in the range of 10^{-8} to 10^{-9} m/s. Such low permeabilities are typical for uniform spheres with a diameter of approximately 5 μm (Kozeny-Carman equation; 4.5). These permeability values are significantly smaller than the permeability of the bulk material and can result from segregation only.

The physical process of the compaction of silt beds is found to be essentially different from the consolidation of mud dominated beds. For mud, consolidation occurs when a space-filling network is formed by the cohesive sediment flocs. The flocs below a certain reference plane have to carry the weight of the sediment above this plane. The weight of sediment above that plane induces a stress within the bed, which expels pore-water from the flocs and the spaces between the flocs. During consolidation, the effective stress increases at the cost of the pore-water pressure (Winterwerp, 2011).

Consolidation of cohesive sediment mixtures can mathematically be described with the Gibson equation (equation 4.1). In **Chapter 4**, the Gibson equation is simplified by neglecting term 3 (which includes the effective stress term) for describing the initial compaction process of silt beds. This is justified because *i*) effective stresses in a silt bed are considered to be low during the initial stage of compaction, and *ii*) silt particles do not swell or compress as mud flocs do. Therefore, it is argued that term 3 of the Gibson equation is of less importance during the initial stage of compaction. Hence, the simplified Gibson equation, in which term 2 includes the permeability parameter, is considered to be suitable to describe the initial compaction process of silt. Applying term 2 only is also convenient, since fluid flow is the dominant process during (hindered) settling, which allows for a continuous mathematical description of the hindered settling phase and initial compaction. Moreover, the permeability parameter can be quantified with the Kozeny-Carman equation.

7.4 Erosion

Apparent cohesion originates from pore-water underpressures, which can develop during interactive processes between the bed and the water column. For erosion of silt beds to occur, water has to flow into the bed to dissipate these underpressures. A silt bed may increase in volume due to shear-dilatancy as a response to hydrodynamic loading conditions. Locally, pore-water underpressures can be generated during such deformation by the increase of intergranular spaces. These are dissipated by the inflow of pore water. When water can flow into the deforming soil within the timescale of shearing (direct response), the conditions are drained. If the timescale of the soil's response exceeds the timescale of the loading, underpressures (undrained conditions) will occur. These underpressures stiffen the granular skeleton and reflect an apparent bonding strength, which is referred to as apparent cohesion. For fine-grained sediment, the dissipation rate of pore-water underpressures depends on the permeability of the soil which is to a large extent determined by the solid content and particle size distribution of the bed. Therefore, the erodibility of a silt bed is highly sensitive to segregation (inverse armouring).

The primary assumption underlying the erosion of silt beds is that at zero isotropic stresses at the bed's surface, the erosion behaviour is dominated by the dissipation of pore-water underpressures. The dissipation rate of pore-water underpressures is related to the permeability parameter and follows from term 2 of the Gibson equation. Term 2 is hence assumed to govern the inflow of water in the silt bed and a simplified Gibson equation in which term 3 is neglected is therefore considered suitable to describe the erosion process. Hence, the simplified Gibson equation, in which term 2 includes the permeability parameter, is considered to be suitable to describe the initial compaction process of silt (in addition to describing the initial compaction). A surface erosion formulation for silt is derived in analogy with Winterwerp et al. (2012) by following a soil mechanical approach. Such an approach seems justified as the erosion of silt appears to be a function of bulk material properties (Roberts et al., 1998).

The newly derived erosion formulation is tested against experimental data obtained with a Gust Microcosm (erosion chamber). It is found that, for most of the experiments, computed and measured erosion rates agree reasonably well. However, an additional comparison with the experimental data obtained by Roberts et al. (1998) shows less agreement, although trends are correctly reproduced.

7.5 Implications for the Yangtze River and Yellow River

Spatial segregation and temporal variation in sediment composition is the results of sediment transport and deposition processes in most river deltas. Silt trapping in general has an influence on the sedimentation and erosion behaviour of mixed sediment. The impact of silt trapping in the catchment area of the Yangtze River on downstream morphology is discussed by Van Maren et al. (2013). The construction of the Three Gorges Dam (TGD) has accelerated the decrease in sediment load in the Yangtze River (Yang et al., 2011). He concluded that the TGD mainly traps sand and coarse silt while fine silt and clay is flushed through the reservoir. Downstream of the reservoir the transport capacity of sand is met by the erosion of the Yangtze River bed. Because of the TGD, the silt supply to the Yangtze River Estuary is expected to

decrease. Since silt is the dominant sediment type of the estuarine tidal flats, upstream trapping of silt may lead to stronger reduction in coastline acceleration (or even erosion) than based on reduction of the total sediment load (Van Maren et al., 2013).

The impact of the removal of the medium coarse silt fraction due to silt trapping in upstream reservoirs on the sediment behaviour on the tidal flats in the Yangtze Estuary can be analysed by assessing the sediment composition. Figure 6.2 shows the composition of the sediment fractions on the Northern and Southern mudflat of Chongming Island, the largest island in the Yangtze River Estuary. The composition can be classified according to the sand-silt-clay triangle as shown in Figure 2.1. The Northern mudflat sediment is likely to alter from cohesive silt dominated (classification V in Figure 2.1) to cohesive clay dominated (classification IV). Due to the high clay content in both classifications, no change in behaviour is expected. However, the sediment classification on the Southern mudflat is likely to alter from a non-cohesive silt dominated (classification VI) and non-cohesive mixed (classification III) into non-cohesive sand dominated. The presence of a low clay content indicates that the conditions are unfavourable for clay particles to settle here. Removal of the medium silt fraction will thus lead to a bed which is more prone to erosion since the bed's permeability is likely to increase.

In **Chapters 4 and 6** it was observed that crust formation as a result of segregation can occur in settling columns with artificial and natural sediment. Deposition experiments with Yangtze and Yellow River sediment have shown that sand and silt segregate from the suspended sediment mixture, leaving a low permeability clay "crust" on top of a granular layer. Here, the clay "crust" retards the dissipation of excess pore-water pressures from the lower layers. The dissipation of excess pore-water pressures from the lower layers is thus limited by the permeability of the overlying consolidating clay-water mixture. Seasonal deposition events may result in a layered bed due to segregation. Particle size distributions (unpublished data) obtained from the mini-cores taken during the Yangtze Estuary Fieldwork campaign in September 2009 show no pronounced presence of segregation. This may be attributed to a reworking of the bed (waves, biological activity). As a result, a larger overall permeability can be expected in the presence of a coarse silt fraction when clay percentages do not exceed 10%. Due to the complex interaction of waves, currents and tides, the effect on the consolidation and/or compaction behaviour on the tidal flats is difficult to assess. An in-depth understanding of the segregation mechanisms on the mudflat prior to deposition, and the reworking mechanisms on the mudflat is required to determine the effects on compaction and consolidation.

Sediment segregation during hyperconcentrated flows in the Yellow River (elaborated in section 3.6) is very complex, and very few observations exist. Nonetheless, the high concentrations typical for the Yellow River influence both fluid and sediment dynamics significantly. In the Yellow River, the concentration at which a transition from normal to hyperconcentrated flow occurs is assumed to vary from 200 kg/m^3 (Wan and Wang, 1994) to 300–400 kg/m^3 (Xu, 1999). Depending on the grain size of the suspended matter, the transition to hyperconcentrated flood may occur at even significant higher concentration (around 600 kg/m^3) for coarser sediment (Xu, 2004). From the deposition experiments with Yellow River sediment (**Chapter 6**), it was found that Yellow River sediment flocculates. Hence it is

expected that during deposition, a network structure is formed. During events of mass deposition (described in **Chapter 2**), which is often related to hyperconcentrated flood, segregation as observed in the experiments described in **Chapters 4 and 6** is therefore unlikely to occur due to the high concentrations. Hence, compaction and inverse armouring of the silt dominated bed is therefore not expected to occur. This implies that the erosion threshold is not influenced by vertical segregation and inverse armouring.

From the discussion above it is concluded that, in natural systems, the hydrodynamic conditions are responsible for the spatial and temporal variation in sediment composition and hence should be fully accounted for when studying the behaviour of sediment systems.

Overall, this work contributes to improving the understanding of the behaviour of silt-water mixtures and silt-rich sediment mixtures. It was found that time dependent process play a dominant role in the hindered settling, deposition, compaction and erosion behaviour of silt. The presence of a clay fraction in the sediment composition results in fundamental differences between the settling, compaction and erosion behaviour of pure silt and the behaviour of silt-rich sediment mixtures. New formulations for the hindered settling of fine-grained sediment-water mixtures and the surface erosion of silt beds have been developed. These formulation are verified by means of laboratory experiments and are found to perform reasonably good. The formulations can be used to study natural processes in silt-rich sediment systems and can help to understand the impacts of human interventions and/or natural changes on large scale morphological developments in river and estuaries. An important restriction to the formulations is that the sediment-mixture has to consist of find-grained sediment without any intermixture of clay.

References

ARIATHURAI, C. R. & ARULANANDAN, K. 1978. Erosion rates of cohesive soils. ASCE, *Journal of the Hydraulics Division*, 104 (2) 279-282.

ASTM-D4253 2006. Standard test methods for maximum index density and unit weight of soils using a vibratory table. *Annual Book of ASTM standards. West Conshohocken: American Society for Testing Materials*.

ASTM-D5084 2006. Standard test methods for measurements of hydraulic conductivity of saturated porous material using a flexible wall permeameter. *Annual Book of ASTM standards. West Conshohocken: American Society for Testing Materials.*

BAGNOLD, R. A. 1954. Experiments on a gravity-free dispersion of large solid spheres in a Newtonian fluid under shear. *Proceeding of the Royal Society of London.* Series A, 225, 49-63.

BALDOCK, T. E., TOMKINS, M. R., NIELSEN, P. & HUGHES, M. G. 2004. Settling velocity of sediments at high concentrations. *Coastal Engineering*, 51, 91-100.

BEEN, K. 1980. Stress-strain behaviour of a cohesive soil deposited under water. Doctoral Thesis. Oxford University.

BEEN, K. & SILLS, G. C. 1981. Self-weight consolidation of soft soils: an experimental and theoretical study. *Géotechnique*, 31, 519-535.

BERGER, C. 1968. Factors affecting settling of silt from suspension along the edge of the eastern Wadden sea (The Netherlands). *Engineering Geology*, 2, 341-349.

BOOIJ, R. 1994. Measurements of the flow field in a rotating annular flume. Delft University of Technology.

BOWDEN, R. K. 1988. Compression behaviour and shear strength characteristics of a natural silty clay sedimented in the laboratory. Ph.D. thesis, Oxford University.

BRIAUD, J., TING, F., CHEN, H., CAO, Y., HAN, S. & KWAK, K. 2001. Erosion function apparatus for scour rate predictions. *Journal of geotechnical and geoenvironmental engineering*, 127, 105-113.

BUSTOS, M. C. 1999. Sedimentation and thickening: Phenomenological foundation and mathematical theory (Vol. 8). Springer Science & Business Media.

CARMAN, P. 1938. Determination of the specific surface of powders I. Transactions. *Journal Society of Chemical Industries*, 57, 225-234.

CARMAN, P. C. 1939. Permeability of saturated sands, soils and clays. *The Journal of Agricultural Science*, 29, 262-273.

CARMAN, P. C. 1956. Flow of gases through porous media, Academic press.

CARRIER, W. D. 2003. Goodbye, Hazen; Hello, Kozeny-Carman. *Journal of Geotechnical and Geoenvironmental Engineering*, 129, 1054-1056.

CHAPUIS, R. P. & AUBERTIN, M. 2003. On the use of the Kozeny–Carman equation to predict the hydraulic conductivity of soils. *Canadian Geotechnical Journal*, 40, 616-628.

CHIEN, N. & WAN, Z. 1999. Mechanics of sediment transport. American Society of Civil Engineers.

CHUNG, S., RANDOLPH, M. & SCHNEIDER, J. 2006. Effect of Penetration Rate on Penetrometer Resistance in Clay. *Journal of Geotechnical and Geoenvironmental Engineering*, 132, 1188-1196.

COUSSOT, P. 2005. Rheometry of pastes, suspensions and granular materials. *Applications in industry and environment*. John Wiley & Sons.

CUTHBERTSON, A., DONG, P., KING, S. & DAVIES, P. 2008. Hindered settling velocity of cohesive/non-cohesive sediment mixtures. *Coastal Engineering*, 55, 1197-1208.

CUTHBERTSON, A. J. S., DONG, P. & DAVIES, P. A. 2010. Non-equilibrium flocculation characteristics of fine-grained sediments in grid-generated turbulent flow. *Coastal Engineering*, 57, 447-460.

DAI, Q., SHAN, H. X., JIA, Y. G. & MENG, X. M. 2009. Laboratory study on the relationship between suspended sediment concentration and electrical conductivity. *Proceedings of the ASME 2009 28th International Conference on Ocean, Offshore and Arctic Engineering*. Qingdao, China: College of Environmental Science and Engineering

DANKERS, P. J. T. 2006. On the hindered settling of suspensions and mud-sand mixtures. Ph.D. thesis, Delft University of Technology.

DANKERS, P. J. T. & WINTERWERP, J. C. 2007. Hindered settling of mud flocs: Theory and validation. *Continental Shelf Research*, 27, 1893-1907.

DE LUCAS, M. A., BAKKER, M., WINTERWERP, J. C., VAN KESSEL, T. & COZZOLI, F. 2013. Erodibility of soft fresh water sediments in Markermeer: the role of bioturbation by meiobenthic deposit feeders. *Ocean Dynamics,* 63(9-10), 1137-1150.

DIPLAS, P. & PAPANICOLAOU, A. N. 1997. Batch analysis of slurries in zone settling regime. *Journal of environmental engineering*, 123, 659-667.

DOU, G. 1960. On the incipient motion of sediment. *Chinese Journal of Hydraulic Engineering*, 44-60.

DOU, G., DOU, X. & LI, T. 2001. Incipient motion of sediment by waves. *Science in China Series E: Technological Sciences*, 44, 309-318.

EINSTEIN, A. 1906. Eine neue Bestimmung der Moleküldimensionen. *Annalen der Physik*, 324, 289-306.

EISMA, D., BALE, A., DEARNALEY, M., FENNESSY, M., VAN LEUSSEN, W., MALDINEY, M.-A., PFEIFFER, A. & WELLS, J. 1996. Intercomparison of in situ suspended matter (floc) size measurements. *Journal of Sea Research*, 36, 3-14.

FAIR, G. M. & HATCH, L. P. 1933. Fundamental factors governing the streamline flow of water through sand. *American Water Works Association*, 25, 1551-1565.

FLOSS, R. 1970. Vergleich der Verdichtungs- und Verformungseigenschaften unstetiger und stetiger Kiessanden hinsichtlich ihrer Eignung als ungebundenes Schuttmaterial in Strassenbau. *Wissenschaftliche Berichtte der Bundesanstalt fur Strassenwesen*, Heft 9.

FULLER, W. B. & THOMPSON, S. E. 1907. The laws of proportioning concrete. *Asian Journal of Civil Engineering Transport*, 59, 67 To 143.

GIBSON, R. E., ENGLAND, G. L. & HUSSEY, M. J. L. 1967. The Theory of One-Dimensional Consolidation of Saturated Clays. *Géotechnique*, 17, 261-273.

HIEMENZ, P. C. & RAJAGOPALAN, R. 1997. Principles of Colloid and Surface Chemistry, revised and expanded, *CRC press*.

HJULSTROM, F. 1935. Studies of the morphological activity of rivers as illustrated by the river Fyris. *Bulletin of the Geological Institution of Upsala*, 25.

JACOBS, W. 2011. Sand-mud erosion from a soil mechanical perspective. Ph.D. thesis, Delft University of Technology.

JEPSEN, R., ROBERTS, J. & LICK, W. 1997. Effects of bulk density on sediment erosion rates. *Water, Air and Soil Pollution*, 99, 21-31.

JIN, L., MCNEIL, J., LICK, W. & GAILANI, J. 2002. Effects of bentonite on the erosion rates of quartz particles. Santa Barbara: *University of California: Mechanics & Environmental Engineers.*

KOZENY, J. 1927. Uber die kapillare Leitung des Wassers im Boden (Aufstieg Versickerung und Anwendung auf die Bewasserung. Sitz. Ber. Akad. Wiss, Wien, Math. Nat.(Abt. Iia), 136a.

KRIEGER, I. M. & DOUGHERTY, T. J. 1959. A mechanism for non-Newtonian flow in suspensions of rigid spheres. *Transactions of the Society of Rheology*, 3, 137-152.

KRONE, R. B. 1962. Flume studies of the transport of sediment in estuarial shoaling processes. University of California, Berkeley, USA.

KRUMBEIN, W. C. & SLOSS, L. L. 1963. Stratigraphy and sedimentation, Freeman. No. QE571 K7 1963.

KUERBIS, R., NEGUSSEY, D. & VAID, Y. P. 1988. Effect of Gradation and Fines Content on the Undrained Response of Sand. *Hydraulic Fill Structures* (GPS21), 330-345.

KYNCH, G. J. 1952. A theory of sedimentation. *Transactions of the Faraday Society*, 48, 166-176.

LAMBE, T. W. & WHITMAN, R. V. 1979. Soil Mechanics, New York, John Wiley and Sons.

LI, Y. H., TERAOKA, H., YANG, T. S. & CHEN, J. S. 1984. The elemental composition of suspended particles from the Yellow and Yangtze Rivers. *Geochimica et Cosmochimica Acta*, 48(7), 1561-1564.

LICK, W., JIN, L. & GAILANI, J. 2004. Initiation of Movement of Quartz Particles. *Journal of Hydraulic Engineering*, 130, 755-761.

MAGGI, F. 2005. Flocculation dynamics of cohesive sediment. Doctoral Thesis, Delft University of Technology.

MANNING, A. J., BAUGH, J. V., SPEARMAN, J. R., PIDDUCK, E. L. & WHITEHOUSE, R. J. S. 2011. The settling dynamics of flocculating mud-sand mixtures: Part 1: Empirical algorithm development. *Ocean Dynamics*, 61, 311-350.

MANNING, A. J., BAUGH, J. V., SPEARMAN, J. R. & WHITEHOUSE, R. J. S. 2010. Flocculation settling characteristics of mud: sand mixtures. *Ocean Dynamics*, 60, 237-253.

MASTBERGEN, D. R. & VAN DEN BERG, J. H. 2003. Breaching in fine sands and the generation of sustained turbidity currents in submarine canyons. *Sedimentology*, 50, 625-637.

MEHTA, A. J. & PARTHENIADES, E. 1982. Resuspension of deposited cohesive sediment beds. *18th Conference on Coastal Engineering*, Cape Town, South Africa. 1569-1588.

MERCKELBACH, L. & KRANENBURG, C. 2004. Determining effective stress and permeability equations for soft mud from simple laboratory experiments. *Géotechnique*, 54, 581-591.

MERCKELBACH, L. M. 2000. Consolidation and strength evolution of soft mud layers. Doctoral Thesis, Delft University of Technology.

MERCKELBACH, L. M., KRANENBURG, C. & WINTERWERP, J. C. 2002. Strength modelling of consolidating mud beds. *Proceedings in Marine Science*. Elsevier.

MIEDEMA, S. 2011. Constructing the Shields Curve, a new theoretical approach and its applications. WODCON XIX. Beijing China.

MITCHENER, H. & TORFS, H. 1996. Erosion of mud/sand mixtures. *Coastal Engineering*, 29, 1-25.

MONTSERRAT, F., VAN COLEN, C., PROVOOST, P., MILLA, M., PONTI, M., VAN DEN MEERSCHE, K., YSEBAERT, T. & HERMAN, P. M. J. 2009. Sediment segregation by biodiffusing bivalves. *Estuarine, Coastal and Shelf Science*, 83, 379-391.

NEN-5124 1993. Geotechnics: Laboratory determination of permeability of soil by the falling head method (in Dutch). Nederlands Normalisatie Instituut.

NEZU, I. & NAKAGAWA, H. 1993. Turbulence in open channel flows, Rotterdam. *IAHR-monograph*.

PARTHENIADES, E. 1962. A study of erosion and deposition of cohesive soils in salt water. Doctoral Thesis, University of California

QIAN, N. N. C. 1980. Preliminary study on the mechanism of hyperconcenetrated flow in north-west region of China (in Chinese). *Selected papers of the symposium on sediment problems on the Yellow River*, 4, 244-267.

QUEMADA, D. 1985. Phenomenological rheology of concentrated dispersions. I: Clustering effects and the structure-dependent packing fraction. *Journal de Mécanique Théorique et Appliquée* 267-288.

RANDOLPH, M. F. & HOUSE, A. R. 2001. The complementary roles of physical and computational modelling. *IJPMG - International Journal of Physical Modelling in Geotechnics*, 1, 01-08.

REN, M. E. & SHI, Y. L. 1986. Sediment discharge of the Yellow River (China) and its effect on the sedimentation of the Bohai and the Yellow Sea. *Continental Shelf Research*, 6, 785-810.

RICHARDSON, J. F. & ZAKI, W. N. 1954. The sedimentation of a suspension of uniform spheres under conditions of viscous flow. *Chemical Engineering Science*, 3, 65-73.

ROBERTS, J., JEPSEN, R. & GOTTHARD, D. 1998. Effects of particle size and bulk density on erosion of quartz particles. *Journal of Hydraulic Engineering*, 124, 1261.

SCHOFIELD, A. & WROTH, P. 1968. Critical state soil mechanics, McGraw-Hill London. Vol. 310.

SCOTT, K. J., SCIENTIFIC, C. F., GROUP, I. R. C. E. R., SCIENTIFIC, S. A. C. F. & GROUP, I. R. C. E. R. 1984. Hindered Settling of a Suspension of Spheres: Critical Evaluation of Equations Relating Settling Rate to Mean Particle Diameter and Suspension Concentration, Chemical Engineering Research Group, CSIR.

SHIELDS, A. 1936. Anwendung der Ahnlichkeits Mechanik und der Turbulenzforschung auf die Geschiebe Bewegung: Preuss. *Versuchanstalt fur Wasserbau und Schiffbau.*

SHIMING, W., ANCHUN, L., KEHUI, X. & XUEMING, Y. 2008. Characteristics of Clay Minerals in the Northern South China Sea and Its Implications for Evolution of East Asian Monsoon since Miocene. *Journal of China University of Geosciences*, 19, 23-37.

SLEATH, J. F. A. 1999. Conditions for plug formation in oscillatory flow. *Continental Shelf Research*, 19, 1643-1664.

SORENSEN, J. A. & GLASS, G. E. 1987. Ion and temperature dependence of electrical conductance for natural waters. *Analytical Chemistry*, 59, 1594-1597.

STOKES, G. G. 1851. On the effect of the internal friction of fluids on the motion of pendulums. *Transition of Cambridge Philosophy Society*, 9, 8-106.

TE SLAA, S. 2012. Calibration Report Annular Flume Zhejiang University. Delft University of Technology.

TERNAT, F., BOYER, P., ANSELMET, F. & AMIELH, M. 2008. Erosion threshold of saturated natural cohesive sediments: Modeling and experiments. *Water Resources Research*, 44.

TERZAGHI, K. 1943. Theoretical soil mechanics. JohnWiley & Sons. New York, 11-15.

TERZAGHI, K. & FRÖHLICH, O. K. 1936. Theorie der Setzung von Tonschichten; eine Einführung in die analytische Tonmechanik, Leipzig, Wien: Franz Deuticke.

TERZAGHI, K. & PECK, R. B. 1967. Soil mechanics in engineering practice. John Wiley & Sons.

THOMSEN, L. & GUST, G. 2000. Sediment erosion thresholds and characteristics of resuspended aggregates on the western European continental margin. *Deep Sea Research Part I: Oceanographic Research Papers*, 47, 1881-1897.

TOMKINS, M. R., BALDOCK, T. E. & NIELSEN, P. 2005. Hindered settling of sand grains. *Sedimentology*, 52, 1425-1432.

TOORMAN, E. A. 1999. Sedimentation and self-weight consolidation: constitutive equations and numerical modelling. *Géotechnique*, 49, 709-726.

TORFS, H., MITCHENER, H., HUYSENTRUYT, H. & TOORMAN, E. 1996. Settling and consolidation of mud/sand mixtures. *Coastal Engineering*, 29, 27-45.

TURNER, J. S. 1979. Buoyancy effects in fluids. *Cambridge University Press*.

UITTENBOGAARD, R. E. 1994. Physics of Turbulence: Technical report on subtask 5.2. In: *Hydraulics Department Report Z649*, MAST VERIPARSE Project. Delft.

VAN KESTEREN, W. G. M. 1996. Slope stability analysis Orange River mouth, *WL|Delft Hydraulics, report Z2462*.

VAN LEDDEN, M., VAN KESTEREN, W. G. M. & WINTERWERP, J. C. 2004. A conceptual framework for the erosion behaviour of sand-mud mixtures. *Continental Shelf Research*, 24, 1-11.

VAN MAREN, D. 2007. Grain size and sediment concentration effects on channel patterns of silt-laden rivers. *Sedimentary Geology*, 202, 297-316.

VAN MAREN, D. S., WINTERWERP, J. C., WU, B. S. & ZHOU, J. J. 2009a. Modelling hyperconcentrated flow in the Yellow River. *Earth Surface Processes and Landforms*, 34, 596-612.

VAN MAREN, D. S., WINTERWERP, J. C., WANG, Z. Y. & PU, Q. 2009b. Suspended sediment dynamics and morphodynamics in the Yellow River, China. *Sedimentology*, 56, 785-806.

VAN MAREN, D. S., YANG, S.-L. & HE, Q. 2013. The impact of silt trapping in large reservoirs on downstream morphology: the Yangtze River. *Ocean Dynamics*, 63, 691-707.

VAN RHEE, C. 2010. Sediment Entrainment at High Flow Velocity. *Journal of Hydraulic Engineering*, 136, 572-582.

VAN RIJN, L. C. 1984. Sediment Transport, Part I: Bed Load Transport. *Journal of Hydraulic Engineering*, 110, 1431-1456.

VAN RIJN, L. C. 1989. Handbook sediment transport by currents and waves, Delft Hydraulics Laboratory.

VAN RIJN, L. C. 1993. Principles of sediment transport in rivers, estuaries and coastal seas, *Aqua publications Amsterdam*.

VAN RIJN, L. C. 2007. Unified View of Sediment Transport by Currents and Waves. I: Initiation of Motion, Bed Roughness, and Bed-Load Transport. *Journal of Hydraulic Engineering*, 133, 649-667.

WAN, Z. & WANG, Z. 1994. Hyperconcentrated Flow. *IAHR monograph*, Balkema: Rotterdam, 230.

WINTERWERP, J. C. 2011. The physical analyses of muddy sedimentation processes.

WINTERWERP, J. C. 2001. Stratification of mud suspensions by buoyancy and flocculation effect. *Journal of Geophysical Research*, 106 22.

WINTERWERP, J. C. 2002. On the flocculation and settling velocity of estuarine mud. *Continental Shelf Research*, 22, 1339-1360.

WINTERWERP, J. C. 2006. Stratification effects by fine suspended sediment at low, medium, and very high concentrations. *Journal of Geophysical Research*: Oceans 111.

WINTERWERP, J. C. & VAN KESTEREN, W. G. M. 2004. Introduction to the physics of cohesive sediment in the marine environment, Elsevier

WINTERWERP, J. C., VAN KESTEREN, W. G. M., VAN PROOIJEN, B. & JACOBS, W. 2012. A conceptual framework for shear-flow induced erosion of soft cohesive sediment beds. *Journal of Geophysical Research - Ocean*s, 117(C10).

WU, B., WANG, G., MA, J. & ZHANG, R. 2005. Case Study: River Training and Its Effects on Fluvial Processes in the Lower Yellow River, China. *Journal of Hydraulic Engineering*, 131, 85-96.

WU, W. & WANG, S. S. 2006. Formulas for sediment porosity and settling velocity. *Journal of Hydraulic Engineering*, 132, 858-862.

XIA, Z. & WANG, G. 1982. The settling of non-cohesive particles in a flocculated suspension (in Chinese). *Journal of Sediment Research*, 1, 14-23.

XU, J. 1999. Erosion caused by hyperconcentrated flow on the Loess Plateau of China. *Catena*, 36, 1-19.

XU, J. 2004. Double-thresholds in scour–fill processes and some implications in channel adjustment. *Geomorphology*, 57, 321-330.

XU, K., MILLIMAN, J. D., LI, A., PAUL LIU, J., KAO, S.-J. & WAN, S. 2009. Yangtze- and Taiwan-derived sediments on the inner shelf of East China Sea. *Continental Shelf Research*, 29, 2240-2256.

YANG, S., MILLIMAN, J., LI, P. & XU, K. 2011. 50,000 dams later: erosion of the Yangtze River and its delta. *Global and Planetary Change*, 75, 14-20.

YANG, S. Y., JUNG, H. S. & LI, C. X. 2004. Two unique weathering regimes in the Changjiang and Huanghe drainage basins: geochemical evidence from river sediments. *Sedimentary Geology*, 164, 19-34.

ZANKE, U. 2003. On the influence of turbulence on the initiation of sediment motion. *International Journal of Sediment Research*, 18, 17-31.

ZANKE, U. C. E. 1997. Berechnung der Sinkgeschwindigkeiten von Sedimenten. *Mitt. des Franzius-Instituts für Wasserbau*. Technical University, Hannover, Germany.

ZHANG, W., XING, Y., YU, L., FENG, H. & LU, M. 2008. Distinguishing sediments from the Yangtze and Yellow Rivers, China: a mineral magnetic approach. *The Holocene*, 18, 1139-1145.